Sea Ice Climate Change Initiative: Phase 2

D4.2 Climate Assessment Report (CAR)

Doc Ref: SICCI-CAR

Version: 1.0

Date: 23 July 2018

Consortium Members

Change Record

Issue	Date	Reason for Change	Author
CAR 0.9	26 September 2017	First draft of SICCI2 CAR	Stefan Kern, Armin Köhl, Thomas Lavergne, Dirk Notz, Detlef Stammer
1.0, v01	10 January 2018	Organizing of SICCI2 CAR final version	Stefan Kern
	30 January 2018	Included results from work done at ICDC with regard to sea-ice area, extent, sea-ice volume and sea-ice volume flux.	Stefan Kern, Louisa Bell, Detlef Stammer, Armin Köhl.
1.0, v02	May 14 2018	Included results of MPI-Met work	Laura Niederdrenk, Dirk Notz
1.0, v03	June 26 2018	Included results of work done at IfM	Xueyuan Liu, Armin Köhl, Detlef Stammer
1.0, v03	July 09 2018	Final version, literature list properly included	Stefan Kern
1.0	July 23 2018	Issued for Milestone #6 (KO+42)	Stefan Kern

Authorship

Role	Name	Signature
Written by:	Stefan Kern, Xueyuan Liu, Armin Köhl, Laura Niederdrenk, Dirk Notz, Detlef Stammer	
Checked by:	Gary Timms	
Approved by:	Stein Sandven	
Authorised by:	Pascal Lecomte	

Distribution

Organisation	Names	Contact Details
ESA	Pascal Lecomte, Anna Maria	Pascal.Lecomte@esa.int; Anna.Maria.Trofaier@esa.int
NERSC	Stein Sandven, Kirill Khvorostovsky	Stein.Sandven@nersc.no; kirill.khvorostovsky@nersc.no
CGI	Gary Timms, Sabrina Mbajon, Clive Farquhar	gary.timms@cgi.com; sabrina.mbajon.njiche@cgi.com; clive.farquhar@cgi.com
MET Norway	Thomas Lavergne, Atle Sørensen	t.lavergne@met.no; atlems@met.no
DMI	Rasmus Tonboe	rtt@dmi.dk
DTU	Roberto Saldo, Henriette Skourup, Leif Toudal Pedersen	rs@space.dtu.dk; hsk@space.dtu.dk; ltp@space.dtu.dk
FMI	Marko Mäkynen, Eero Rinne	marko.makynen@fmi.fi; eero.rinne@fmi.fi;
University of Hamburg	Stefan Kern, Lars Kaleschke, Xiangshan Tian-Kunze	stefan.kern@zmaw.de; lars.kaleschke@uni-hamburg.de; xiangshan.tian-kunze@uni-hamburg.de
University of Bremen	Georg Heygster	heygster@uni-bremen.de
MPI-M	Dirk Notz, Louisa Bell	dirk.notz@mpimet.mpg.de; louisa.bell@mpimet.mpg.de
Ifremer	Fanny Ardhuin	Fanny.Ardhuin@ifremer.fr
AWI	Marcel Nicolaus, Stefan Hendricks, Thomas Hollands	marcel.nicolaus@awi.de; stefan.hendricks@awi.de; thomas.hollands@awi.de

Table of Contents

List of Figures

List of Tables

1 Introduction

1.1 Purpose and Scope

This document describes the results of the usage and application of the SICCI-2 project sea ice concentration (SIC) and sea ice thickness (SIT) data sets in climate research – namely for inter-comparison to model data and for usage in assimilation experiments. It also describes results from using the SICCI-2 SIC and SIT data sets for estimation of the sea ice area and extent as well as sea-ice volume and sea-ice volume fluxes.

1.2 Document Structure

After this introduction and the list of references, the document is divided into three sections. The first section describes and presents value added products derived from the SICCI-2 project products. This covers the contractual work associated with WP4210 and WP4220. The second section informs about results obtained so far by using SICCI-2 project products for dynamically consistent assimilation into a coupled ocean – sea ice model as carried out at the Institute of Oceanography, University of Hamburg. This covers the contractual work associated with WP4300. The third section presents the status of and the results of the assimilation experiments in Earth system models – namely the MPI-ESM of the Max-Planck Institute of Meteorology, Hamburg – and of the development of a satellite simulator for MPI-ESM. This covers the contractual work associated with WP4400 and WP4500.

1.3 Document Status

This is issue 1.0 of the CAR from the SICCI-2 project released to ESA as part of the project's contractual deliverable set.

Note that neither the list in section 1.4 nor the reference list in section 1.5 has been updated relative to the CAR of phase 1. Relevant references currently are placed at the end of the section describing the status of WP4300; these will be included onto the references list for the final version of CAR.

1.4 Applicable Documents

The following table lists the Applicable Documents that have a direct impact on the contents of this document.

Acronym	Title	Reference	Issue
AD-1	Sea Ice ECV Project Management Plan	ESA-CCI_SICCI_PMP_D6.1_v1.1	1.3

Table 1-1: Applicable Documents

1.5 Reference Documents

Acronym	Title	Reference	Issue
RD-01	D3.4 Product User Guide (PUG)	Sørensen, A., and T. Lavergne, SICCI-PUG-P2-17-09	V1.1, Sep. 2017
RD-02	Algorithm Theoretical Basis Document (ATBDv1)	Pedersen, L. T., et al.	v2.2, Sep. 2017
RD-03	D3.7 Detailed Processing Model (DPMv2)	Lavergne, T., and E. Rinne, SICCI-DPMv2	v1.0, May 2014
RD-04	D4.1 Product Validation and Inter-comparison Report PVIR	Kern, S., A. Beitsch, N. Ivanova, M. Zygmunstowska, K. Khovorostovsky, G. Spreen, SICCI-PVIR	v1.1, Jul 2018
RD-05	Data Access Requirement Document (DARD)	Kern, S., SICCI-P2-DARD-08-15	v2.0, Sep. 2015
RD-06	Product User Manual for Global Sea Ice Concentration Climate Data Record OSI-450	Sørensen, A., T. Lavergne, S. Eastwood, Document version 1.0, data set version 2.0, DOI: 10.15770/EUM_SAF_OSI_0008	v1.0, Mar 2017
RD-07	Snow depth on Arctic sea ice	Warren, S. G., I. G. Rigor, N. Untersteiner, V. F. Radionov, N. N. Bryazgin, Y. I. Aleksandrov, and R. Colony, Journal of Climate, 12, 1814-1829, 1999.	n.a.
RD-08	Unprecedented springtime retreat of Antarctic sea ice in 2016	Turner, J., T. Philips, G. J. Marshall, J. S. Hosking, J. O. Pope, T. J. Bracegirdle, and P. Deb, Geophysical Research Letters, 44(13), 6868-6875, https://doi.org/10.1002/2017GL073656.	n.a.
RD-09	Satellite observations of Antarctic sea ice thickness and volume	Kurtz, N. T., and T. Markus, Journal of Geophysical Research, 117, C08025, doi:10.1029/2012JC008141, 2012.	n.a.

Acronym	Title	Reference	Issue
RD-10	Snow depth of the Weddell and Bellingshausen sea ice covers from IceBridge surveys in 2010 and 2011: An examination,	Kwok, R., and T. Maksym, Journal of Geophysical Research - Oceans, 119, 4141–4167, doi:10.1002/2014JC009943, 2014.	n.a.
RD-11	Antarctic Sea-Ice Thickness Retrieval from ICESat: Inter-Comparison of Different Approaches	Kern, S., B. Ozsoy-Cicek, and A. P. Worby, Remote Sensing, 8(7), 538; doi:10.3390/rs8070538, 2016.	n.a.
RD-12	Consistent CryoSat-2 and Envisat Freeboard Retrieval of Arctic and Antarctic Sea Ice	Paul, S., S. Hendricks, R. Ricker, S. Kern, and E. Rinne, The Cryosphere, revision under review, https://doi.org/10.5194/tc-2018-34, 2018.	n.a.
RD-13	*Polar Pathfinder Daily 25 km EASE-Grid Sea Ice Motion Vectors, Version 3*.	Fowler, C., J. Maslanik, W. Emery, and M. Tschudi. [Indicate subset used]. Boulder, Colorado USA. NASA National Snow and Ice Data Center Distributed Active Archive Center. doi: https://doi.org/10.5067/O57VAIT2AYYY, 2016.	V3.0
RD-14	Fram Strait sea ice volume export estimated between 2003 and 2008 from satellite data	Spreen, G., S. Kern, D. Stammer and E. Hansen, Geophysical Research Letters, 36, L19502, doi:10.1029/2009GL039591, 2009.	n.a.
RD-15	On the low frequency phase relation between the Denmark Strait and the Faroe-Bank Channel overflows	Serra, N., R. H. Käse, A. Köhl, D. Stammer, and D. Quadfasel, Tellus A, 62 (4), 530–550, doi:10.1111/j.1600-0870.2010.00445.x, 2010.	n.a.
RD-16	Dynamic thermodynamic sea ice model	Hibler, W. D., Journal of Physical Oceanography, 9(4), 1979.	n.a.
RD-17	Modeling a variable thickness sea ice cover	Hibler, W. D., Monthly Weather Review, 108 (12), 1943–1973, 1980.	n.a.

Acronym	Title	Reference	Issue
RD-18	A model for the thermodynamic growth of sea ice in numerical investigations of climate	Semtner, A. J., J. Phys. Oceanogr., 6 (3), 379–389, 1976.	n.a.
RD-19	Arctic ice-ocean modelling with and without climate restoring	Zhang, J., W. D. Hibler, M. Steele, and D. A. Rothrock, Journal of Physical Oceanography, 28 (2), 191–217, 1998.	n.a.
RD-20	On modelling the seasonal thermodynamic cycle of sea ice in studies of climatic change	Semtner, A. J., Climatic Change, 6(1), 27–37, doi:10.1007/BF00141666, 1984.	n.a.
RD-21	Global coupled sea ice-ocean state estimation	Fenty, I., D. Menemenlis, and H. Zhang, Climate Dynamics, 49(3), 931-956, doi:10.1007/s00382-015-2796-6, 2015.	n.a.
RD-22	PHC: A global ocean hydrography with a high-quality Arctic Ocean	Steele, M., R. Morley, and W. Ermold, Journal of Climate, 14(9), 2079-2087, 2001.	n.a.
RD-23	A new reprocessed 20 years altimetric data set for the Arctic Ocean	Cheng, Y., O. Andersen, and P. Knudsen, Marine Geodesy, accepted in 2014.	n.a.
RD-24	Accuracy of satellite sea surface temperatures at 7 and 11 GHz	Gentemann, C. L., T. Meissner, and F. J. Wentz, IEEE Transactions on Geoscience and Remote Sensing, 48, 1009-1018, 2010.	n.a.
RD-25	AVISO Delay-Time (DT) MSLA and DT-MADT	Ssalto/Duacs, http://www.aviso.altimetry.fr/duacs/	Pre v15.0
RD-26	Quality control of ocean temperature and salinity profiles Historical and real-time data	Ingleby, B., and M. Huddleston, Journal of Marine Systems, 65(1-4), 158–175,doi:10.1016/j.jmarsys.2005.11.019, 2007.	n.a.

Acronym	Title	Reference	Issue
RD-27	The North Atlantic and Nordic Seas hydrography collection	Nilsen, J. E. O., NERSC Technical Report #372, NERSC, Bjerknes Center for Climate Research, Bergen, Norway, 20 pp., 2008.	n.a.
RD-28	Skill metrics for evaluation and comparison of sea ice models	Dukhovskoy, D. S., J. Ubnoske, E. Blanchard-Wrigglesworth, H. R. Hiester, and A. Proshutinsky, J. Geophys. Res. Oceans, 120, 5910–5931, doi:10.1002/2015JC010989, 2015.	n.a.
RD-29	Arctic sea ice variability and trends, 1979–2010	Cavalieri, D. J. and Parkinson, C. L., The Cryosphere, 6, 881-889, doi:10.5194/tc-6-881-2012, 2012.	n.a.
RD-30	Large decadal decline of the Arctic multiyear ice cover	Comiso, J. C., J. Climate, 25, 1176–1193, 2012.	n.a.
RD-31	Decline in Arctic sea ice thickness from submarine and ICESat records: 1958–2008	Kwok, R. and Rothrock, D. A., Geophys. Res. Lett., 36, L15501, https://doi.org/10.1029/2009GL039035, 2009.	n.a.
RD-32	Observed Arctic sea-ice loss directly follows anthropogenic CO2 emission	Notz, D., and Stroeve, J., Science, doi:10.1126/science.aag2345, 2016.	n.a.
RD-33	Remote Sensing of Sea Ice in the Northern Sea Route-Studies and Applications	Johannessen, O. M., Alexandrov, V., Sandven, S., Pettersson, L. H., Bobylev, L. and Kloster, K., , Springer Praxis Books, Nansen Centers Polar Series no.4., 2007.	n.a.
RD-34	Polar Amplification of Climate Change in the Coupled Model Intercomparison Project	Holland, M.M. and Bitz, C.M., Climate Dynamics, 21, 221-232, http://dx.doi.org/10.1007/s00382-003-0332-6, 2003.	n.a.

Acronym	Title	Reference	Issue
RD-35	Ocean Data Assimilation in Support of Climate Applications: Status and Perspectives	Stammer, D., Balmaseda, M., Heimbach, P., Köhl, A., and Weaver, A., Annual Review of Marine Science, 8, 491–518, https://doi.org/10.1146/annurev-marine-122414-034113, 2016.	n.a.
RD-36	Assimilation of ice concentration in an ice-ocean model	Lindsay, R. W. and Zhang, J., J. Atmos. Ocean. Tech., 23, 742–749, https://doi.org/10.1175/JTECH1871.1, 2006.	n.a.
RD-37	Assimilation of sea ice concentration in a global climate model - physical and statistical aspects	Tietsche S., D. Notz, J. H. Jungclaus, and J. Marotzke, Ocean Science, 9(1), 19-36, 2013.	n.a.
RD-38	Assimilation of ice concentration in a coupled ice–ocean model, using the Ensemble Kalman filter	Lisæter, K. A., Rosanova, J., and Evensen, G., Ocean Dynam., 53, 368–388, https://doi.org/10.1007/s10236-003-0049-4, 2003.	n.a.
RD-39	Benefits of assimilating thin sea ice thickness from SMOS into the TOPAZ system	Xie, J., Counillon, F., Bertino, L., Tian-Kunze, X., and Kaleschke, L., The Cryosphere, 10, 2745–2761, https://doi.org/10.5194/tc-10-2745-2016, 2016.	n.a.
RD-40	Analysis and forecasting of sea ice conditions with three-dimensional variational data assimilation and a coupled ice-ocean model	Caya, A., Buehner M., Carrieres T., J. Atmos. Ocean. Technol., 27:353–369. doi:10.1175/2009JTECHO701.1, 2010.	n.a.
RD-41	Data assimilation of sea ice concentration into a global ocean–sea ice model with corrections for atmospheric forcing and ocean temperature fields	Toyoda T., Fujii Y., Yasuda T., Usui N., Ogawa K., Kuragano T., Tsujino H., and M. Kamachi, J. Oceanogr., 72, 235–262, 2016.	n.a.

Acronym	Title	Reference	Issue
RD-42	Properties of adjoint sea ice sensitivities to atmospheric forcing and implications for the causes of the long term trend of Arctic sea ice	Koldunov, N. V., Köhl, A., and D. Stammer, Clim. Dynam., 41, 227–241, https://doi.org/10.1007/s00382-013-1816-7, 2013.	n.a.
RD-43	Sea ice assimilation into a coupled ocean-sea ice model using ist adjoint	Koldunov, N. V., Köhl, A., Serra, N., and Stammer, D., The Cryosphere, 11, 2265-2281, 2017.	n.a.
RD-44	Assimilation of ice motion observations and comparisons with submarine ice thickness data	Zhang J., Thomas D.R., Rothrock, D.A., Lindsay R.W., Yu, Y., Kwok, R., J. Geophys. Res.-Oceans., 108(C6), 3170, doi:10.1029/2001JC001041, 2003.	n.a.
RD-45	The topaz monitoring and prediction system for the Atlantic and Arctic oceans	Bertino L., and K. A. Lisæter, J. Operational Oceanography, 1(2), 15-18, 2008.	n.a.
RD-46	Estimated decadal changes in the North Atlantic meridional overturning circulation and heat flux 1993–2004	Wunsch, C., and P. Heimbach, J. Phys. Oceanogr., 36(11), 2012–2024. doi:10.1175/JPO2957.1, 2006.	n.a.
RD-47	An eddy-permitting Southern Ocean state estimate	Mazloff, M., Heimbach, P., and C. Wunsch, J. Phys. Oceanogr. 40(5):880–899. doi:10.1175/2009JPO4236.1, 2010.	n.a.
RD-48	Hydrographic preconditioning for seasonal sea ice anomalies in the Labrador Sea	Fenty, I., and P. Heimbach, Journal of Physical Oceanography, 43(5), 863-883, doi:10.1175/JPO-D-12-064.1, 2013.	n.a.
RD-49	Bidecadal thermal changes in the abyssal ocean	Wunsch, C., and P. Heimbach, J. Phys. Oceanogr, 44(8), 2013–2030. doi:10.1175/JPO-D-13-096.1, 2014.	n.a.

Acronym	Title	Reference	Issue
RD-50	Adjoint analysis of the 2007 all time Arctic sea-ice minimum	Kauker, F., Kaminski, T., Karcher, M., Giering, R., Gerdes, R., and Voßbeck, M., Geophys. Res. Lett., 36, L03707, https://doi.org/10.1029/2008GL036323, 2009.	n.a.
RD-51	A finite-volume, incompressible Navier Stokes model for studies of the ocean on parallel computers	Marshall, J., Adcroft, A., Hill, C., Perelman, L., and Heisey, C., J. Geophys. Res.-Oceans, 102, 5753–5766, https://doi.org/10.1029/96JC02775, 1997.	n.a.
RD-52	Global Sea Floor Topography from Satellite Altimetry and Ship Depth Soundings	Smith, W. H., Science, 277, 1956–1962, https://doi.org/10.1126/science.277.5334.1956, 1997.	n.a.
RD-53	The NCEP/NCAR 40-year reanalysis project	Kalnay, E., Kanamitsu, M., Kistler, R., Collins, W., Deaven, D., Gandin, L., Iredell, M., Saha, S., White, G.,Woollen, J., Zhu, Y., Leetmaa, A., Reynolds, B., Chelliah, M., Ebisuzaki,W., Higgins, W., Janowiak, J., Mo, K. C., Ropelewski, C.,Wang, J., Jenne, R., and Joseph, D., Bull. Am. Meteorol. Soc., 77, 437–471, 1996.	n.a.
RD-54	Global, composite runoff fields based on observed river discharge and simulated water balances	Fekete, B., Vorosmarty, C., and N. Grabs, Technical Report, Global Runoff Data Center, Koblenz, Germany, 1999.	n.a.
RD-55	Oceanic vertical mixing: A review and a model with a nonlocal boundary layer parameterization	Large, W. G., McWilliams, J. C., and Doney, S. C., Rev. Geophys., 32, 363–403, https://doi.org/10.1029/94rg01872, 1994.	n.a.

Acronym	Title	Reference	Issue
RD-56	On an efficient numerical method for modeling sea ice dynamics	Zhang, J. and W. D. Hibler, J. Geophys. Res.-Oceans, 102, 8691–8702, https://doi.org/10.1029/96JC03744, 1997.	n.a.
RD-57	Evaluation of the GECCO2 ocean synthesis: transports of volume, heat and freshwater in the Atlantic	Köhl, A., Q. J. Roy. Meteor. Soc., 141, 166–181, https://doi.org/10.1002/qj.2347, 2015.	n.a.
RD-58	Thinning and volume loss of the Arctic Ocean sea ice cover: 2003-2008	Kwok, R., G. F. Cunningham, M. Wensnahan, I. Rigor, H. J. Zwally, and D. Yi, Journal of Geophysical Research, 114, C07005. doi:10.1029/2009JC005312, 2009.	n.a.
RD-59	Recipes for adjoint code construction	Giering, R. and T. Kaminski, ACM T. Math. Softw., 24, 437–474, https://doi.org/10.1145/293686.293695, 1998.	n.a.
RD-60	Generating efficient derivative code with TAF adjoint and tangent linear Euler flow around an airfoil	Giering, R., Kaminski, T., and Slawig, T., Future Gener. Comp. Sy., 21, 1345–1355, https://doi.org/10.1016/j.future.2004.11.003, 2005.	n.a.
RD-61	Coupled sea Ice–Ocean state estimation in the labrador sea and baffin bay	Fenty, I., and P. Heimbach, Journal of Physical Oceanography, 43(5), 884-904, doi:10.1175/JPO-D-12-065.1, 2013.	n.a.
RD-62	An adjoint method for the assimilation of statistical characteristics into eddy-resolving ocean models	Köhl, A. and J. Willebrand, Tellus A, 54, 406–425, https://doi.org/10.1034/j.1600-0870.2002.01294.x, 2002.	n.a.
RD-63	Variability of the meridional overturning in the North Atlantic from the 50-year GECCO state estimation	Köhl, A., and D. Stammer, Journal of Physical Oceanography, 38(9), 1913-1930, doi:10.1175/2008JPO3775.1, 2008.	n.a.

Acronym	Title	Reference	Issue
RD-64	Adjoint-based estimation of eddy-induced tracer mixing parameters in the global ocean	Liu, C., Köhl, A., and Stammer, D., J. Phys. Oceanogr., 42, 1186–1206, 2012.	n.a.
RD-65	ICESat over Arctic sea ice: Estimation of snow depth and ice thickness	Kwok, R., and G. F. Cunningham, Journal of Geophysical Research, 113, C08010, 2008.	n.a.
RD-66	Seasonal forecasts of Arctic sea ice initialized with observations of ice thickness	Lindsay, R., C. Haas, S. Hendricks, P. Hunkeler, N. Kurtz, J. Paden, B. Panzer, J. Sonntag, J. Yungel, and J. Zhang, Geophys. Res. Lett., 39, L21502, doi:10.1029/2012GL053576, 2012.	n.a.
RD-67	Impacts of Sea Ice Thickness Initialization on Seasonal Arctic Sea Ice Predictions	Dirkson, A., Merryfield, W.J., and Monahan, A., Journal of Climate, 30, 1001-1017, DOI: 10.1175/JCLI-D-16-0437.1, 2017.	n.a.
RD-68	How well must climate models agree with observations?	Notz, D., Phil. Trans. R. Soc. A, 373, 20140164, doi:10.1098/rsta.2014.0164, 2015.	n.a.
RD-69	Climate and carbon cycle changes from 1850 to 2100 in MPI-ESM simulations for the Coupled Model Intercomparison Project phase 5	Giorgetta, M. A., et al., J. Adv. Model. Earth Syst., 5, doi:10.1002/jame.20038, 2013.	n.a.
RD-70	Characteristics of the ocean simulations in MPIOM, the ocean component of the MPI-Earth system model	Jungclaus, J. H., N. Fischer, H. Haak, K. Lohmann, J. Marotzke, D. Matei, U. Mikolajewicz, D. Notz, and J. S. von Storch, J. Adv. Model. Earth Syst., 5, 422–446, doi:10.1002/jame.20023, 2013.	n.a.

Acronym	Title	Reference	Issue
RD-71	Arctic sea-ice evolution as modeled by Max Planck Institute for meteorology's Earth system model	Notz, D., F. A. Haumann, H. Haak, J. H. Jungclaus, and J. Marotzke, J. Adv. Model. Earth Syst., 5, 173–194, doi:10.1002/jame.20016, 2013.	n.a.
RD-72	Improved retrieval of sea ice thickness from SMOS and CryoSat-2	Kaleschke, L., X. Tian-Kunze, and N. Maaß, IEEE IGARSS July 26-31, 2015, Milano, Italy, DOI: 10.1109/IGARSS.2015.7327014.	n.a.
RD-73	Sensitivity of CryoSat-2 Arctic sea-ice freeboard and thickness on radar-waveform interpretation	Ricker, R., Hendricks, S., Helm, V., Skourup, H., and Davidson, M., The Cryosphere, 8, 1607-1622, 2014.	n.a.
RD-74	Retrieval of Arctic Sea Ice Parameters by Satellite Passive Microwave Sensors: A Comparison of Eleven Sea Ice Concentration Algorithms	Ivanova, N., O. M. Johannessen, L. T. Pedersen, and R. T. Tonboe , IEEE Trans. Geosci. Rem. Sens. 52.11, 7233– 7246. doi: 10.1109/TGRS.2014.2310136, 2014.	n.a.
RD-75	Insights into brine dynamics and sea ice desalination from a 1-D model study of gravity drainage	Griewank, P.J. and D. Notz, J. Geophys. Res-Oceans 118, 3370–3386, doi: 10.1002/jgrc.20247, 2013.	n.a.
RD-76	A 1-D modelling study of Arctic sea-ice salinity	Griewank, P.J. and D. Notz, The Cryosphere 9, pp. 305–329. doi: 10.5194/tc-9-305-2015, 2015.	n.a.
RD-77	Microwave emission model of layered snowpacks	Wiesmann, A. and C. Mätzler, Remote Sensing of Environment 70, pp. 307–316, 1998.	n.a.

Acronym	Title	Reference	Issue
RD-78	Sea ice emission modelling	Tonboe, R., S. Andersen, L. Toudal, and G. Heygster, In: Thermal Microwave Radiation - Applications for Remote Sensing. Ed. by C. Mätzler, P.W. Rosenkranz, A. Battaglia, and J.P. Wigneron. IET Electromagnetic Waves Series 52, pp. 382–400, 2006.	n.a.
RD-79	Inter-comparison and evaluation of sea ice algorithms: towards further identification of challenges and optimal approach using passive microwave observations	Ivanova, N., L.T. Pedersen, S. Kern, G. Heygster, T. Lavergne, A. Sørensen, R. Saldo, G. Dybkjaer, L. Brucker, and M. Shokr, The Cryosphere, 9, 1797-1817. doi: 10.5194/tc- 9-1797-2015, 2015.	n.a.

Table 0-1: Reference Documents

1.6 Acronyms and Abbreviations

Acronym	Meaning
AMSR-E	Advanced Microwave Scanning Radiometer aboard EOS
AO	Announcement of Opportunity
ASCII	American Standard Code for Information Interchange
ASIRAS	Airborne Synthetic Aperture and Interferometric Radar Altimeter System
ATBD	Algorithm Theoretical Basis Document
CM-SAF	Climate Monitoring Satellite Application Facility
DMSP	Defence Meteorological Satellite Program
DWD	Deutscher Wetterdienst
EASE2	Equal-Area Scalable Earth Grid 2
ECV	Essential Climate Variable
Envisat	Environmental Satellite
ERS	European Remote Sensing satellite
ESA	European Space Agency
EUMETSAT	European Organisation for the Exploitation of Meteorological Satellites
FB	Freeboard
FCDR	Fundamental Climate Data Record
FOC	Free of Charge

Acronym	Meaning
FOV	Field-of-View
FTP	File Transfer Protocol
GB	GigaByte
GCOM	Global Change Observation Mission
H	Horizontal polarization
H+V	Horizontal and vertical polarization
L1B	Level 1b
MB	MegaByte
MODIS	Moderate Resolution Imaging Spectroradiometer
MSS	Mean Sea Surface
n.a.	Not applicable
NetCDF	Network Common Data Format
NSIDC	National Snow and Ice Data Center
OCOG	Offset Centre of Gravity
OIB	Operation Ice Bridge
OSI-SAF	Ocean and Sea Ice Satellite Application Facility
OW	Open Water
PHC	Polar Science Centre Hydrographic Climatology
PI	Principal Investigator
PMW	Passive Microwave
POES	Polar Operational Environmental Satellite
PRF	Pulse Repetition Frequency
RA	Radar Altimeter
RADAR	Radio Detection and Ranging
SAR	Synthetic Aperture Radar
SGDR	Sensor Geophysical Data Record
SIA/SIE	Sea Ice Area / Sea Ice Extent
SIC	Sea Ice Concentration
SIRAL	SAR/Interferometric Radar Altimeter
SIT	Sea Ice Thickness
SMMR	Satellite Multichannel Microwave Radiometer
SSM/I	Special Sensor Microwave / Imager
SSM/IS	Special Sensor Microwave / Imager+Sounder
TB	TeraByte
t.b.d.	To be determined
TM	Thematic Mapper
ULS	Upward Looking Sonar
URL	Uniform Resource Locator
V	Vertical polarization
WGS84	World Geodetic System revision -84

Table 0-2: Acronyms

2 Preface

The SICCI-2 products are described in the Product User Guide (PUG) [RD-01]. The algorithms used to obtain the products are described in the Algorithm Theoretical Basis Document (ATDB) [RD-02] and the production chains used are explained in the Detailed Processing Model (DPM) document [RD-03]. The Product Validation and Intercomparison Report (PVIR) [RD-04] describes the results of the evaluation efforts. Data used for some of the inter-comparison studies found in this report are given in the DARD [RD-05]

The results presented in this report are based on v2.0 and v2.1 of the SIC product and v1.0 of the SIT product. Both were downloaded from the Integrated Climate Data Center (ICDC) website http://icdc.cen.uni-hamburg.de/esa-cci_sea-ice-ecv0.html?&L=1.

3 Sea-ice area and extent, volume and volume flux

SICCI-2 project products of sea ice concentration (SIC) are available for both hemispheres year-round for the time periods: 06/2002-09/2011 (AMSR-E) and 07/2012-04/2017 (AMSR2). Sea-ice thickness (SIT) products are available for the Southern Hemisphere year-round for the time period 05/2002 through 04/2015, and for the Northern Hemisphere for winters 2002/03 through 2016/17 – based on Envisat RA-2 (until 03/2012) and CS-2) (since 11/2010) data. Winters comprise the months October to April.

This section is going to describe the computation of sea-ice area and extent based on the SICCI-2 SIC data. It will elaborate on the uncertainty estimates of this computation developed in phase 1 of the SICCI project.

This section is also going to describe the computation of the sea-ice volume computed solely from SICCI-2 SIC and SIT data. In addition, by adding information about sea-ice motion, this section will give results from sea-ice volume flux computations across key flux gates / transect lines.

3.1 Sea ice area and extent

For both hemispheres sea-ice area (SIA) and sea-ice extent (SIE) were computed from the variable 'ice_conc' using a SIC threshold of 15%, separately for grid resolutions of 12.5km, 25km and 50km. Information from the flag layer was not included. No effort was undertaken to block-average fine-resolution data to coarse-resolution data. No effort was undertaken to use the same land-mask or modify the data such that the same (coarse) land-mask is used in all three data sets.

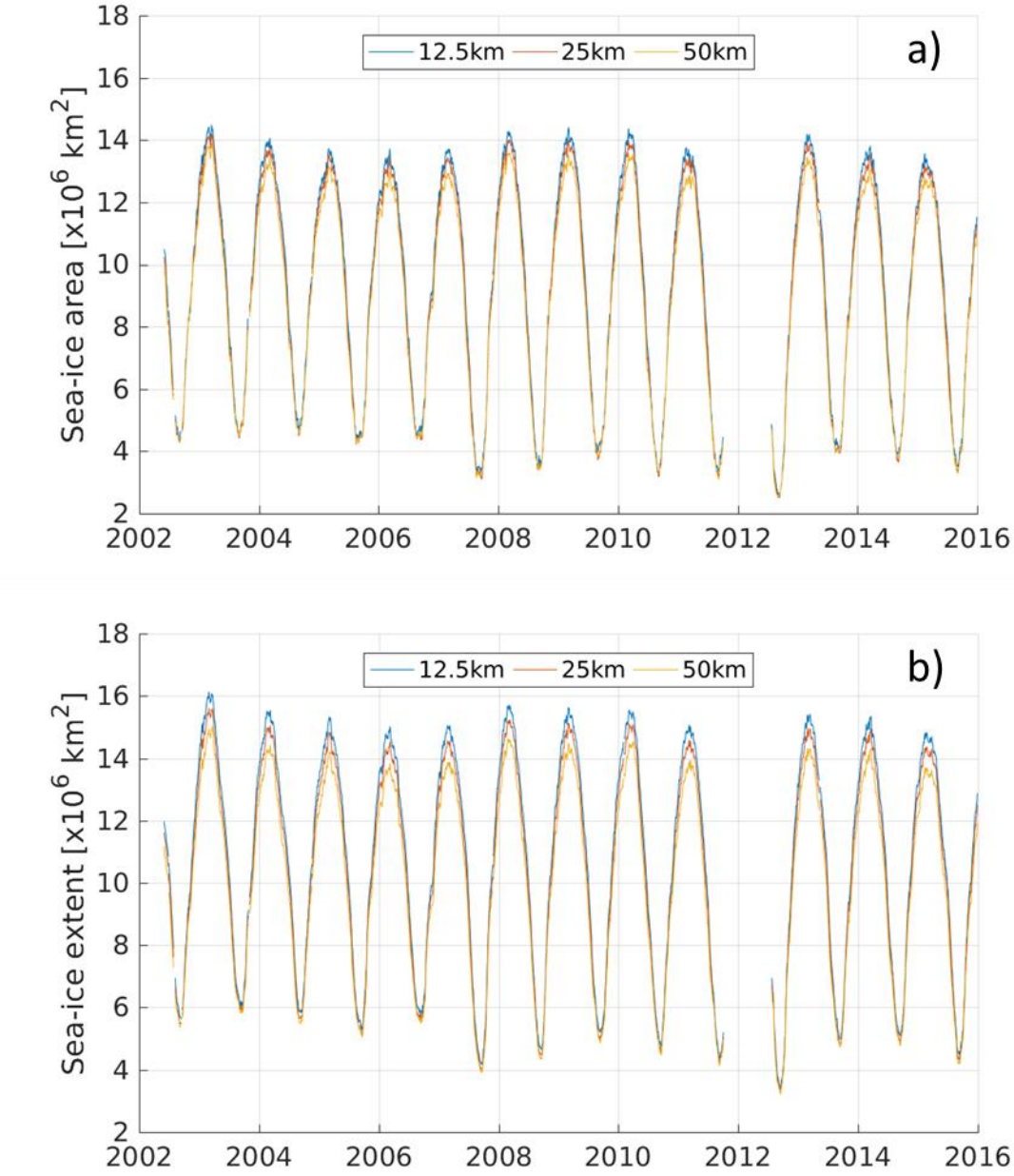

Figure 3-1: Time-series of the sea-ice area (a) and the sea-ice extent (b) for the northern hemisphere as computed from the SICCI phase-2 sea-ice concentration data set for the three different grid resolutions (algorithms) denoted by the different colors.

The following observations can be made:

There seems to be a smooth transition between AMSR-E and AMSR2; both SIA and SIE exhibit the record minimum in summer 2012 and the increase by about 1 million square kilometer from the summer minimum 2012 to the summer minimum in 2013. This observation (above) can be made for all three algorithms.

The algorithm with the coarsest grid resolution (50 km) provides the lowest SIE and SIA maximum and minimum values while the one with the finest grid resolution (12.5 km) provides the highest SIE and SIA maximum and minimum values. During the winter maximum the difference between coarse and fine resolution is between 500 000 km² and 1 000 000 km² for the SIA and generally around 1 000 000 km² for SIE. During the summer minimum these differences do not exceed 500 000 km².

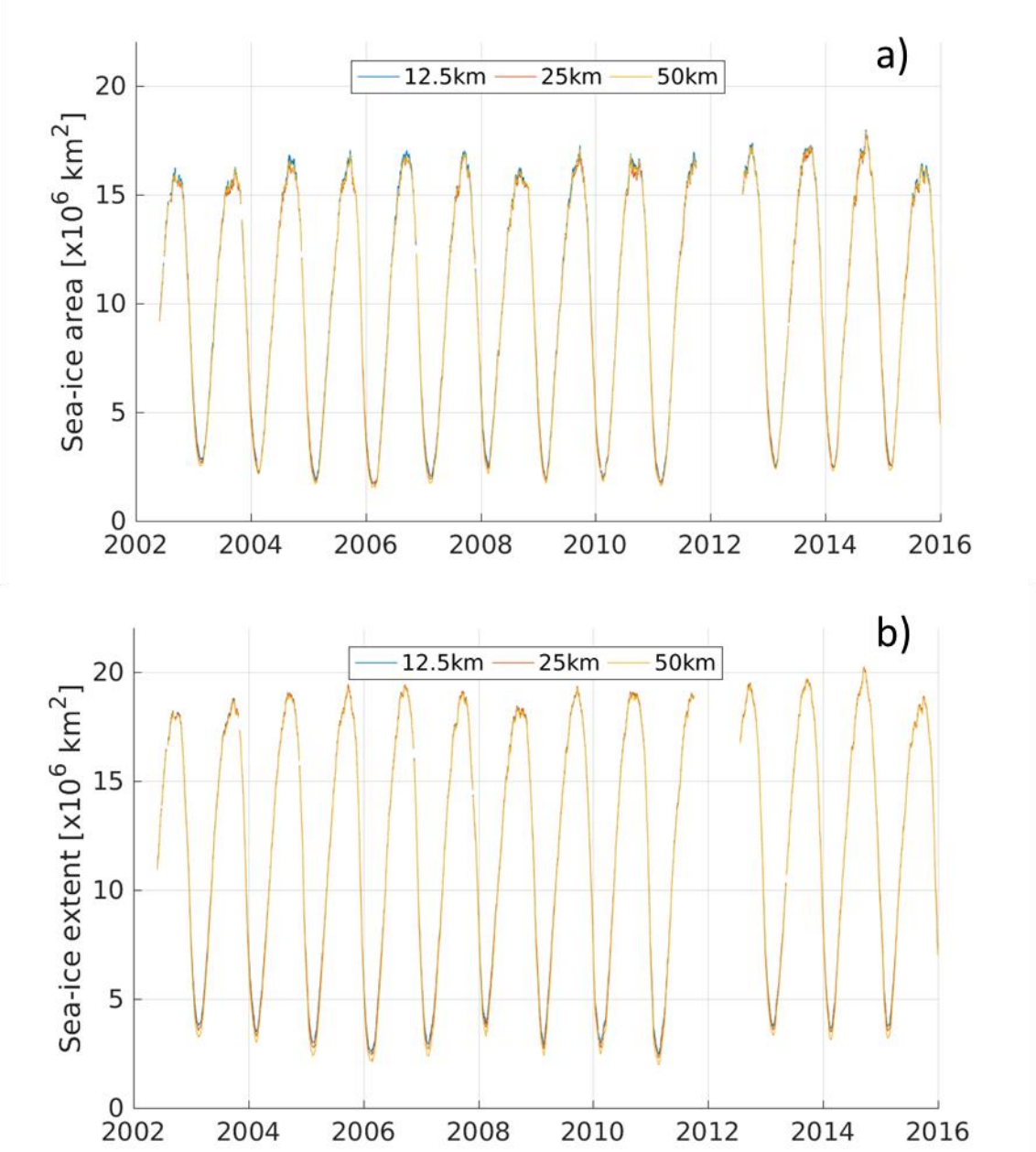

Figure 3-2: Time-series of the sea-ice area (a) and the sea-ice extent (b) for the southern hemisphere as computed from the SICCI phase-2 sea-ice concentration data set for the three different grid resolutions (algorithms) denoted by the different colors.

The following observations can be made for the southern hemispheric SIA and SIE time series:

Also in the southern hemisphere there is a smooth transition between AMSR-E and AMSR2 with the development of the maximum SIA and SIE during the last 5 years as observed by other algorithms (peak in 2014 and drop in 2015).

Differences in SIA and SIE between the different grid resolutions / algorithms are smaller than in the northern hemisphere if existent at all. For the summer minimum SIA and SIE the same order as for the northern hemisphere applies, i.e. largest values for the fine resolution and lowest values for the coarse resolution; the difference amount ~ 500 000 km² for SIE and less than that for SIA. For the winter maximum period, SIA values are almost the same while SIE values are maximal at 12.5 km followed less strictly by 25 km like in the northern hemisphere; in several winters SIA at 12.5 km is closer to SIA at 50 km than at 25 km. During winter maximum differences are smaller than 500 000 km².

The small differences in winter-time SIA and SIE in the southern hemisphere suggest that all three algorithms more or less provide the same sea-ice concentration. The fact that winter-time SIA and SIE in the northern hemisphere differ considerably between the three algorithms could partly be caused by a different treatment of first-year ice (FYI) and multiyear ice (MYI). It seems more likely though that this is caused by the different grid resolution and hence the different land fraction in the investigated domain. This idea seems to be supported by the fact that the difference between the three algorithms stays almost as large during summer-time and that also in the southern hemisphere differences between the algorithms (grid resolutions) become notable during summer-time when the contribution of the different land-fractions has a larger impact than during winter.

How does the SICCI-2 product harmonize with the OSI-SAF OSI-450 one [RD-06]? This is illustrated by means of sea-ice area and extent in Figure 3-3 through Figure 3-6. With regard to the Arctic sea-ice area (Figure 3-3) we find that SICCI-25km provides the same seasonal amplitude than OSI-450. We see the tendency that SICCI-25km sea-ice area is slightly smaller than OSI-450 sea-ice area – particularly during the melt phase which we attribute the finer native resolution of the AMSR-E / AMSR2 sensors (SICCI-25km) compared to SSMIS (OSI-450).

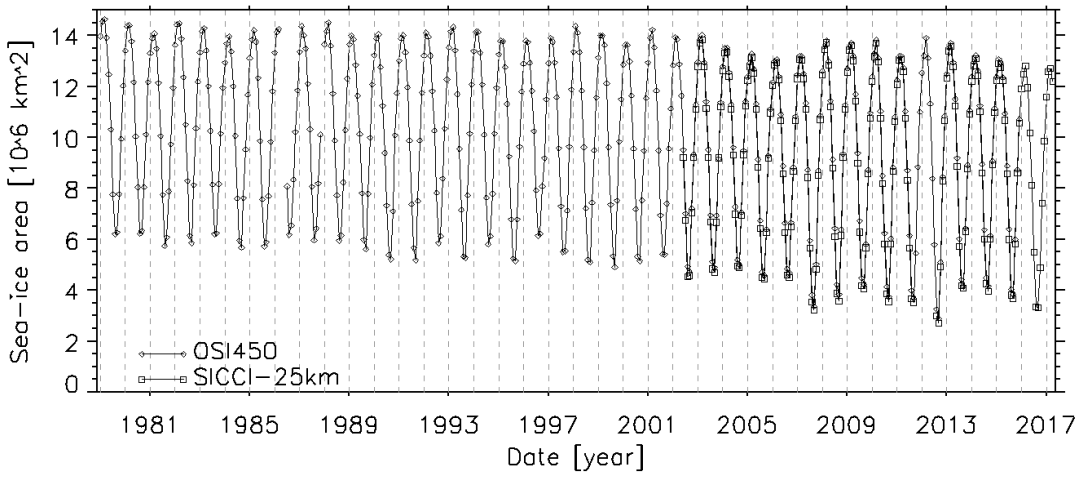

Figure 3-3: Time series of the combined Eumetsat OSISAF OSI-450 and the ESA-SICCI2 SICCI-25km sea-ice area for the Arctic.

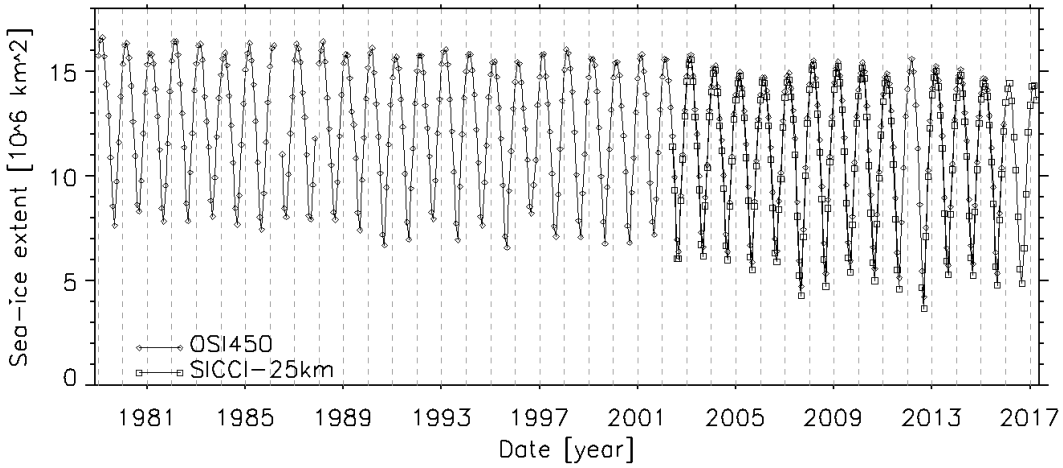

Figure 3-4: As Figure 3-3 but for the Arctic sea-ice extent.

The same finding applies to the Arctic sea-ice extent (Figure 3-4). We find a difference between OSI-450 and SICCI-25km of about 500 000 km² (SICCI-25 km < OSI-450) at the end of melting period for most of the overlapping years. This difference exists for the freezing limb of the seasonal cycle as well, but values are much smaller.

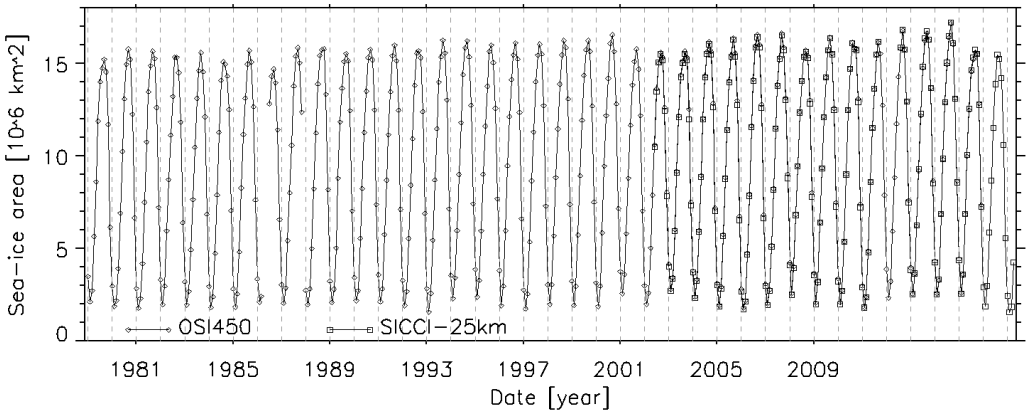

Figure 3-5: As Figure 3-3 but for the Antarctic sea-ice area.

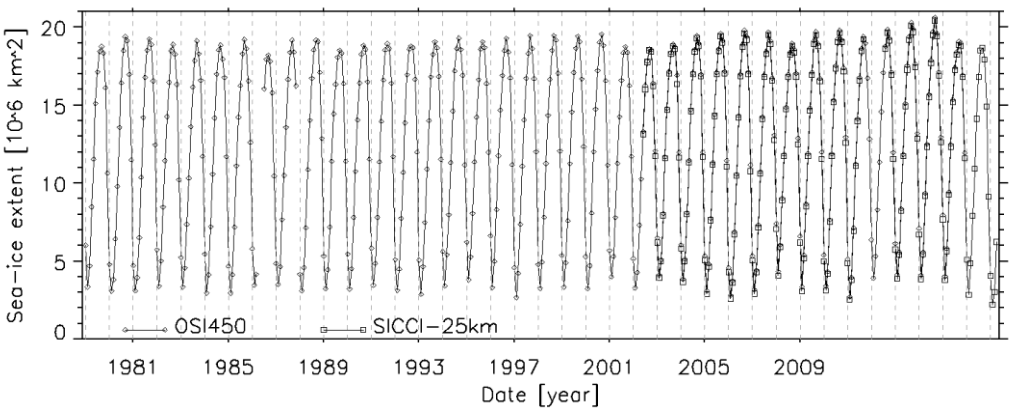

Figure 3-6: As Figure 3-5 but for the sea-ice extent.

For the Antarctic sea-ice area (Figure 3-5) and extent (Figure 3-6) we make the same observation as in the Arctic. Actually, the agreement between OSI-450 and SICCI-25km is better in the Antarctic. During the melting limb of the seasonal cycle we can find differences between OSI-450 and SICCI-25km of the same kind as in the Arctic (SICCI-25km < OSI-450), however; these differences are again larger for the extent than the area and may peak also at ~500 000 km² in December, the month of peak melt.

How do OSI-450 and SICCI-25km compare the Arctic sea-ice index which is based on the NASA-Team algorithm? This is illustrated for months March and September in Figure 3-7.

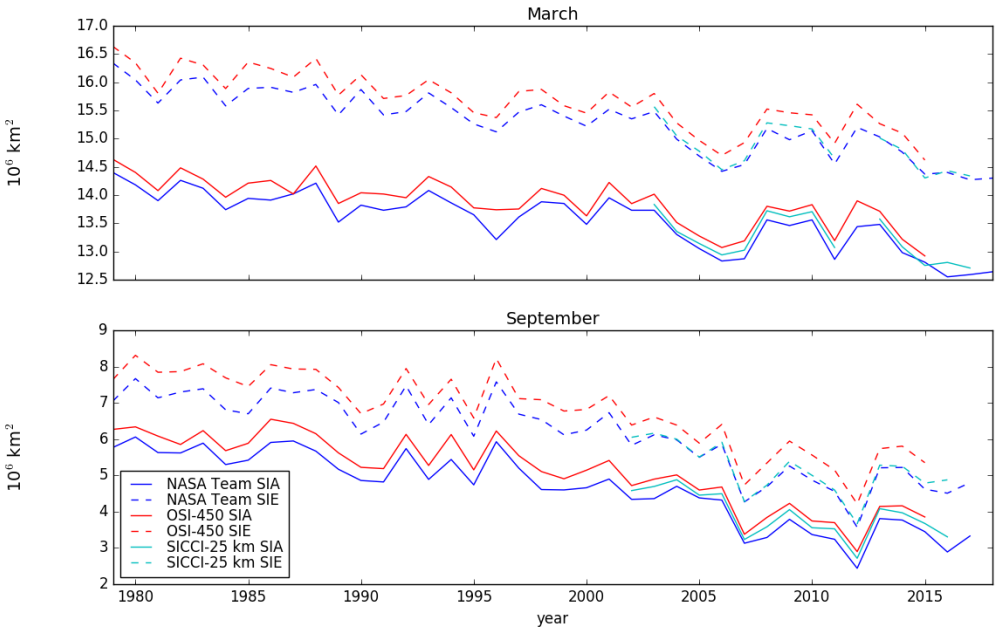

Figure 3-7: Time series of the monthly mean sea-ice area (SIA) and extent (SIE) for (in blue) the NASA-Team algorithm (NSIDC sea-ice index https://nsidc.org/data/seaice_index), (in red) OSI-450, and (in green) SICCI-25km.

We find that the sea-ice extents from NASA-Team and OSI-450 match almost perfectly well with respect to the inter-annual variability with OSI-450 being about 200 000 km² (500 000 km²) larger than NASA-Team in March (September). We find an almost perfect agreement in the sea-ice extent between NASA-Team and SICCI-25km; larger deviations can only be seen for September 2016 and March 2009.

We find that the sea-ice areas from NASA-Team and OSI-450 match less well with respect to the inter-annual variability than the sea-ice extents but the agreement is still very good. This comes not unexpected because potential differences between the algorithms at, e.g., intermediate sea-ice concentrations would be visible in the sea-ice area but the extent. Like for the sea-ice extent there is a systematic bias of ~200 000 km² (March) and

~300 000 km² (September) with OSI-450 > NASA-Team. Sea-ice area from SICCI-25km ranges between the two other products without particularly following one of these throughout the period of overlap shown.

3.2 Sea ice volume

We derived the monthly average sea-ice volume for both hemispheres for both, the Envisat and the CryoSat-2 periods. This was done using the sea-ice thickness of the SICCI-2 product, using only values with status-flag = 0. Instead of using the monthly mean SIC also provided with the product, we used the SICCI-2 SIC product. The gap (October 2011 through July 2012) we filled with OSI-450 SIC data based on SSMIS [RD-06]. While we used SICCI-25km for the Arctic we used SICCI-50km for the Antarctic; in that case we averaged the OSI-450 SIC to the same grid resolution. Volume was computed as the product of SIC, grid cell area and SIT. Grid cell area was 25 km x 25 km for the Northern and 50 km x 50 km for the Southern Hemisphere.

We compute the sea-ice volume SIV as: $V = I * A$ where V is volume, I is the true sea-ice thickness (not the grid-cell mean) and A is sea-ice area which is computed as $A = C * A_{grid}$ with sea-ice concentration C (as a fraction of grid cell area) and A_{grid} the grid cell area.

We use a sea-ice concentration threshold of 60% (or 0.6) to compute A and hence V.

Both CDRs (SIC and SIT) provide estimates of the uncertainty which allows us to also provide an estimate of the uncertainty of V. However, the uncertainty of the sea-ice thickness is so large that we would end up with uncertainties of V that would be so large that the seasonal variation in V would completely fall into the range of its uncertainty. As a preliminary solution we therefore scale the uncertainty proportional to the sea-ice thickness: $\sigma_I = 0.33 * I$. We compute the uncertainty in V, σ_V, as follows: $\sigma_V = \Sigma((\sigma_C * I)^2 + (C * \sigma_I)^2)$ with the total standard error in C: σ_C .

The SIT CDR might have data gaps where the SIC CDR indicates SIC > 60%. In order to avoid an under-estimation of V due to these gaps, which can be up to 10% in V, we interpolated the spatial gaps from nearby SIT values. A minimum of 5 SIT values is required for a box spanning 13 x 13 grid cells for the Arctic and 7 x 7 grid cells in the Antarctic; that is an area of ~ 350 km x 350 km.

The SICCI-2 sea-ice thickness retrieval uses the Warren et al. (1999) [RD-07] snow-depth climatology for snow depth and snow density. Because this climatology is only valid over the Arctic Ocean but not in the peripheral seas like the Hudson Bay or Barents Sea, or the Canadian Arctic Archipelago, we limit the computation of the sea-ice volume to the sector "Arctic Ocean". The grid cells belonging to this sector are derived from the Arctic sector mask provided originally by NSIDC on polar-stereographic grid and modified by NSIDC (personal communication, W. Meier and S. Steward, NSIDC, 2018).

Finally, and most crucially, for the Arctic for both sensors exist a large circular area centered at the Pole where no observations are made due to the satellites' orbit inclination. This does not apply to the Antarctic. We fill this hole by interpolation. This region of no observations begins at ~81.5°N for Envisat and at ~88.5°N for Cryosat-2. For Cryosat-2 we compute the

mean SIC and mean SIT of the ring north of 87.0°N (Figure 3-8 and Figure 3-9); for Envisat we compute the mean SIC and mean SIT of the ring north of 81.0°N (Figure 3-10 and Figure 3-11).

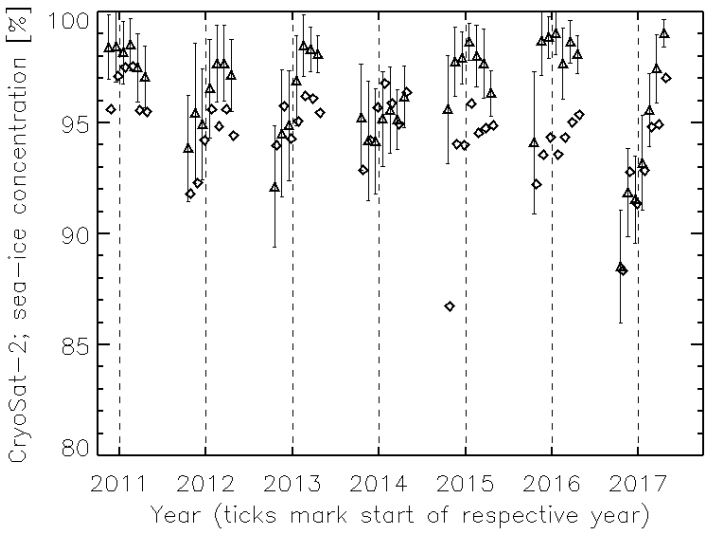

Figure 3-8: Mean sea-ice concentration of the area north of 87°N used for the sea-ice volume based on Cryosat-2 sea-ice thickness data (triangles); diamonds show the mean sea-ice concentration obtained for the ring 81.0°N to 81.5°N potentially used to continue the Envisat-based sea-ice volume time series.

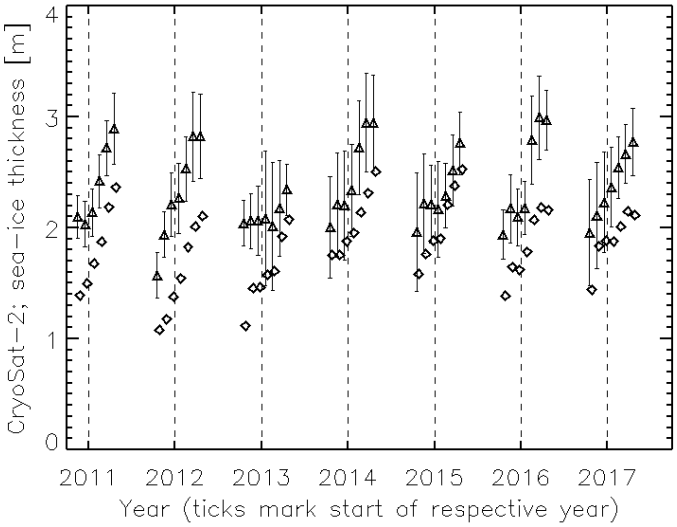

Figure 3-9: As Figure 3-8 but showing the mean Cryosat-2 sea-ice thickness for the area north of 87.0°N (triangles) and the ring 81.0°N to 81.5°N (diamonds).

For the Arctic, the final sea-ice volume is then computed as $V = V_{valid} + V_{interp} + V_{polehole}$. Here V_{valid} , V_{interp} , and $V_{polehole}$ are the volume computed from all grid cells up to the altimeter observation gap at the pole, the volume resulting from the grid cells of valid SIC values but missing SIT values, and the volume of the altimeter observation gap area, respectively.

For the Antarctic it is $V = V_{valid} + V_{interp}$.

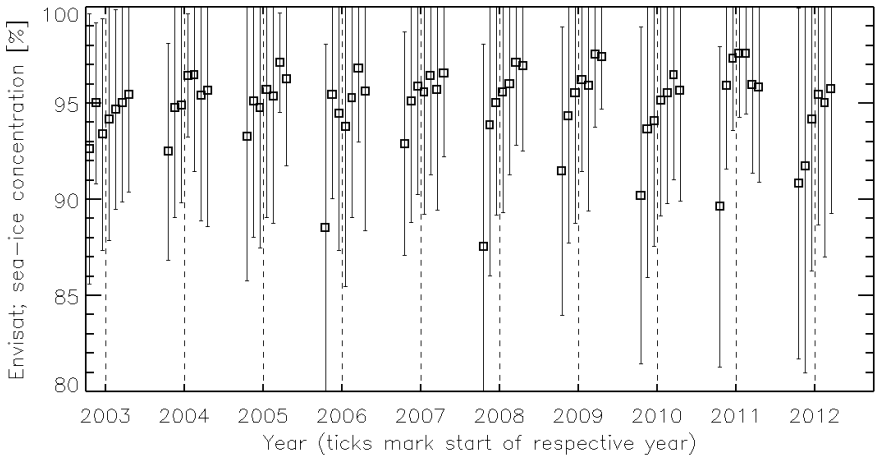

Figure 3-10: Mean sea-ice concentration of the ring area between 81.0°N and 81.5°N used for the sea-ice volume based on Envisat sea-ice thickness data.

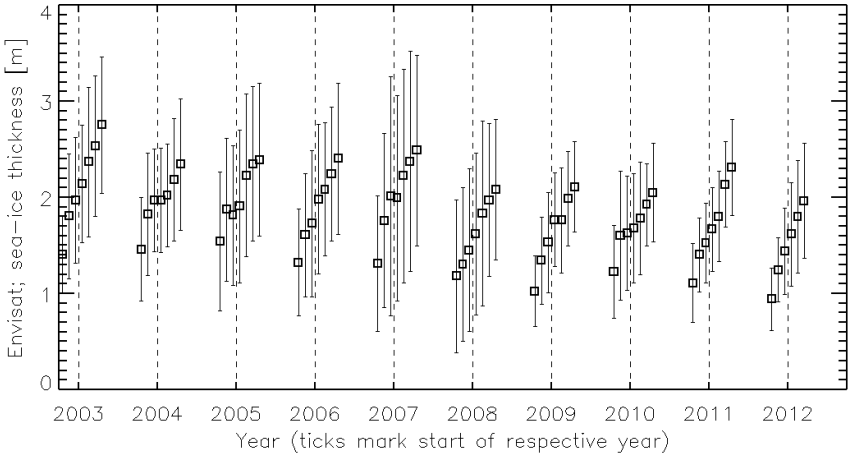

Figure 3-11: As Figure 3-10 but showing the mean Envisat sea-ice thickness for the ring between 81.0°N and 81.5°N.

Figure 3-8 through Figure 3-11 illustrate how variable the mean SIC and SIT values are that are used to fill the gap of observations at the pole. Not surprisingly, the mean SIC and SIT values for the CS-2 observation gap are higher (Figure 3-8 and Figure 3-9) than those for the Envisat observation gap (Figure 3-10 and Figure 3-11). It seems to be advisable therefore, when constructing a consistent SIV time series, to rely on the full CS-2 SIV time series, and to carry out a bias correction for the Envisat SIV time series. This is done by taking the overlapping period and computing the difference between Envisat SIV and CS-2 SIV for every month. The respective monthly SIV difference is then added to the corresponding Envisat SIV value of the period 10/2002 through 10/2010 (Arctic) and 06/2002 through 10/2010 (Antarctic). For those months where the overlap period contains two months the arithmetic mean of the monthly differences is taken.

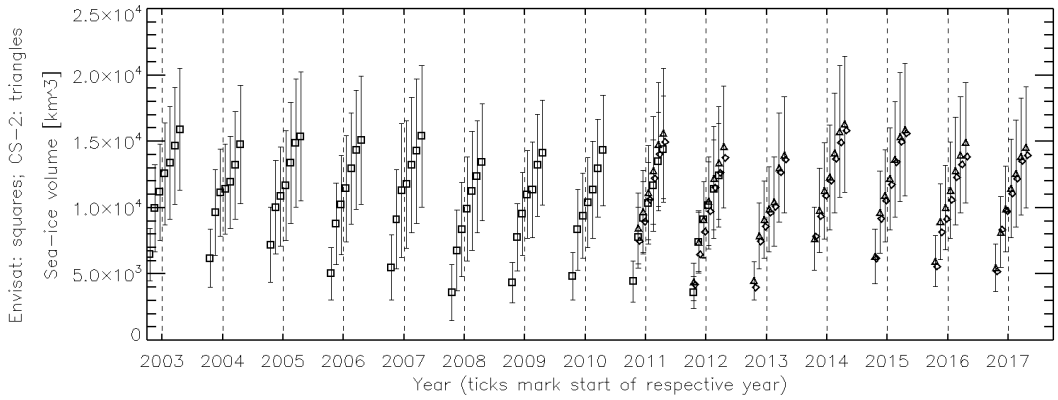

Figure 3-12: Arctic Ocean sector (see text) sea-ice volume time series from Envisat (squares) and CS-2 (triangles) together with a the volume uncertainty estimate.

In Figure 3-12 we show the SIV time-series computed from both sensors in one plot. Differences in the overlap period are within the uncertainty but still large enough to call for a bias correction. The diamonds shown for the CS-2 period denote an attempt to extend the Envisat SIV time-series into the CS-2 period instead of the CS-2 SIV time-series into the Envisat period. The SIV difference between the diamonds and the triangles is surprisingly small. What we did here is the following: We took CS-2 data and computed the mean SIT for the same ring used to fill the Envisat observation gap at the pole and also computed the mean SIC for the same area. Subsequently, we considered the CS-2 observation hole at the pole as large as the one for Envisat and "filled" it by using the just computed mean SIT and SIC values. Despite the small difference we decided to carry out the bias correction as described further above – mainly because in the evaluation CS-2 has been shown to provide a more accurate freeboard and hence sea-ice thickness. Also in terms of the resolution of the sea-ice thickness variability CS-2 is certainly the better choice. Hence, in Figure 3-13 we provide the final, consistent Arctic Ocean sector sea-ice volume time series. It is based on CS-2 SIV for the CS-2 period and on bias-corrected Envisat SIV for the Envisat period until including October 2010.

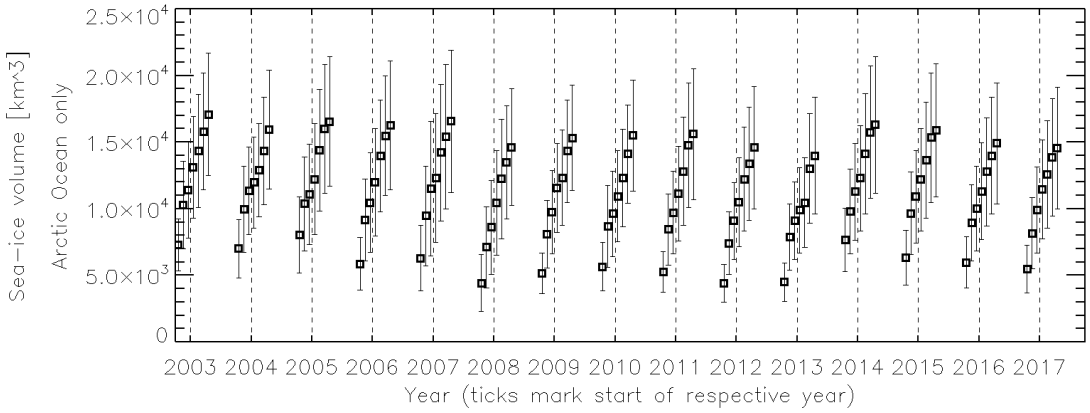

Figure 3-13: Arctic Ocean sector consistent sea-ice volume time series.

If we take ~5 000 km³ and 20 000 km³ as useful ballpark numbers for the SIV at the beginning and end of the freezing season, as suggested by PIOMAS (Figure 3-14), then our estimates are at a reasonable magnitude in October / November but increasingly under-estimate PIOMAS SIV later in the freezing season. This can be attributed to the different regions used. PIOMAS uses a pan-Arctic domain (http://psc.apl.washington.edu/zhang/IDAO/z_arctic1 .gif).

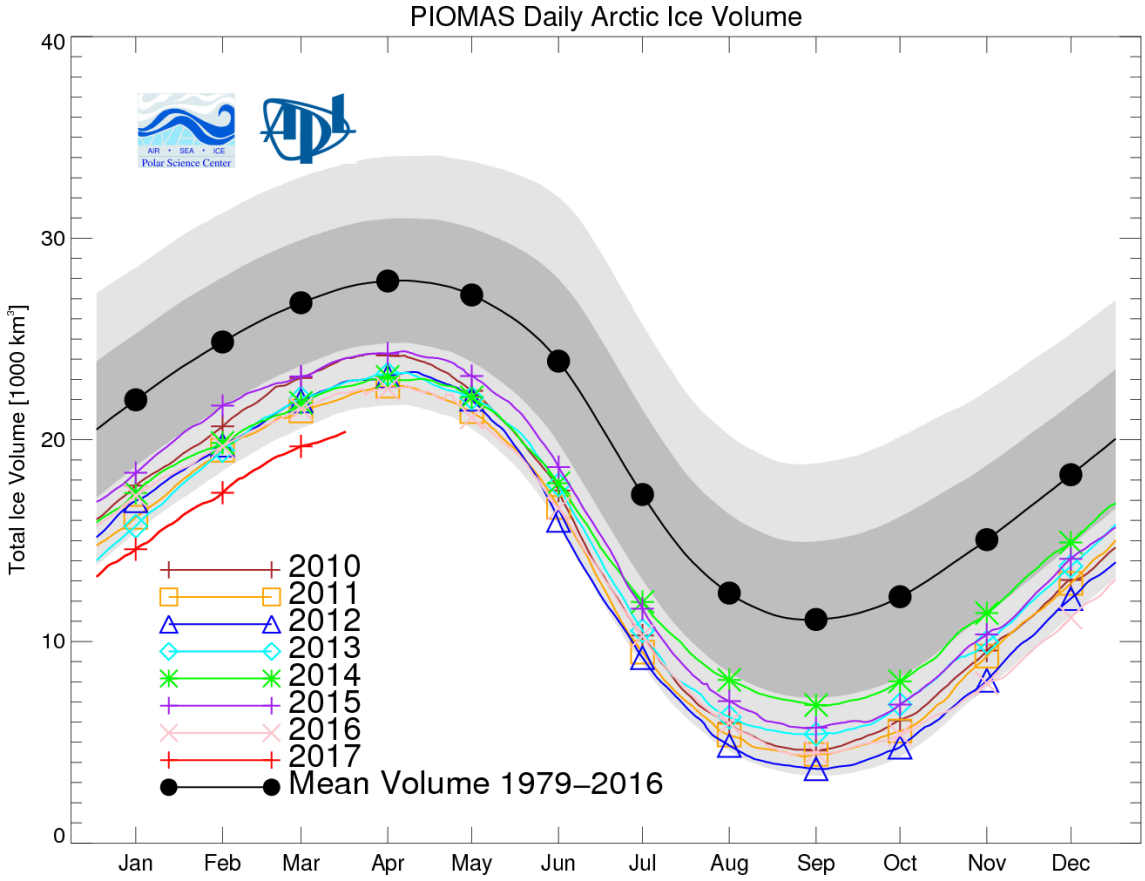

Figure 3-14: PIOMAS estimates of the Arctic Ocean sea-ice volume (from NSIDC: http://nsidc.org/arcticseaicenews/files/2017/04/PIOMAS_figure_March2017.png).

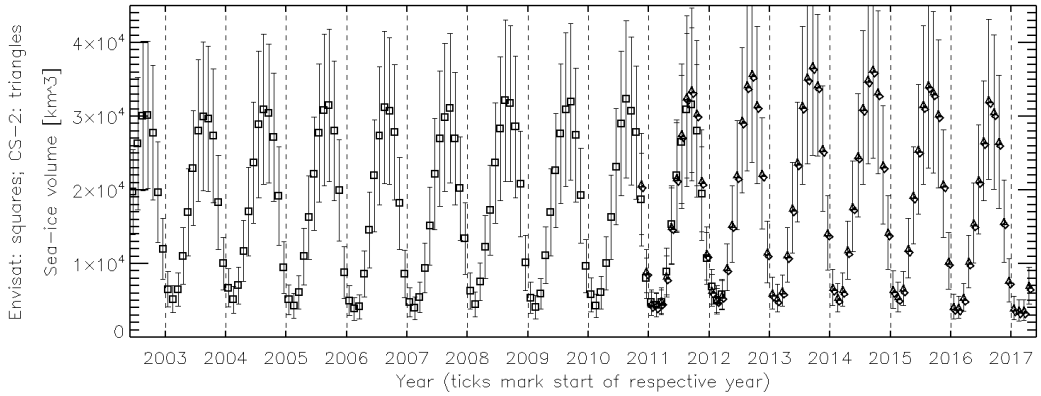

Figure 3-15: As Figure 3-13 but for the Southern Hemisphere; squares are for Envisat, triangles for CS-2, and diamonds denote extension of the Envisat SIV time series using the overlap period (see text).

The Southern Hemisphere sea-ice volume derived with Envisat and CS-2 is shown in Figure 3-15. We find a reasonable seasonal cycle with minimum values in February of ~ 5 000 km³ and maximum values in August / September of ~28 000 km³. We find an increase in the SIV between the Envisat and the CS-2 era for the time period shown; extension of the time series with data from the recent two years with substantial reductions in the sea-ice cover of the Southern Hemisphere [RD-08] might change this view.
We note that our values are more than twice as large as those published based on ICESat-1 SIV estimates by Kurtz and Markus [RD-09] – results which have been discussed to be very likely too low, however ([RD-10], RD-11]).
In order to obtain a consistent SIV time series here as well we tried to extend the Envisat SIV time series into the CS-2 measurement period (diamonds in Figure 3-15). However, given the possibly higher accuracy of CS-2 also in the Southern Ocean and also the better data coverage [RD-12] we find it more reasonable to carry out a bias correction the same way we did it for the Arctic (see above). The resulting consistent Antarctic sea-ice volume time-series, which is based on CS-2 SIV data starting from 11/2010 and on bias-corrected Envisat SIV data from 06/2002 through 10/2010 is shown in Figure 3-16.

We finally note that both sea-ice volume time-series are available under http://icdc.cen.uni-hamburg.de/projekte/esa-cci-sea-ice-ecv0.html

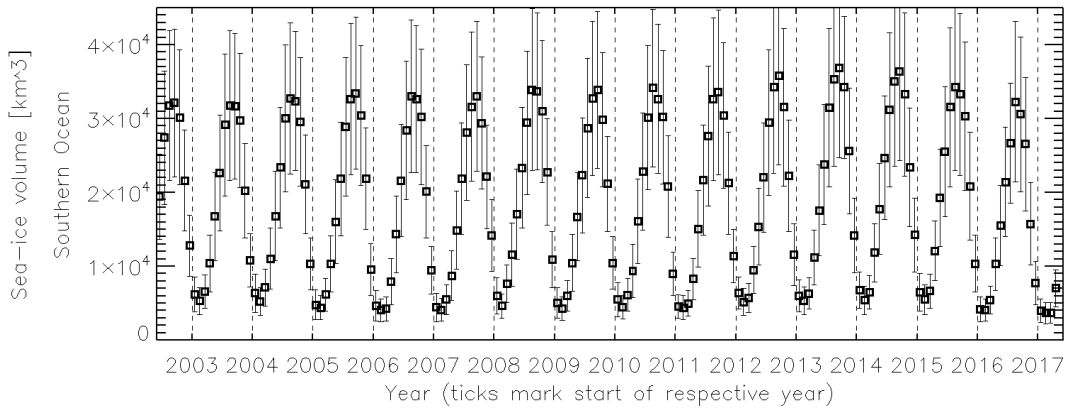

Figure 3-16: As Figure 3-13 but for the Antarctic.

3.3 Sea ice volume flux

For the sea-ice volume flux we co-locate the NSIDC sea-ice motion data set v03 [RD-13] at monthly temporal resolution, available until including Feb. 2017 with the SICCI-2 SIT and with monthly averaged SIC data from SICCI-2. Like in section 3.2 we use SICCI-25km for the Arctic and SICCI-50km for the Antarctic and bridge the gap between AMSR-E and AMSR2 with OSI-450 SIC data. In both hemispheres we chose a number of zonal and meridional flux gates. These are illustrated in Figure 3-17 for the Arctic and in Figure 3-28 for the Antarctic. For the zonal flux gates, i.e. an ice flow in zonal (west←→east) direction, we only used the u-component of the sea-ice motion. For the meridional flux gates, i.e. an ice flow in meridional (north←→south) direction, we only used the v-component of the sea-ice motion.

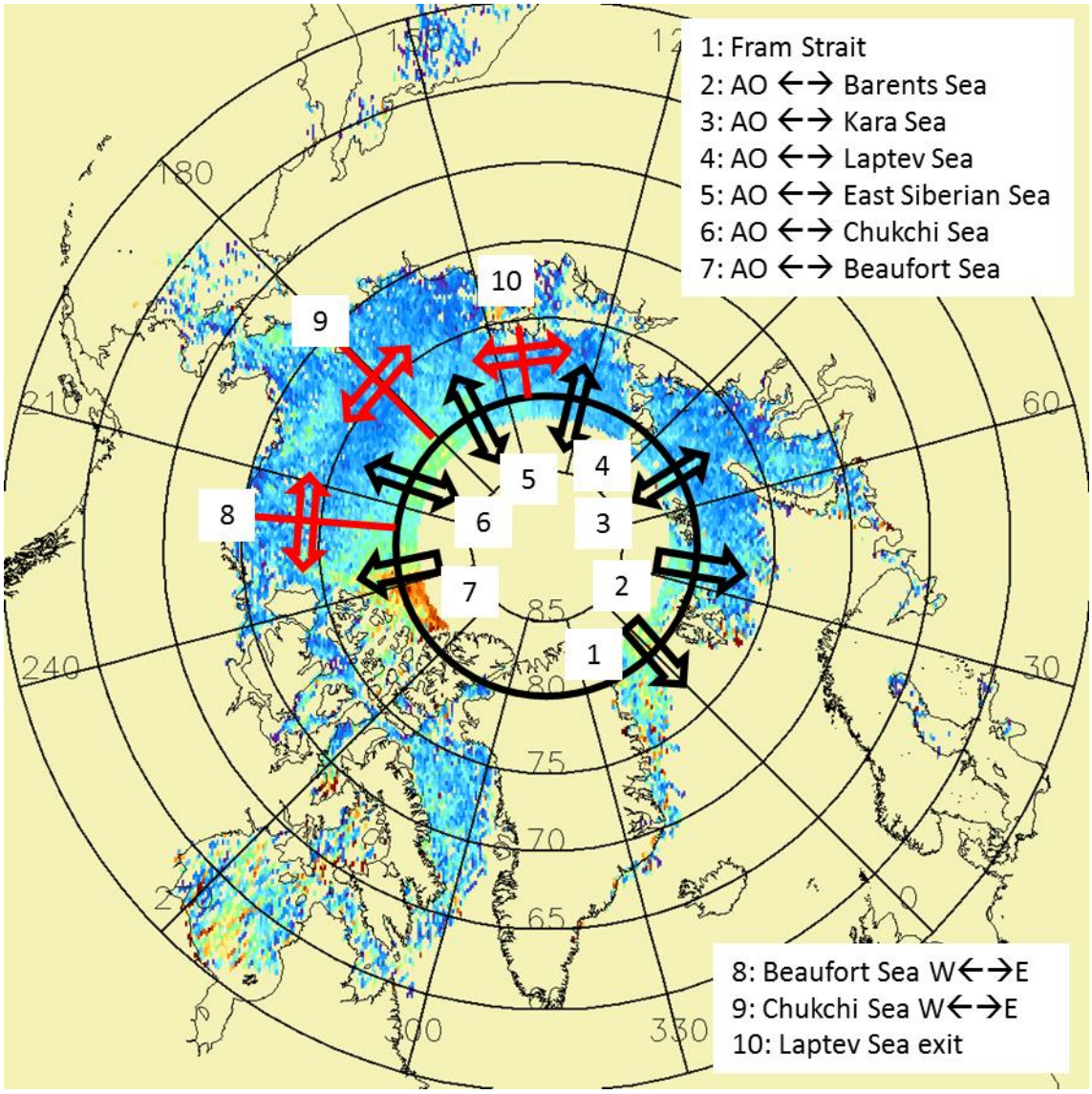

Figure 3-17: Locations of the flux gates in the Arctic. We have 7 meridional (numbers 1 to 7) and 3 zonal (numbers 8 to 10) flux gates. AO refers to Arctic Ocean. Background is a typical winter-time sea-ice thickness distribution.

In the following we show and describe first the sea-ice volume flux (SIVF) for the Arctic flux gates. We only show SIVF time-series where we plot data obtained from both sensors, Envisat and CS-2. In contrast to the sea-ice volume we did not carry out a bias correction to create a more consistent time series (compare Figure 3-13 and Figure 3-16). Note that SIVF is only computed for months October through April, i.e. the freezing season. Note further that the sign of the SIVF follows the direction of the sea-ice motion. A northward (southward) meridional flux (gates #1 to #7, Figure 3-17) is positive (negative). An eastward (westward) zonal flux (gates #8 to #10, Figure 3-17) is positive (negative).

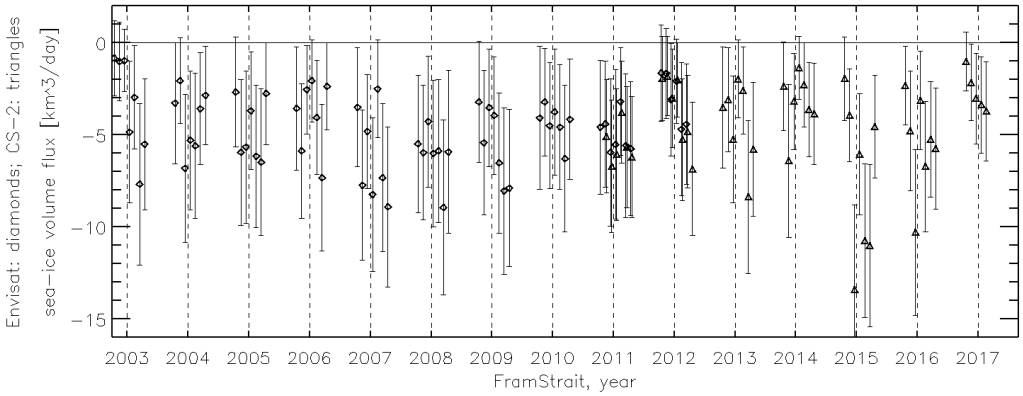

Figure 3-18: Sea-ice volume flux time-series for flux gate #1: Fram Strait (see Figure 3-17).

In agreement with previous studies the SIVF through Fram Strait (Figure 3-18) is negative, i.e. directed outward of the Arctic Ocean, a sea-ice export out of the Arctic. Typical values vary between 2 km³/day and 8 km³/day – summing up to a cumulative ice export of ~1000 km³ during winter (October through April). Exceptional is the winter 2014/15 when exports peaked at > 10 km³/day during three months with a total winter cumulative ice export through Fram Strait of ~1600 km³. These values are smaller than those reported by [RD-14] based on ICESat data analysis of the period 2003 through 2008. Their estimates of the mean SIVF through Fram Strait at 80°N range between 100 km³ and 300 km³ per month, while ours range between ~60 km³ and ~200 km³ per month.

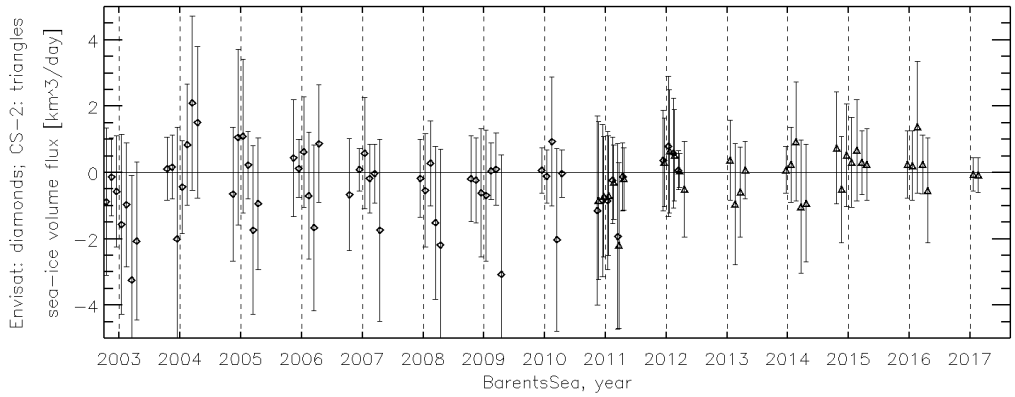

Figure 3-19: Sea-ice volume flux time-series for flux gate #2: Arctic Ocean ←→ Barents Sea (see Figure 3-17).

At the Barents Sea flux gate (gate #2, Figure 3-17) SIVF values are comparably small, typically < 1 km³/day, and both import and export of sea ice into and out of the Arctic Ocean can be observed (Figure 3.3.4). Towards the end of the winter export is more likely: 11 of the 14 winters had maximum export rates in March or April. Winter 2002/03 is marked by an exceptionally large ice export of up to ~3 km³/day in March while winter 2003/04 is marked by an exceptionally large ice import of up to 2 km³ / day in March.

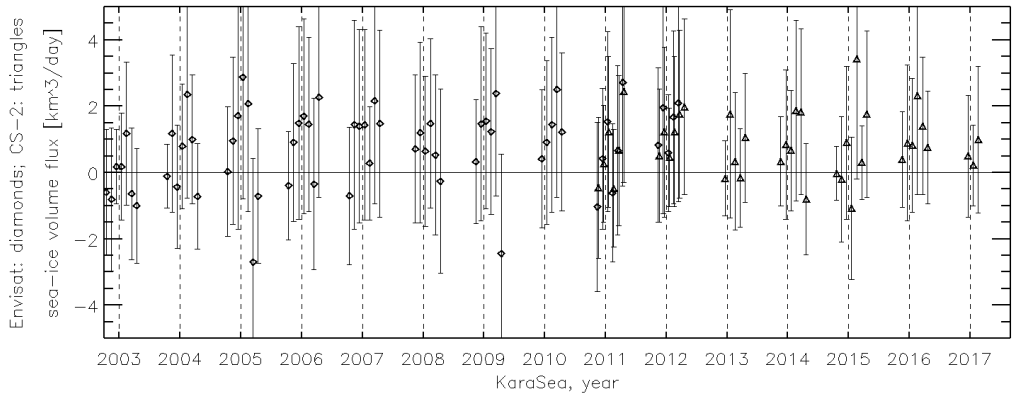

Figure 3-20: Sea-ice volume flux time-series for flux gate #3: Arctic Ocean ←→ Kara Sea (see Figure 3-17).

At the Kara Sea flux gate (gate #3, Figure 3-17) we find a predominant import of sea ice into the Arctic Ocean, i.e. the Kara Sea exports ice (Figure 3-20). Export rates out of the Kara Sea are about 1 km³/day. We find winters with a rather low variability from month to month like 2008/09, 2011/12 or 2015/16 but also winters where the SIVF direction changes drastically, for example, in 2004/05 from > 2km³/day export in February to > 2km³/day import in March or in 2008/09 from > 2km³/day export in March to > 2km³/day import in April. Such high import rates are rare though for the period investigated.

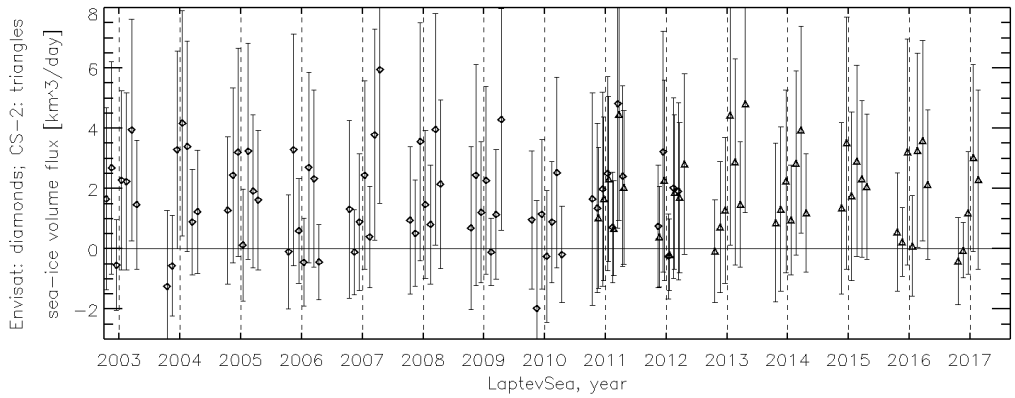

Figure 3-21: Sea-ice volume flux time-series for flux gate #4: Arctic Ocean ←→ Laptev Sea (see Figure 3-17).

The Laptev Sea exports sea ice into the Arctic Ocean through flux gate #4 (see Figure 3-17) during most winter months of our investigation period (Figure 3-21). Average export rates vary between 1 km³/day and 3km³/day and may peak 6km³/day (2006/07). We find 300 km³ to 400 km³ as an average amount of cumulative winter-time SIV export out of the Laptev Sea

into the Arctic Ocean. Figure 3-22 shows the zonal SIVF out of the Laptev Sea and illustrates that the meridional sea-ice export out of the Laptev Sea (Figure 3-21) is temporally more continuous and steady than the sea-ice exchange with the East-Siberian Sea through flux gate #10. Through this gate sea-ice import and export vary more. Only the winters 2008/09, 2011/12, and 2016/17 saw a larger cumulative ice export out of the Laptev Sea, peaking eventually at > 4km³/day also at this flux gate.

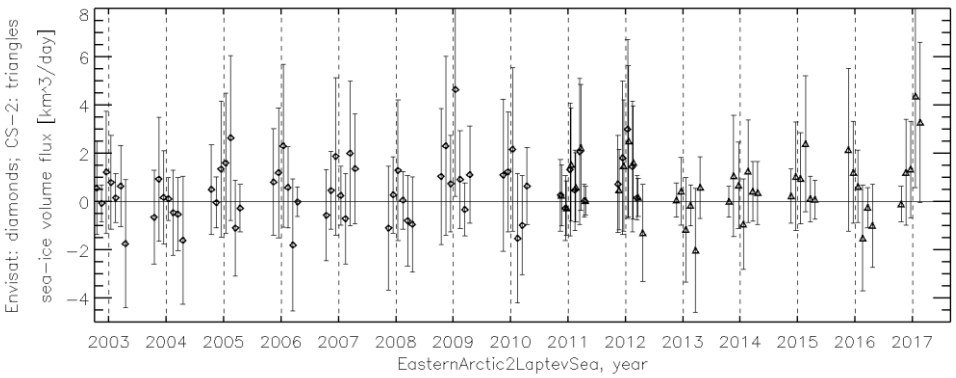

Figure 3-22: Sea-ice volume flux time-series for flux gate #10: East-Siberian Sea ←→ Laptev Sea (see Figure 3-17).

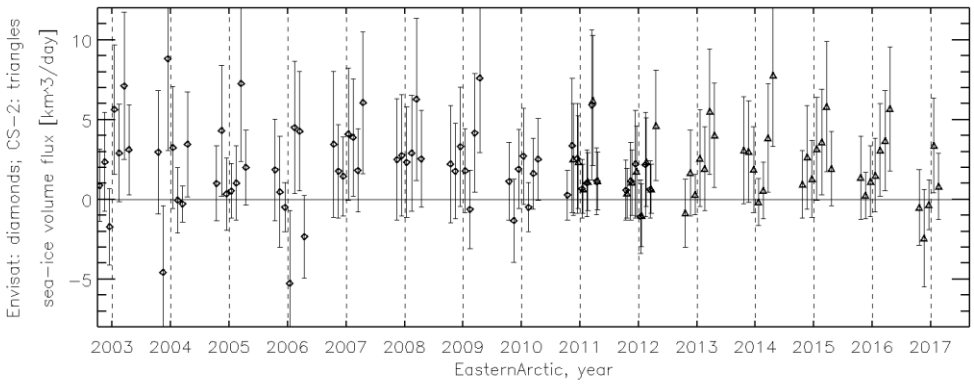

Figure 3-23: Sea-ice volume flux time-series for flux gate #5: Arctic Ocean ←→ East Siberian Sea / western part of transpolar drift (see Figure 3-17).

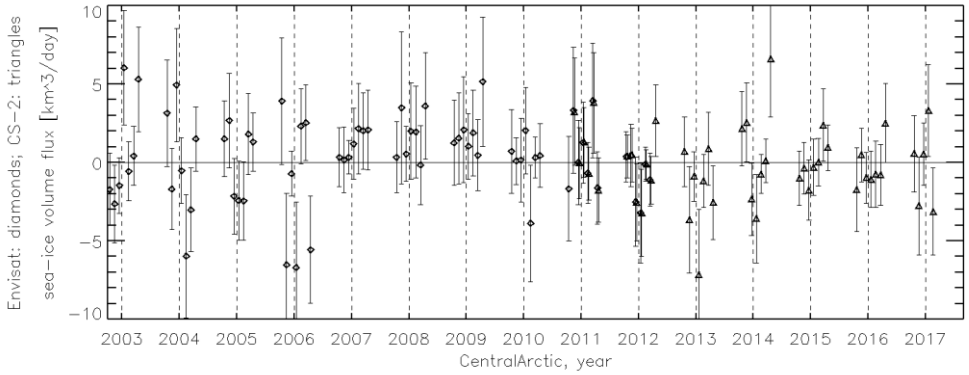

Figure 3-24: Sea-ice volume flux time-series for flux gate #6: Arctic Ocean ←→ Chukchi Sea / eastern part of transpolar drift (see Figure 3-17).

Now we compare the fluxes through gates #5 to #7. While gates #5 and #6 can be associated with the transpolar drift for which we would expect a northward SIVF, gate #7 is situated close to the Canadian Arctic Archipelago and hence the eastern limb of the Beaufort Gyre so that we expect a southward SIVF. Indeed, for gate #5 (Figure 3-23) we find mostly positive SIVF values, i.e. a northward flux; major exceptions only occur in 2003/04, 2005/06 and 2016/17. On average, sea ice is imported into the central Arctic Ocean at a rate of 2 km³/day at this gate; for 11 of the 14 winters we find at least one SIVF value above 5 km³/day. In most winters the month-to-month variation in SIVF is relatively low and the direction of the SIVF does not change sign. The SIVF through gate #6 (Figure 3-24) is more variable with month-to-month changes in SIVF sign and with month-to-month changes in SIVF of > 5km³/day (see 2003/04 and 2005/06). Winters with a particularly stable SIVF are 2007/08 through 2010/11 and 2014/15+2015/16; in these winters also the flux through the neighbouring gate #5 was relatively stable (compare Figure 3-23). We do not find a general im- or export of sea ice into or out of the Arctic Ocean at this gate #6. What seems to characterise this gate are episodes with low variation in SIFV (see above) and episodes with very variable SIVF where SIVF rates can range over a winter from -5 km³/day to +5 km³/day with peak values of > +6 km³/day and < -7 km³/day.

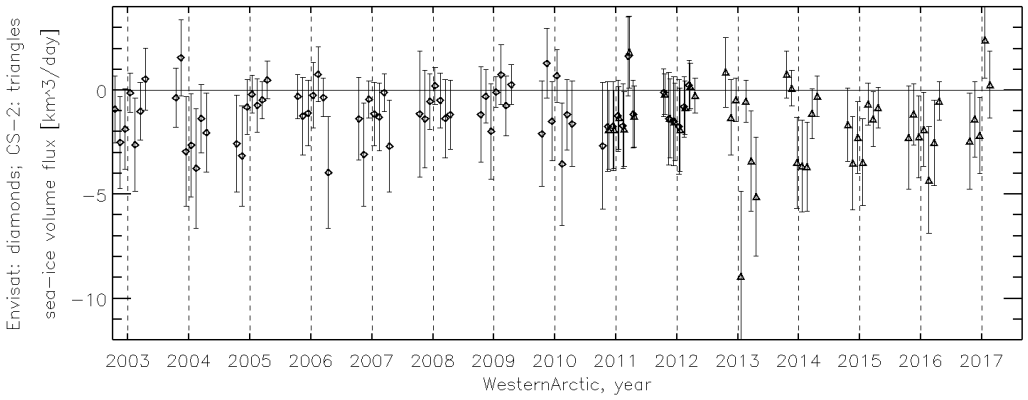

Figure 3-25: Sea-ice volume flux time-series for flux gate #7: Arctic Ocean ←→ Beaufort Sea (see Figure 3-17).

For gate #7 we find mostly negative SIVF rates (Figure 3-25), i.e. an ice export out of the Arctic Ocean. The average rate of this export is 2 km³/day and commonly varies between 0 and 4 km³/day, except in winter 2012/13 when we find two months with > 5 km³/day. The fact that SIVF rates at this gate #7 known for the presence of a lot of thick sea ice (see also Figure 3-17) are comparable to the fluxes observed and most of the other gates – except #1 – can be associated with the relative immobility of this ice during winter.

The re-distribution of sea ice between the Beaufort, Chukchi and East Siberian Seas through gates #8 and #9 (Figure 3-17) is illustrated by the zonal SIFV time series shown in Figure 3-26 and Figure 3-27. During most of the winters we find a negative zonal, i.e. westward, SIVF. SIVF rates are higher in the Beaufort Sea at gate #8: ~5 km³/day than across the Chukchi and East Siberian Sea at gate #9: ~2 km³/day. Gate #8 also shows a more constant westward SIVF while at gate #9 there are more months and episodes with an eastward SIVF. At gate #8 eastward SIVF peaks at 3 km3/day (2005/06, 2012/13) while westward SIVF exceeds 7 km³/day in 9 of the 14 winters and peaks 13 km³/day in winter 2012/13 and 15 km³/day in winter 2015/16. In contrast, at gate #9 we find an eastward SIVF

exceeding 3 km³/day in five winters while the westward SIVF exceeds 7 km³/day only in four winters. The month-to-month and inter-winter variability is similar for these two gates.

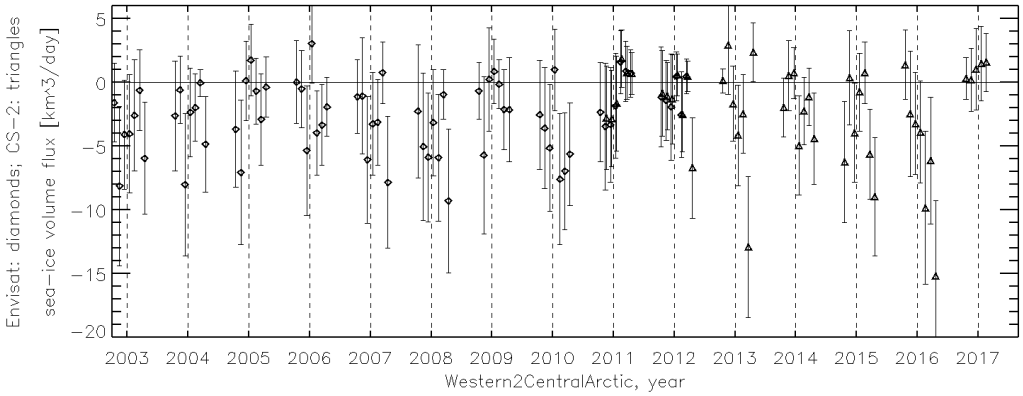

Figure 3-26: Sea-ice volume flux time-series for flux gate #8: across the Beaufort Sea (see Figure 3-17).

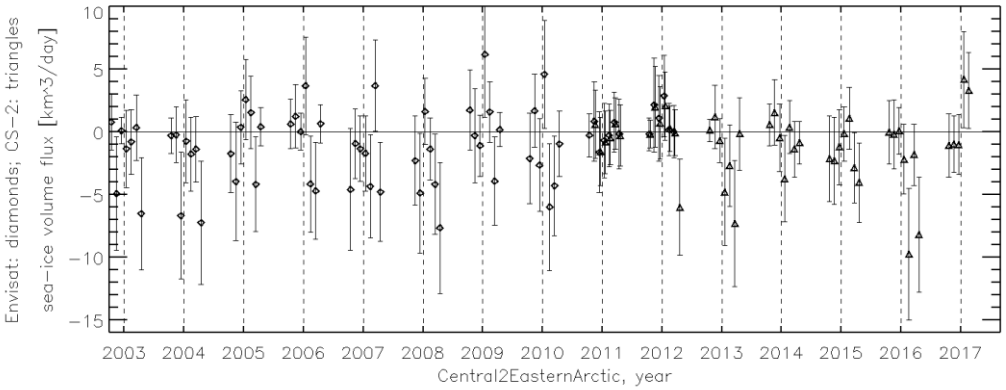

Figure 3-27: Sea-ice volume flux time-series for flux gate #9: Chukchi Sea ←→ East Siberian Sea (see Figure 3-17).

An inter-comparison of these fluxes with fluxes derived from other data sets is pending. Results from inter-comparisons between the ESA-SICCI2 sea-ice thickness CDR and sea-ice thickness data from ICESat and from CryoSat-2 are presented in the Product Validation and Intercomparison Report (PVIR) for SIT associated with the ESA SICCI2 project. These results would allow to investigate – by means of looking at the SIT difference maps – where the SIVF derived here would differ substantially from a SIVF derived with the other SIT data sets used in the PVIR.

We note that we consider the length of the time series as too short to make a statement about trends.

We note in addition that the fact that we used a snow depth climatology also torpeds any trend analysis because any trend found might simply be caused by an increasing or decreasing match between the snow depth climatology used and the actual snow depth distribution.

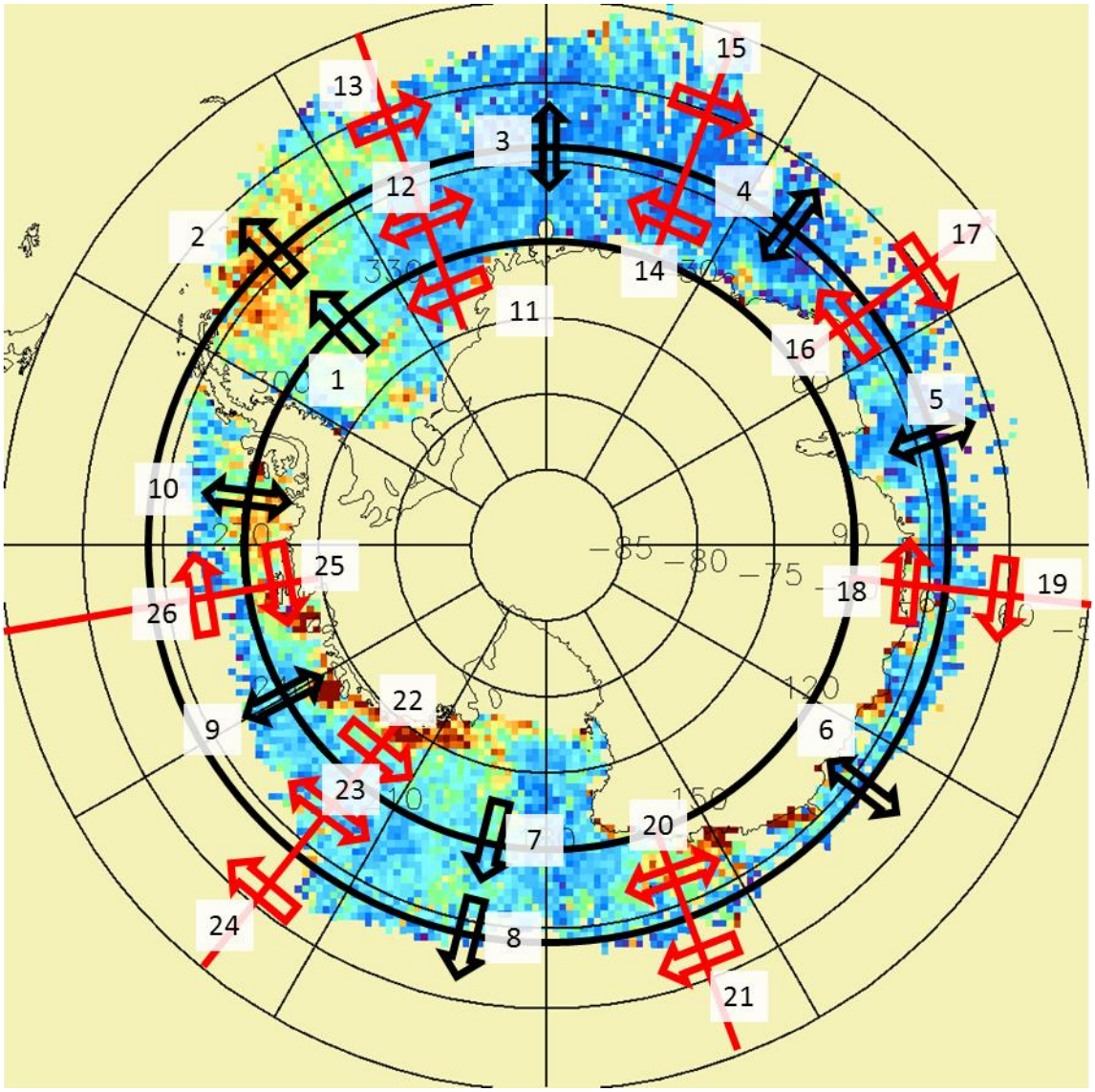

Figure 3-28: Locations of the flux gates in the Antarctic. We have 10 meridional (numbers 1 to 10) and 16 zonal (numbers 11 to 26) flux gates. Because of the total numbers we don't specify names here but will do that, if required, in the text. The background is a typical winter sea-ice thickness distribution.

In the following we reflect upon sea-ice volume flux (SIVF) estimates for the Southern Ocean. The gates across which we estimated SIVF are shown in Figure 3-28. Like in the Arctic we differentiate between meridional fluxes which are positive when northward and zonal fluxes which are positive when eastward. First we focus on the Western Weddell Sea, i.e. gates #1, #2, and #11 to #13.

The meridional SIVF through gates #1 and #2 is positive = northward and very large during winter and close to zero during summer (Figure 3-29 and Figure 3-30). It has a pronounced seasonal cycle. During winter SIVF rates at both gates regularly exceed 15 km³/day. Month-to-month changes can be > 15 km³ / day as well. Peak values in excess of 25 km³/day are observed twice at gate #1 (August 2006 and May 2016) but seven times at gate #2. The large differences between Envisat based (diamonds) and CS-2 based (triangles) SIVF values in the overlap year 2011 (Figure 3-30)

suggests, however, that the large number of these extraordinarily high SIVF values at gate #2 could also be caused by SIT over-estimation of, in this case, CS-2; this is supported by the observation that 5 of the winters with more than 25 km³/day SIVF occurred after 2011. The larges SIVF for the Envisat period at gate #2 occurs at the same month and year as at gate #1: August 2006. The degree of month-to-month SIVF variability increases particularly at gate #2 between Envisat (until 2011) and CS-2 (after 2011); this is less visible at gate #1.

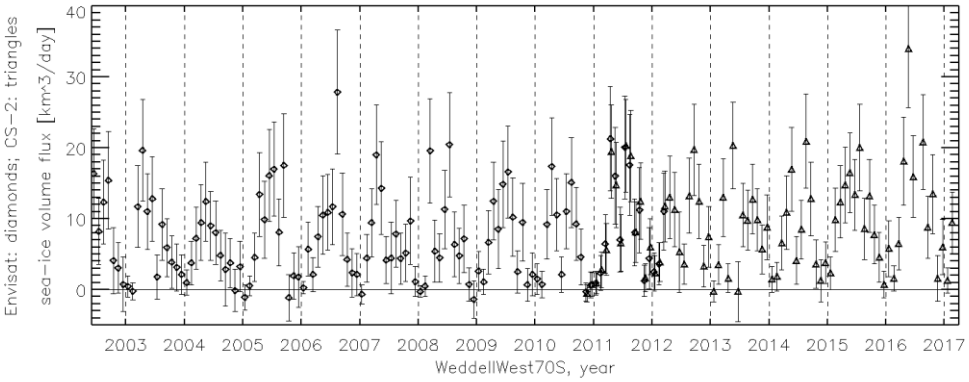

Figure 3-29: Antarctic sea-ice volume flux time series through gate #1 (see Figure 3-28): Western Weddell Sea through 70S.

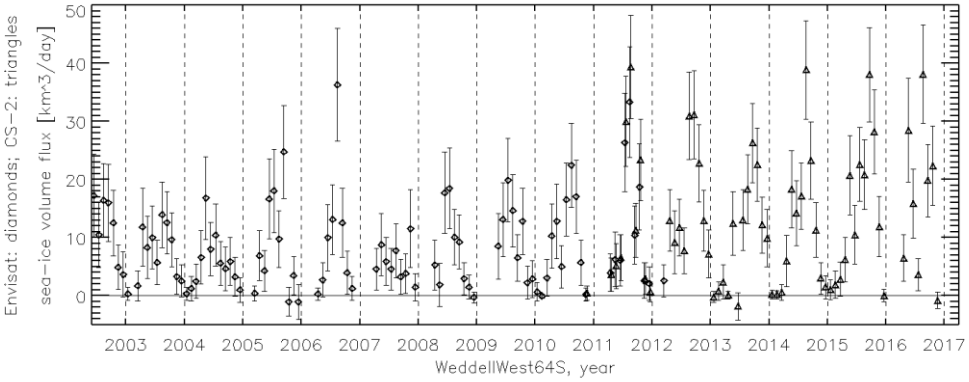

Figure 3-30: Antarctic sea-ice volume flux time series through gate #2 (see Figure 3-28): Western Weddell Sea through 64S.

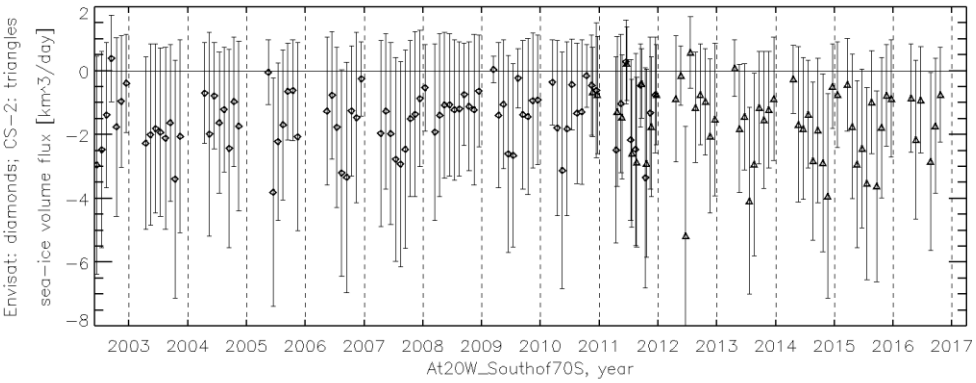

Figure 3-31: Antarctic sea-ice volume flux time series through gate #11 (see Figure 3-28): Central ←→ Western Weddell Sea south of 70S.

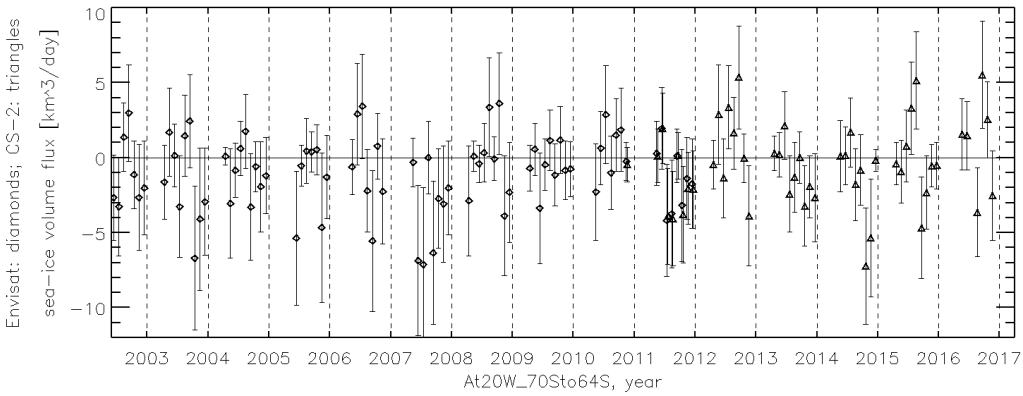

Figure 3-32: Antarctic sea-ice volume flux time series through gate #12 (see Figure 3-28): Central ←→ Western Weddell Sea between 70S and 64S.

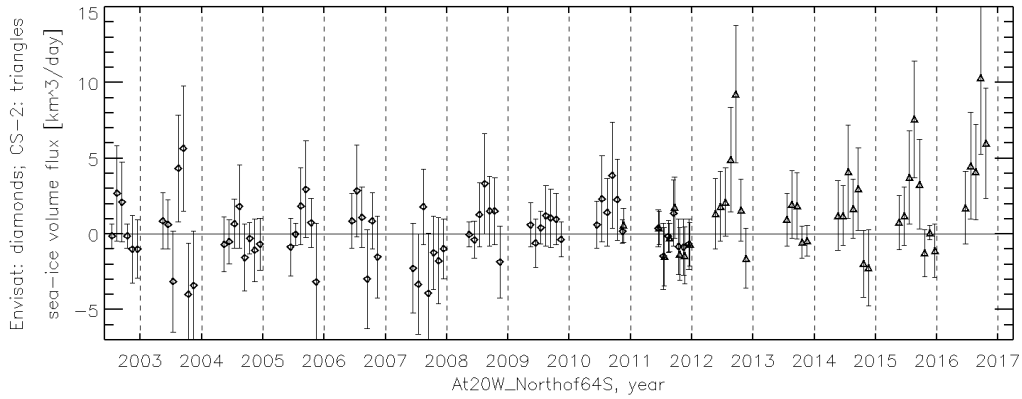

Figure 3-33: Antarctic sea-ice volume flux time series through gate #13 (see Figure 3-28): Central ←→ Western Weddell Sea north of 64S.

As with regard to the zonal SIVF fluxes at gates #11 through #13 we find that at the southernmost gate #11 sea ice is imported in the Western Weddell Sea at an average rate of 1.5 km³/day (Figure 3-31). This is in line with the overall circum-Antarctic sea-ice motion near the coast which is westward. Differences between Envisat and CS-2 SIT based SIVF estimates in the year of overlap 2011 can be comparably large: ~1 km³/day in April 2011, but are not consistent in their sign and therefore we do not find systematic changes between SIVF rates before and after the sensor switch.
This last statement also applies to the SIVF rates found for the middle gate #12 (Figure 3-32) and the northernmost gate #13 (Figure 3-33). Inter-annual variation in the SIVF is quite large at gate #12 between an overall annual average import into or export out of the Western Weddell Sea; the overall impression is that import is larger. Remarkable are two years: 2003 and 2016, when the SIVF sign switches from positive high (2 km³/day and 5 km³/day in September) to negative high (-7 km³/day and -5 km³/day in October) (Figure 3-32), i.e. from net export to net import. At gate #13 inter-annual variation is smaller than at gate #12 and the overall average sign of the SIVF is positive for 9 to 10 years – suggesting an eastward ice export out of the Western Weddell Sea which is in line with the general picture. Monthly SIVF rates regularly exceed 2 km³/day but rarely exceed 5 km³/day at gate #13 in comparison to gate #12.

Second we focus on the Ross Sea, i.e. gates #7, #8, and #20 to #24. In agreement with expectations we find a massive northward export of sea ice in the Ross Sea at gate #7 with winter-time value of the positive (northward) SIVF regularly exceeding 10 km³/day. We find a pronounced seasonal cycle – like in the Western Weddell Sea (compare with Figure 3-29 and Figure 3-30) – with SIVF around zero during summer. In contrast to gates #1 and #2, where we suggested an overestimation of CS-2 based SIVF relative to Envisat based SIVF, we find the opposite here; it seems as if winter-time SIVF are higher and more variable for the Envisat period before 2011 but on average smaller for the CS-2 period after 2011 (Figure 3-34). This is in line with the evaluation results presented in the PVIR for sea-ice thickness where we found considerably smaller sea-ice thickness values for CS-2 than for Envisat south of the gate #7; we considered this thinner sea ice as being more realistic due to the origin of the sea ice in this region: the Ross Ice Shelf polynya. Therefore, the SIVF values shown in Figure 3-34 before 2011 are most likely too large.

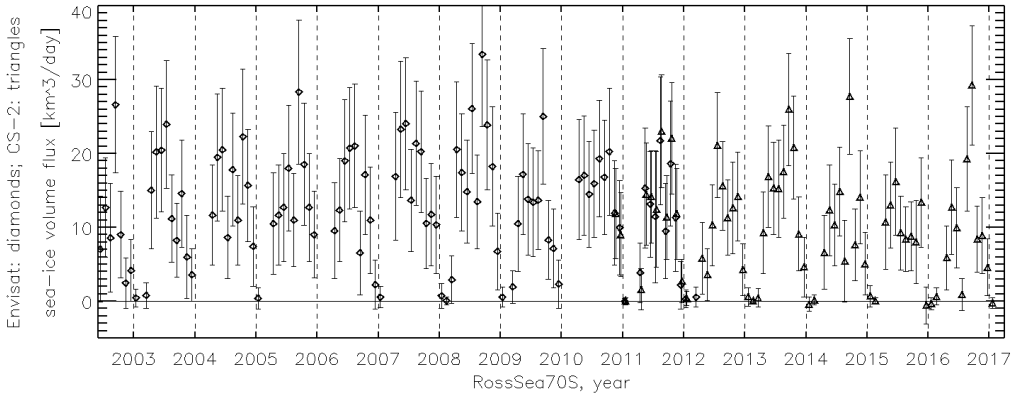

Figure 3-34: Antarctic sea-ice volume flux time series through gate #7 (see Figure 3-28): Ross Sea through 70S.

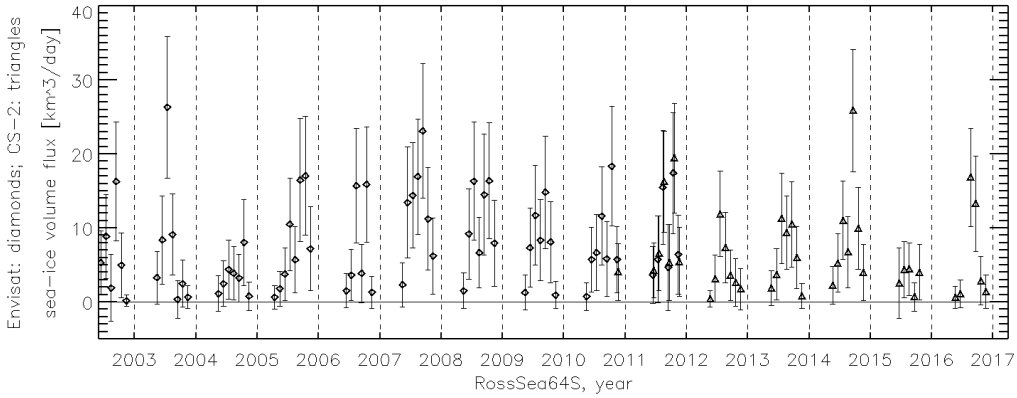

Figure 3-35: Antarctic sea-ice volume flux time series through gate #8 (see Figure 3-28): Ross Sea through 64S.

At gate #8, about 360 miles further north, we still find a clear seasonal cycle in SIVF and exclusively a northward sea-ice transport (Figure 3-35). While annual average SIVF values are smaller than at gate #7 we again find regularly SIVF values exceeding 15 km³/day – particularly during the Envisat part of the record. Years with a comparably SIVF at gate #7 (e.g. 2015) show a relatively low SIVF at gate #8 as well but not vice versa: 2004 was a year with particularly low SIVF at gate #8 while it was a year

with an average high SIVF: 15 km³/day at gate #7. On the other hand, the two years with the largest average SIVF at gate #8 (2007 and 2008, Figure 3-35) also saw an above normal average SIVF at gate #7 (Figure 3-34).

What about the zonal SIVF related to the Ross Sea? We find sea-ice import from and export into the East Antarctic (west of 160E) through gate #20 but also several months long episodes of almost no sea-ice exchange at this gate (Figure 3-36). The latter applies, e.g., for years 2006/07, 2007/08, 2009 and 2013. Episodes of positive SIVF, i.e. eastward SIVF and hence import from the East Antarctic occurred in 2005, 2010 and 2015 with peak SIVF values > 4 km³/day. Episodes of negative SIVF, i.e. westward SIVF through gate #20 and hence export into the East Antarctic occurred in 2003, 2011, 2013, and 2015 with peak values close to or well above 5 km³/day. North of 64S, at gate #21 (Figure 3-28) there are not too many valid SIVF data available (only few months) and hence results are not shown or discussed.

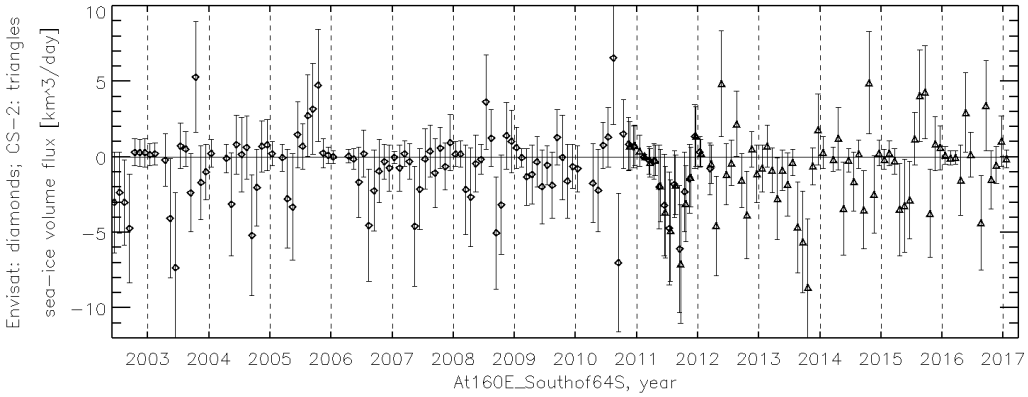

Figure 3-36: Antarctic sea-ice volume flux time series through gate #20 (see Figure 3-28): East Antarctic ←→ Ross Sea south of 64S.

At the eastern side of the Ross Sea, at 220E, gates #22 and #23 (too few data for gate #24 and therefore neither shown nor discussed), we also find episodes of sea-ice import into the Ross Sea, expressed via negative (westward) SIVF values and episodes of zonal sea-ice export out of the Ross Sea, expressed via positive (eastward) SIVF values.

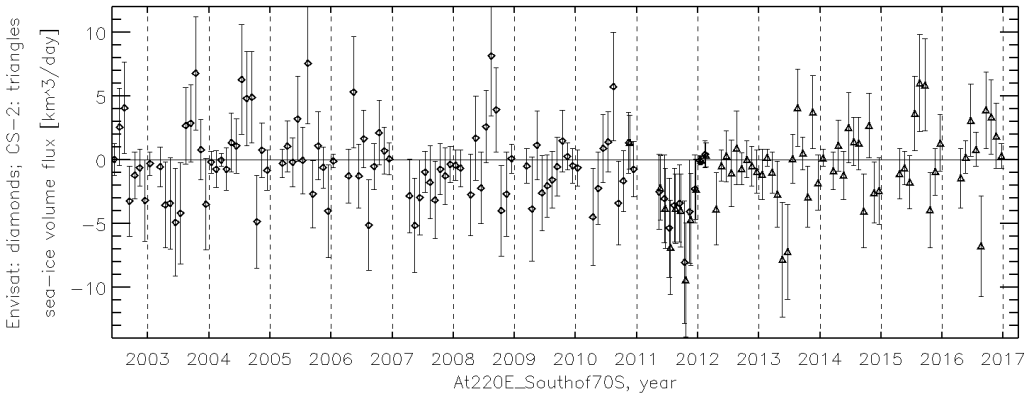

Figure 3-37: Antarctic sea-ice volume flux time series through gate #22 (see Figure 3-28): Amundsen ←→ Ross Sea south of 70S.

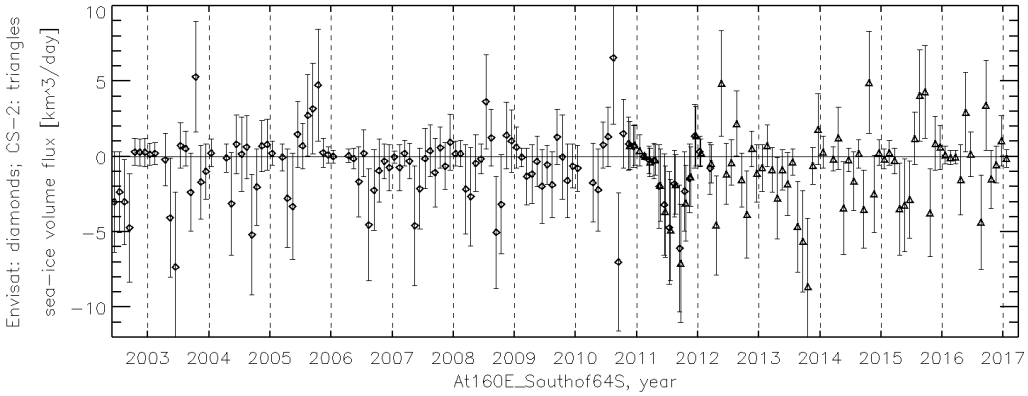

Figure 3-38: Antarctic sea-ice volume flux time series through gate #23 (see Figure 3-28): Amundsen ←→ Ross Sea between 70S and 64S.

Most interesting to note are the SIVF for years 2005, 2011, 2013, and 2015. In 2005, winter, we find positive SIVF at gate #23, i.e. between 64S and 70S, i.e. an export out of the Ross Sea (Figure 3-38). While there is some export further south as well (gate #22, Figure 3-37), the interesting thing is that there is sea-ice import from the East Antarctic in the same zonal band of about the same magnitude (Figure 3-36). The same behaviour we find for the other years mentioned. In 2011, in late 2013 and in 3 winter months in 2015 we find sea-ice import into the Ross Sea from the East through gate #23 (Figure 3-38); for the same years and periods we find sea-ice export out of the Ross Sea towards the West through gate #20 (Figure 3-36). Also, the 3 months of SIVF reversal in late 2015 from sea-ice import to sea-ice export at gate #23 (Figure 3-38) has its counterpart at gate #20 with a reversal from sea-ice export to sea-ice import (Figure 3-35). The SIVF at gate #22 (Figure 3-37) is mostly quite similar to that at gate #23.

With that we close our discussion of SIVF in the Antarctic because we think that we have been able to provide some first interesting insights. We note that the sea-ice thickness data set used for the SIVF computations is as short as the one for the Arctic and also uses a snow depth climatology which prevents us from carrying out any trend analysis for the reasons stated in the context of the Arctic SIVF. In addition to that, the sea-ice thickness product for the Antarctic needs to be considered as being experimental because on the one hand the evaluation is less mature than for the Arctic (see PVIR-SIT). On the other hand it is shown (also in the PVIR-SIT and in [RD-12]) that there seem to still exist inconsistencies in the obtained sea-ice thickness between Envisat and CS-2 and sea-ice thickness values might also be a bit too large in certain regions, e.g. in the Weddell Sea (see PVIR-SIT).
We note also, that the NSIDC sea-ice motion product used is certainly less accurate in the Antarctic than in the Arctic simply because less data have been used to generate it and because less data have been available to evaluate it.

4 Dynamical consistent assimilation of SICCI-2 SIC and SIT into a coupled ocean – sea ice model – status-quo

Assimilation of data into numerical ocean-sea ice models provide the opportunity to combine information from models and data to arrive at a consistent and complete description of the processes that drive changes in the ocean and of the sea ice. Ideally, the combined state has smaller errors than the individual products, the data and the model simulation. In practice, models are known to have large biases; these biases are partly corrected by assimilating data but often are regionally so strong that the combined product has only smaller errors than the pure unconstraint simulation but remain less good than the data fields. Assimilation therefore mostly serves the goal to fill gaps, to provide a complete picture and to improve models in this attempt. However, despite large errors of the models data, validation is nevertheless possible by assimilating data. By inter-comparison of a new satellite product with results from numerical modelling we can get an idea where models and data are consistent and likely to be trustworthy. This provides information about the quality of the data and the model. We report about results achieved by assimilating SICCI prototype products into numerical models within the SICCI project consortium in the framework of the coupled sea ice - ocean numerical model of the Arctic Ocean.

4.1 Assimilation of SICCI SIC prototype products into coupled ocean-sea ice model

Details of the model configuration and the assimilation procedure as well as the assimilated data have been presented in the previous Sea Ice Climate Change Initiative: Phase 1 in Climate Assessment Report D4.2. We summarize the configuration only briefly since the present results are based on the identical configuration.

4.1.1 Description of the model and method

The model domain covers the northern North Atlantic and the Arctic Ocean with the model grid being curvilinear and a subset of the 16-km resolution Atlantic-Arctic model (ATL06) reported in [RD-15]. As atmospheric forcing the model uses the atmospheric state from the 6-hourly NCEP R1 reanalysis. At the open southern boundary, roughly at 48° N in the Atlantic, results from a 60-year long integration of the ATL06 model are used. The sea ice component is based on a Hibler-type ([RD-16], [RD-17]) viscous-plastic dynamic-thermodynamic sea ice model. The thermodynamic part of the model is the so-called zero-layer formulation following [RD-18] with snow cover as in [RD-19]. The temperature profile in the ice is assumed to be linear, with constant ice conductivity. Such a formulation implies that the sea ice does not store heat, and, as a result, the seasonal variability of sea ice is exaggerated [RD-20].

4.1.2. Adjoint data assimilation approach

Similar to the work of [RD-21], our assimilation also employs the ECCO adjoint methodology to bring the coupled sea ice-ocean general circulation model into consistency with assimilated data and prior uncertainties. In the adjoint method, an uncertainty-weighted sum of squares of model-data misfits is minimized in an iterative fashion by using its gradient with respect

to a number of control variables. Although the sea ice module was active in the adjoint integration, the sea ice dynamics were switched off. A complete list of parameters assimilated and their sources are presented in Table 4-1.

Table 4-1: Datasets used in the assimilation procedure.

Dataset	**Source**
Monthly PHC climatology	PHC 3.0, *Steele et al.* [RD-22]
Mean Dynamic Topography	MDT from Technical University of Denmark *Cheng et al.* [RD-23]
Monthly SST	Remote Sensing Systems [RD-24]
Sea Level Anomalies	TOPEX/Poseidon, ERS-1,2 and Envisat, AVISO [RD-25]
EN3 hydrographic data	*Ingleby and Huddleston* [RD-26]
NISE hydrographic data	*Nilsen* [RD-27]
Sea ice concentration	EUMETSAT OSI-SAF Version 2 (constant uncertainties) ESA CCI Sea-Ice-ECV project (variable uncertainties) [RD-06].

Each of the iterative cost function reductions is performed until the cost function differs by less than 1% in two consecutive iterations. After the first year assimilation, we move to the next year using the final state of the previous year successful iteration as initial conditions. Therefore, the iteration termed 0 in the following makes already use of an improved initial condition from the assimilation in the previous year, and is thus not equivalent to a free run starting from climatology. For the impact on the ocean circulation, we consider also the free run to demonstrate the impact of changing the initial conditions by assimilating data during the preceding year.

The seasonal cycle of sea ice area (SIA) and sea ice extent (SIE) are shown in Figure 4-1 again for years 2005 and 2007. Results for SIA for both years show that values of SIA in general are getting closer to satellite observations as a result of the SIC assimilation. One would expect that, close to the beginning of the assimilation period (1st of January), corrections of the atmospheric forcing did not have enough time to considerably influence sea ice parameters. This is true for SIA in 2007, when sizable differences between initial and last iterations only first appear in May. However, SIA in 2005 gets considerably closer to observations already in February, indicating that atmospheric corrections actually can affect sea ice parameters relatively fast even during winter.

For both years SIA shows overall improvement during the whole year; but this is not the case for the SIE. In 2005 the SIE good match between initial iteration and satellite data during summer months disappears after assimilation, with considerable underestimation of SIE. In 2007 there is an overall SIE improvement after the assimilation, but there are again months with a considerable SIE underestimation. Both metrics suffer from the inability to guarantee that improvements in this metric also lead to an overall improved match, since a perfect area evolution may still correspond to considerable differences to the data in their regional distribution.

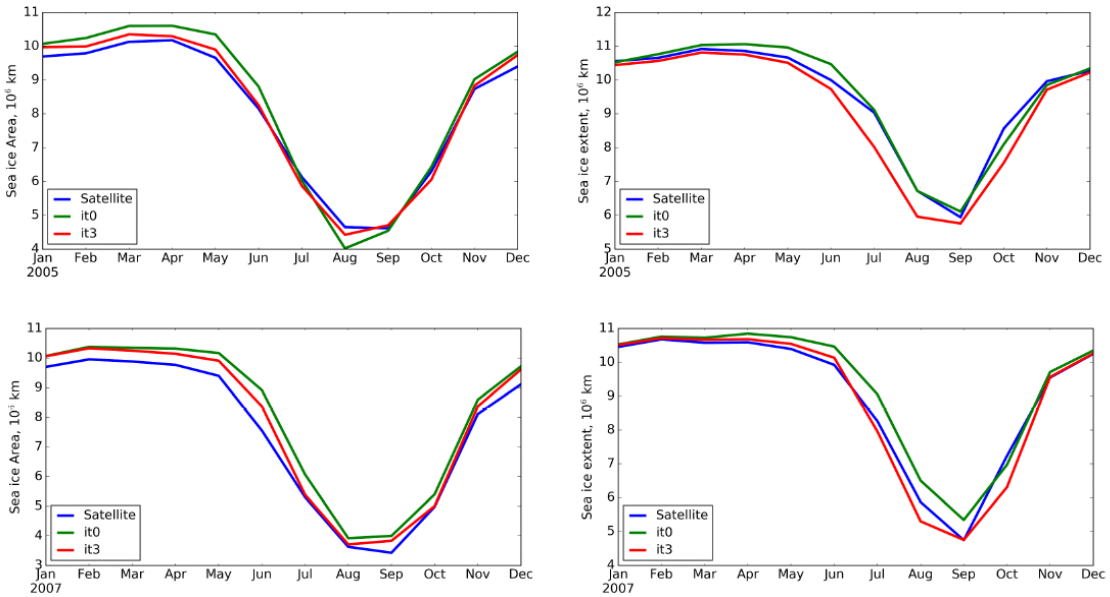

Figure 4-1: Monthly mean sea ice area (left) and extent (right) for years 2005 (top) and 2007 (bottom). Assimilated satellite data is shown in blue, model solution without corrections is shown in green and the result from the last iteration is shown in red.

Therefore, those commonly used integral parameters show limited ability to characterize the quality of sea ice simulations. Chances of having SIE distribution close to observations with quite different spatial shape of the sea ice field are very high. This calls for changing the common practice of model evaluation by only comparing their ability to simulate present day SIE without considering the sea ice spatial distribution. To address this issue, [RD-28] have investigated several norms to measure the differences between two sea ice fields. They found that Hausdorff Distances have the best skill to quantifying the similarity between two-dimensional fields.

Two simpler better metrics regarding the model performance are the sum of the RMS errors for SIA and SIE, which at least to some extent consider differences in spatial distribution by penalizing positive and negative differences at every grid point. Monthly values of the SIA RMS error before assimilation, after assimilation and the respective differences between the two (in percent) are shown in Figure 4-2. Before assimilation, largest RMSE appear during summer months (> $2x10^6$ km^2), while in other seasons they are about $1.5x10^6$ km^2. Interesting to note, values of RMSE in March and September are quite similar, despite the large differences in ice cover in the two months.

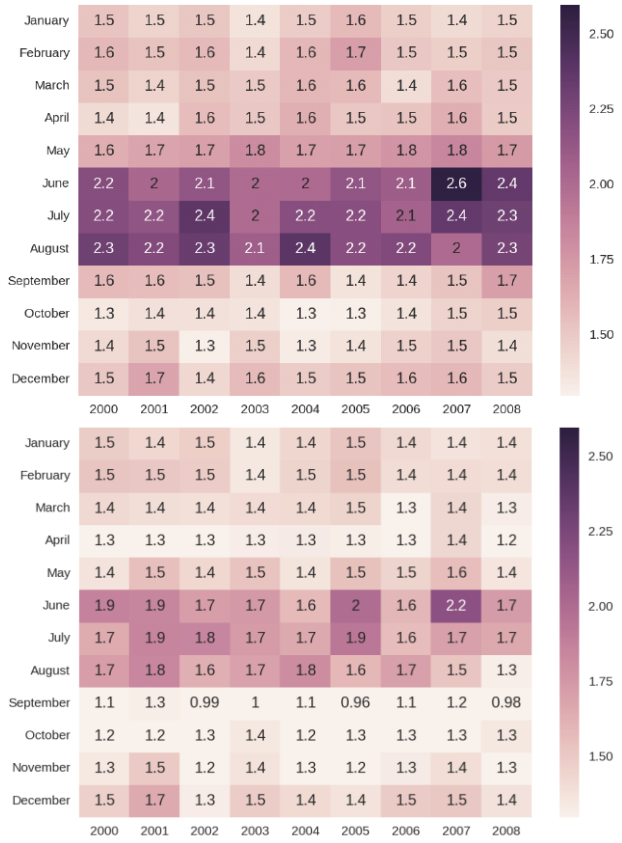

Figure 4-2: Sum of the sea ice area root-mean-square error (RMSE) (compared to assimilated sea ice at every grid location) for every month (in 10^6 km²), before assimilation (top), after assimilation (middle) Positive differences

After the assimilation the most notable improvements also occur for summer months, but with the addition of September. After the assimilation, March values show only about 10% improvement, while September values have about 25% improvement on average. There is no clear indication that assimilation of SIC on the yearly basis gradually improves the simulated sea ice, due to, for instance, better initial conditions in January. For some months the decrease in SIA RMSE after assimilation can be as little as 1%, although it is always getting smaller. The same is not the case for the case of SIE RMSE.

As expected, SIE RMSE values (Figure 4-3) are larger, with a maximum in summer and September before the data assimilation. Assimilation is most effective for a reduction of SIE RMSE in September (about 25% on average). After the assimilation October becomes, in addition to summer months, one of the months with relatively large SIE RMSE differences. October is also a month when (during 5 out of total 9 years) after assimilation the SIE RMSE increased. The SIE RMSE, similarly to the SIA RMSE, do not show any obvious tendency from the first year to the last.

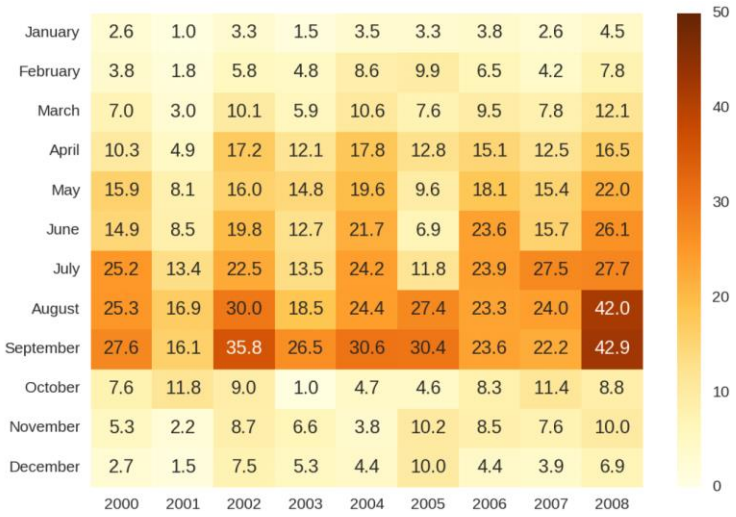

Figure 4-3: The percent difference between the RMSE before assimilation and after assimilation shown in Figure 4-2.

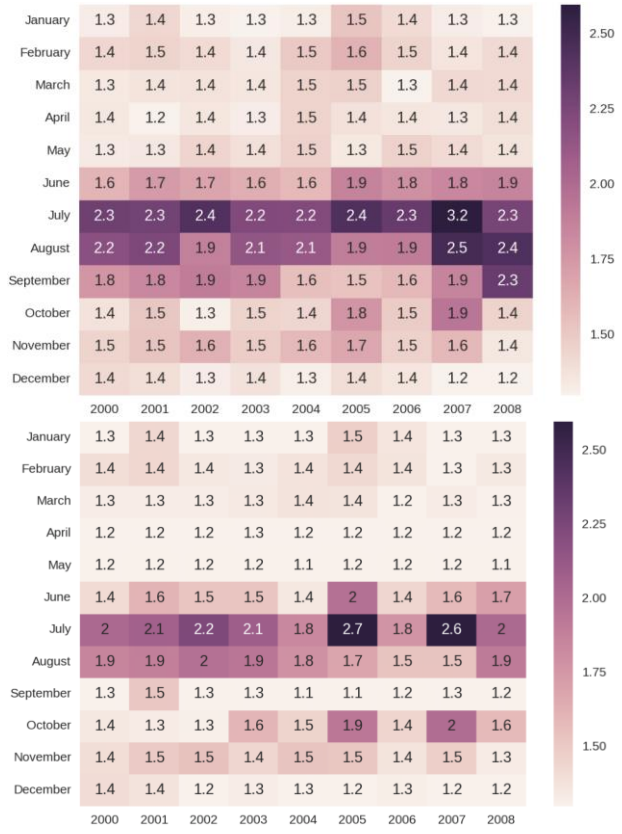

Figure 4-4: Same as Figure 4-2, but for the sea ice extent.

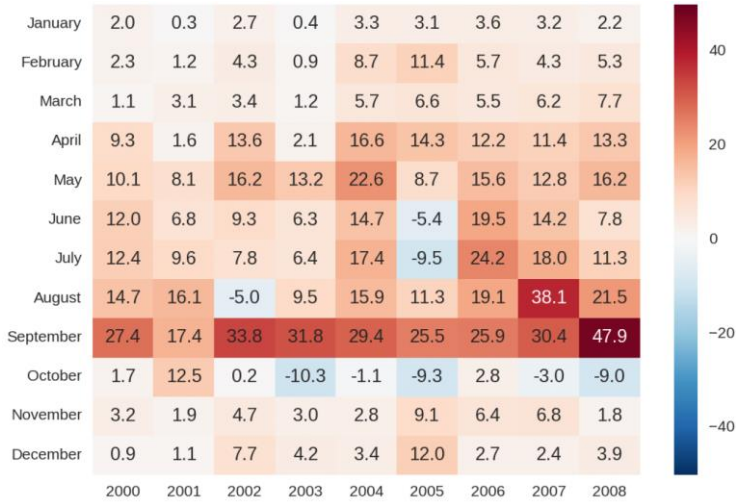

Figure 4-5: Same as Figure 4-3, but for the sea ice extent.

4.1.3. Ocean changes

Local changes of the SIC are caused by corrected atmospheric conditions (see above), which in the coupled system will also affect near-surface ocean parameters. Figure 4-6 shows differences in temperature and salinity between the initial and final iterations of the assimilation system for June and September of year 2005. The month of June is chosen because corrections to thermodynamic control variables during this month are largest. The sea surface temperature differences are mostly positive along the ice edge, where the model produces too much ice in the initial iteration and lower in magnitude in the central part of the Arctic Ocean. In June, considerable temperature differences cover a much smaller area, since most of the shelf seas are still covered by high concentrations of sea ice and most of the additional energy resulting from the correction to thermodynamic control variables is spent directly in the sea ice melting.

The surface salinity (Figure 4-6, right column) shows an increase in the Eurasian Basin, caused by additional sea ice production (or less melting). There is a decrease of salinity around the sea ice edge due to melting of excessive sea ice formed in the initial iteration. In September, however, there is a pronounced increase in salinity in most of the Arctic shelf seas. This might be a result of the local increase in sea ice production in areas which become free of ice due to the summer corrections (e.g. Laptev Sea), but still have quite negative temperatures in the original forcing which are not corrected in September (corrections in September are quite small) at the onset of the freezing period.

Due to the relatively short assimilation periods (1 year) and to the extremely low amount of vertical temperature/salinity profile observations, improvements in the vertical distribution of temperature and salinity after 9 years of assimilation are quite small. Nevertheless, the positive bias in the Atlantic Water layer temperature of the Eurasian Basin, which is characteristic for the forward run, has been slightly reduced (not shown). On the other hand, changes in the upper part of the water column due to sea ice corrections, although hardly penetrating deeper than the first 50 meters, may influence integral fluxes at the borders of the Arctic Ocean.

Figure 4-7 shows volume, heat, and freshwater fluxes through the main passages of the Arctic Ocean (except for Bering Strait, where fluxes are largely prescribed in the model by the boundary conditions). Along with the initial and final iterations, results for a no-assimilation forward run are shown in order to remove the effect of changing the initial conditions at the beginning of each assimilation year. These may lead to changes of long-term variability and may affect the fluxes towards the end of the assimilation period.

Differences in the volume flux are quite small for all passages. This is probably due to the fact, that the volume flux is mostly controlled by the wind stress, which means that the corrections of the control variables discussed above do not contribute considerably to changes in the ocean circulation. However, episodically significant changes can be observed, for example in summer 2008, when changes in the through flows at Fram Strait, Barents Sea Opening and St. Anna Trough are noticed, which are about 60% larger than in the forward simulation.

Differences in the heat flux (Figure 4-7, middle) at Fram and Davis Straits can be episodically relatively large, but they do not show any particular tendency and may be related to the local heating or cooling in the vicinity of the sections.

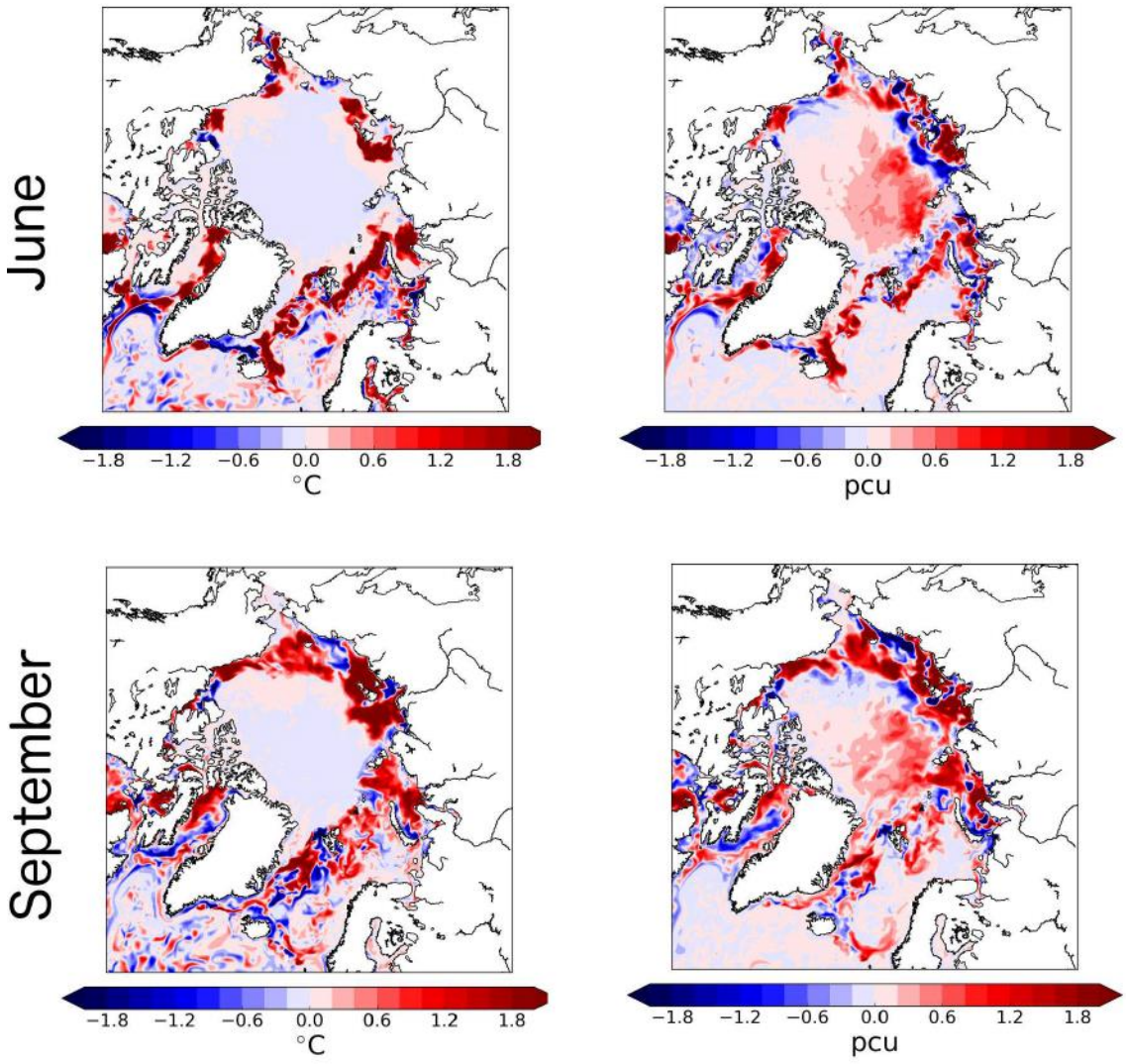

Figure 4-6: Differences in ocean surface temperature (left column) and salinity (right column) between first guess and last iteration for June 2005 (top row) and September 2005 (bottom row).

The freshwater flux differences (Figure 4-7, bottom) are most visible in the Fram Strait time series, but positive and negative differences remain comparable to the forward run and compensate each other, such that on average the relative difference is only about 3%. Large relative differences are again visible for the St. Anna Trough, which is located in an area with strong atmospheric corrections during most of the years.

From the combined analysis of Figure 4-7 one can conclude that, while on average most of the transports are hardly affected by the assimilation, during some periods relative large differences between the simulations with assimilation and the forward run without assimilation can be seen and may reach 60-100% for major straits.

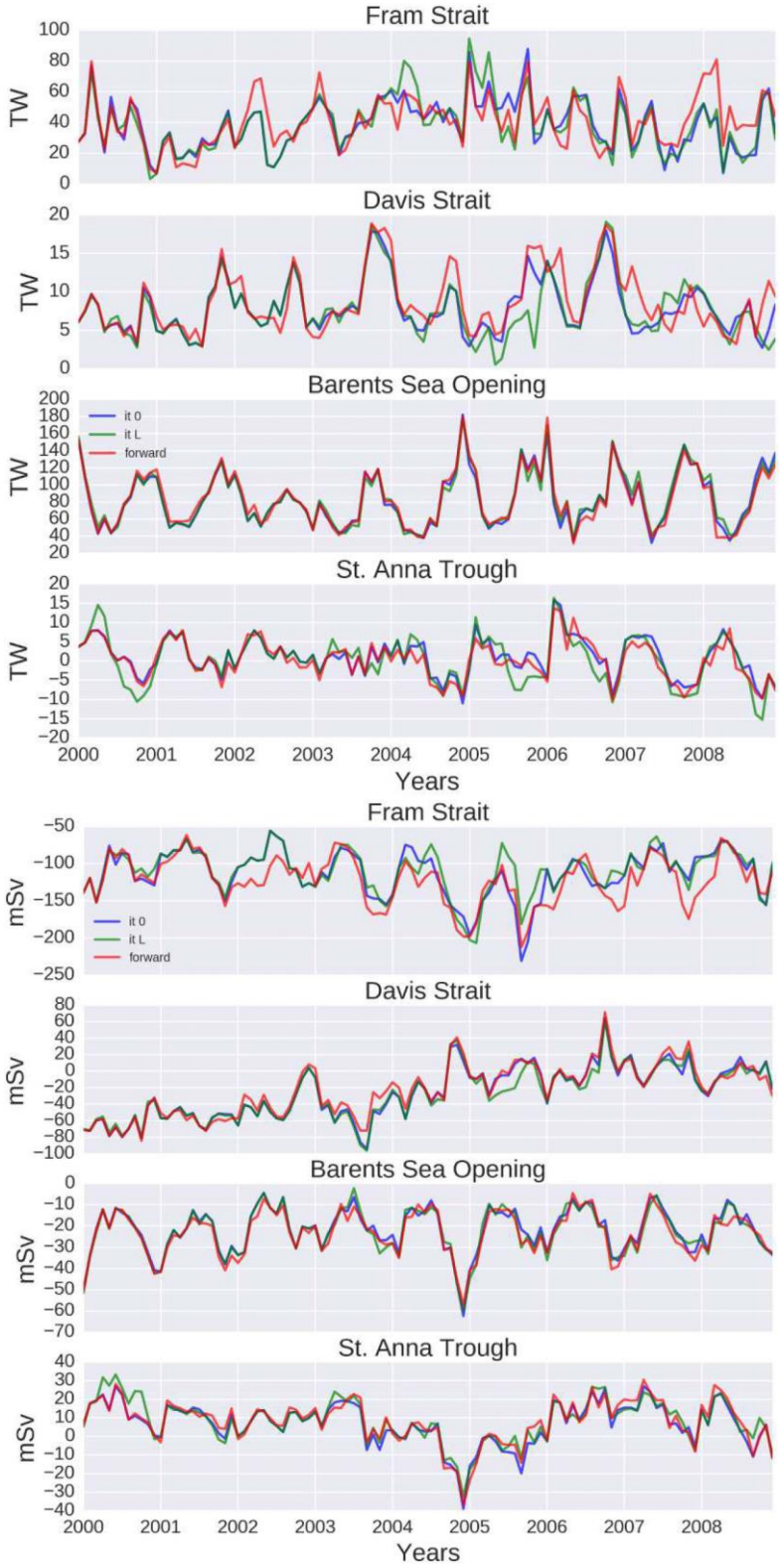

Figure 4-7: Fluxes through selected straits of (left) heat and (right) freshwater. For Fram Strait, Davis Strait and Barents Sea Opening, positive fluxes are into the Arctic Ocean; for St. Anna Trough, negative fluxes are into the Arctic Ocean. Results are shown for the forward run (red), for the run before assimilation (blue) and for the run after assimilation (green).

4.1.4 Summary

Results from a multi-year data assimilation attempt based on a coupled Arctic Ocean-sea ice system were presented. The largest improvements relative to simulations without data assimilation were seen for the sea ice concentration and sea surface temperature. Most of the improvements in the SIC happened during summer months and manifest themselves in a more realistic position of the sea ice edge and in SIC values closer to observations in the central Arctic.

The seasonal cycle of the monthly mean sea ice area (SIA) shows an overall improvement after assimilation, while sea ice extent (SIE) becomes worse during some months. The later fact demonstrates that the total mean SIE and SIA are not good measures for the model success in simulating sea ice, particularly considering the obvious improvements in spatial sea ice distribution. In order to obtain more meaningful estimates of the sea ice improvements, we consider sums of the RMS error for SIA and SIE. The largest reduction of the RMSE happened during the summer months.

The comparison to available but limited sea ice thickness observations shows that SIC assimilation reveals some improvements in SIT, despite these observations not being directly assimilated. The amount of assimilated ocean observations in the water column of the Arctic Ocean is almost negligible compared to the amount of SIC data. However, the ocean state is affected indirectly by SIC assimilation, for example due to the freshwater fluxes related to the additional melting or freezing and by changes in the ocean exposure to the atmosphere caused by changes in SIC. The transports of ocean properties do not change on average after the assimilation, but episodically they can be quite different from the corresponding transports in simulations without assimilation. The latter can still be important for local process studies or model validation against observations that are limited in time.

5 Dynamical consistent assimilation of SICCI-2 SIC and SIT into a coupled ocean – sea ice model – Update

Abstract

Based on the adjoint methodology, satellite sea ice data of concentration (SIC) and thickness (SIT) are assimilated into a regional Arctic coupled ocean-sea ice model for the period of 2000-2015 (SIT: 2003-2008), as well as other climate variables. The spatial distributions of sea ice become closer to the observations after assimilation, in particular for the position of ice edge. There is large improvement for the representation of SIC in the central Arctic in summer.

5.1 Introduction

As an important component of the climate system, sea ice strongly affects the climate of the Arctic through the transportation of heat and mass fluxes between the ocean and the atmosphere. During the last three decades, dramatic reduction of sea ice in the Arctic, especially the summer ice, has been observed ([RD-29], [RD-30], [RD-31]) mainly due to anthropogenic GHG emissions [RD-32]. This will affect the local environment, ecosystem and fishery [RD-33] and feedback on the climate system globally and in an amplified way in the Arctic [RD-34]. Skillful prediction of the seasonal and inter-annual variability of the Arctic sea ice is in great need to quantify the heat and mass budget locally and globally, and understand the processes driving the changes of the sea ice. Despite being a central focus of recent climate change studies, the Arctic remains one of the least explored regions. Due to the harsh environmental conditions of the Arctic, systematic and long-term observations of the ocean variables in the Arctic heavily rely on the satellites. Nevertheless, satellite observations have strong limitations over sea-ice-covered regions in the polar regions, considering the high surface albedo and parameters of the satellite orbits. A practical solution to derive realistic representations of the sea ice is to combine the satellite observations and numerical model simulations by means of data assimilation. This produces consistent data sets that optimize the limited observational data within the framework of the dynamical model, and can be later on used to monitor the Earth System, initialize forecasts and provide feedback on observation and model qualifications.

Similar to the matured ocean data assimilation in the ice-free region [RD-35], the way that sea-ice variables are assimilated into the sea ice model includes nudging (e.g., [RD-36], [RD-37]), ensemble Kalman filter (e.g., [RD-38, [RD-39]), three-dimensional (3DVAR; e.g. [RD-40], [RD-41]) and four-dimensional (4DVAR; e.g. [RD-21], [RD-42], [RD-43]) variational data assimilation methods. A first attempt of sea-ice data assimilation by [RD-38] employed the ensemble Kalman filter approach. The covariance between modeled sea-ice concentration (SIC) and ocean variables of temperature and salinity was described by ensemble statistics. A recent study by [RD-41] showed improvement in the reconstruction of the SIC field in both hemispheres by incorporating SIC data using a 3DVAR method. However, a sequential data assimilation method such as Kalman filtering or nudging scheme introduces unphysical energy and mass discontinuities and results in dynamical inconsistency in the ocean state estimation (e.g. [RD-44], [RD-36]; [RD-45]). Different from that, the adjoint method provides a natural

framework by using the physics and thermodynamics encoded in the model. Therefore, adjoint state estimations are energy and mass conserved and can be used in closed-budget climate studies (e.g. [RD-46], [RD-47], [RD-48], [RD-49]). The adjoint method was also used in sea-ice sensitivity studies (e.g. [RD-50], [RD-42]) to explore the relative contribution of atmospheric forcing and initial conditions to SIC.

Recent studies based on the adjoint method showed fruitful results. Based on a global, eddy-permitting ocean circulation model, [RD-21] studied the impact of assimilating SIC into the model and reconstructed the sea-ice fields of 2004. The authors found out that the synthesis of sea-ice data reduce model misfits in the Arctic and the synthesis of sea-ice thickness (SIT) may increase the accuracy of global SIT. A recent study by [RD-43] assimilated SIC and several ocean variables under the adjoint framework of a coupled Arctic coupled ocean-sea ice models and demonstrated substantial improvement in the representation of the SIC spatial distribution. Such improvement was also achieved for the position of the ice edge and SIC in the central Arctic.

In this study, we extend the work of [RD-43] and incorporate both SIC and SIT data into a regional coupled Arctic ocean-sea ice model for the period of 2000-2015. The goal of the study is to investigate the changes in the Arctic and explore the impact of synthesis of sea-ice data on the estimate of the ocean circulation. Reconstructions of sea-ice state will also be used to explore the impact from assimilation of SIT.

5.2 Model and method

5.2.1 Model

A regional configuration of the Massachusetts Institute of Technology general circulation model (MITgcm, [RD-51]) that covers the northern North Atlantic and the Arctic Ocean is used in this study. The grid of the coupled ocean-sea ice model is curvilinear and is a subset of the ATL06 [RD-15]. It has a spatial resolution of around 18-km and 50 vertical layers that vary from 10m in the top layers of the water volume to 550m in the deep parts of the ocean. The ETOPO2 database [RD-52] is used to build the bathymetry without artificial deepening or widening of the Nordic Seas' passages.

Atmospheric fields of 2m air temperature, precipitation rate, 2m specific humidity, downward shortwave radiation flux, net shortwave radiation flux, downward longwave radiation flux, 10m zonal and meridional wind components from the 6-hourly NCEP R1 Reanalysis [RD-53] are used as atmospheric forcing. The surface fluxes of heat, freshwater and momentum are derived via bulk formulae. Results from a 70-year integration of the ATL06 model at around 48N in the Atlantic are used as the open southern boundary. A barotropic net inflow of 0.9 Sv into the Arctic at the northern boundary is prescribed at the Bering Strait, balancing the corresponding outflow through the southern boundary. An annual averaged river runoff [RD-54] is applied in the North Atlantic, while seasonally varying runoff is used for the Arctic rivers.

The MITgcm offers a wide variety of modules that can simulate different aspects of the unresolved ocean physics. Similar to [RD-43], the model uses the K-profile parameterization (KPP) scheme of [RD-55] to parameterize the vertical mixing. The viscous–plastic rheology scheme of [RD-16] with an extended line successive over-relaxation (LSOR) method [RD-56] is applied

in the model. The sea ice model that is based on the Hibler-type ([RD-16], [RD-17]) viscous–plastic dynamic–thermodynamic sea ice model employs a thermodynamic following zero-layer formulation by [RD-18] with snow cover as in [RD-19]. More details about the model parameters used in this study can be found in [RD-43].

5.2.2 Adjoint

Similar to the work of [RD-21] and [RD-43], the ECCO adjoint method is used to derive the optimized estimation state that is consistent with the model and prior uncertainties in an iterative way. This GECCO2 synthesis [RD-57] based implementation was extended to facilitate the additional assimilation of sea ice parameters. A complete list of parameters assimilated and their sources is presented in Table 5-1. Different from [RD-43], sea ice data of SIT is also assimilated to the coupled ocean-sea ice model. This present pilot study is supposed to improve the reconstruction of sea ice and ocean states through the inclusion of both SIT and SIC, which are provided by the ESA Climate Change Initiative project (ESA CCI) phase 2. ESA-CCI SIT data were provided too late to include results in this report; instead we used SIT information from ICESat laser altimetry [RD-58].

Table 5-1: Data sets used in the assimilation procedure

Data set	Source
Mean dynamic topography	MDT from Technical University of Denmark
Monthly SST from AMSR-E/AMSR2	Remote Sensing Systems (www.remss.com)
Sea level anomalies	Topex/Poseidon, ERS-1,2 and Envisat, Copernicus Marine and Environment Monitoring Service
EN4 hydrographic data	EN4: 2000-2015
Sea ice concentration	OSI-SAF (2015; 2000-2002), ESA CCI v2.0 (2017; 2003-2015)
Sea ice thickness	JPL, ICESat laser altimetry [RD-58]

Under the framework of the adjoint method, a cost function J (equation 1) that is defined as an uncertainty-weighted sum of squares of model-data misfits (first term of J on the RHS) is minimized iteratively, using its gradient with respect to a number of control variables (the remaining terms of J on the RHS).

$$J = \sum_{t=1}^{t_f}[y(t) - E(t)x(t)]^T R(t)^{-1}[y(t) - E(t)x(t)] + v^T P(0)^{-1} v + u_m^T Q_m^{-1} u_m + \sum_{t=0}^{t_f-1} u_a(t)^T Q_a(t)^{-1} u_a(t) \quad (1)$$

For the model-data misfits penalty, $y(t)$ denotes the vector of assimilated data at time, $x(t)$ is the model state vector, and $E(t)$ is a matrix mapping the model state to the assimilation space. In the remaining components, v is the difference between the first-guess initial condition and the model state, and u_m ($u_a(t)$) is the difference between the first-guess time mean (time-varying) atmospheric state and the optimized mean (time-varying) atmospheric state. The relative contribution of each term to the cost function is defined by four weights matrices: $R(t)^{-1}$, $P(0)^{-1}$, Q_m^{-1} and $Q_a(t)^{-1}$. A more detailed description of the cost function and optimization procedure can be found in [RD-21].

The MITgcm is suitable for the automatic generation of adjoint code by the Transformation of logarithms in FORTRAN (TAF) source-to-source translator ([RD-59], [RD-60]). Here we use the MITgcm checkpoint 63 with an improved adjoint of a thermodynamic ice model ([RD-48], [RD-61]). The adjoint model was modified here similarly to [RD-43] to exclude KPP module and increase diffusivity values compared to the forward run. Such implementation avoids exponentially growing adjoint variables. The sea ice module was active in the adjoint integration, but the part of the sea ice dynamics which treats rheology was switched off, so that the sea ice model was in a free drift configuration. This approach leads to a reduced (approximate) adjoint producing smoother adjoint gradients. These gradients can still be successfully used to improve the large-scale state of the model (see [RD-62] and [RD-63], for more details). Similar simplifications of the adjoint model were used by [RD-21] and [RD-64] provided an evaluation of the effect of modifications in the parameterizations on the adjoint. They confirm mostly small changes, although regionally some patterns of the gradients may shift. Since the gradients are only a means to find the cost function minimum and the forward code (and thus the minimum itself) is unmodified, changes to the gradient may lead to lower performance in finding the minimum but not to different states once the minimum is found.

The control variables are surface (2 m) air temperature, surface (2 m) specific humidity, surface (10 m) zonal and meridional wind velocity, precipitation rate, downward shortwave radiation, and initial temperature and salinity for the first year of assimilation. For the atmospheric control variables, uncertainties were specified as the maximum of the standard deviation of the NCEP fields for the 1948–2016 time period and the errors for the mean components of air temperature, humidity, precipitation, downward shortwave radiation and wind were specified same as [RD-43]. The uncertainty weights for hydrographic and satellite data are specified to be same as [RD-57]. For the sea ice, a constant error of 50% is employed following [RD-43] for SIC, while the real map of errors of the SIT is used as the uncertainty weights for the thickness.

The initial conditions for the first year (2000) is generated via a 10-year spin-up run, which guarantees the consistency with the ocean-ice dynamics and thermodynamics of the coupled model [RD-21]. The assimilation is carried out in a 1-year truncation. The final state of the previous year's successful iteration is taken as initial conditions for the next year. Therefore, the first iteration in the following year makes already use of an improved initial condition from the assimilation in the previous year and is thus not equivalent to a free run starting from climatology. The optimization procedure is terminated when the cost function differs by less than 1% in two consecutive iterations, which in our case range from 5 (for 2002) to 18 iterations (2007).

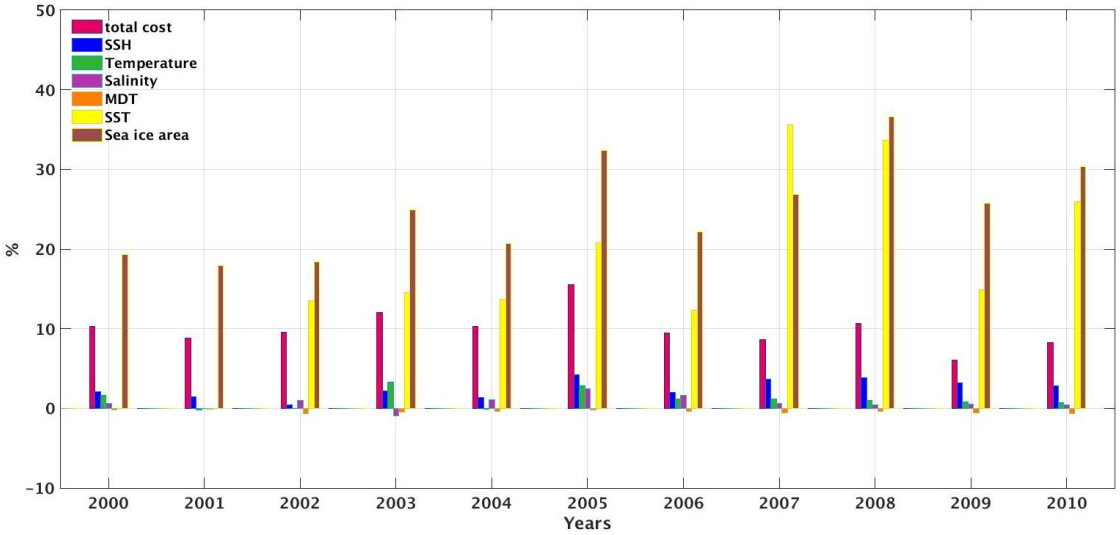

Figure 5-1: Total cost reduction and individual contributions to the reduction from different assimilated variables (without SIT). During the first two years, SST is not assimilated due to lack of data; we decided to continue to use SST data from AMSR-E first data of which are available for May 2002.

Figure 5-1 shows the percentage decrease in model-data differences for the assimilations that only incorporate SIC. The red color indicates reduction in total model-data difference, while other colors indicate the reduction of the differences for individual variables. Negative values mean that there is an increase in model-data difference for that variable.

The cost is dominated by SIC and SST data, which easily respond to the surface controls, and the adjoint method quickly reduces the misfits of those data. It's not surprising that the total reductions of the cost function are mainly from contributions of SIC and SST, given the larger amount of SIC and SST data compared to that of hydrography data. Most of the improvements can be expected for these variables, while changes in the state of the other variables are expected to be relatively small.

Although with similar set-up as [RD-43], the cost reduction performance is different. Instead of a largest total cost reduction (about 16%) in 2008, the largest total reduction (about 16%) until 2010 is obtained for the year 2005 in our study. In contrast, the smallest (about 6%) cost reduction is obtained for the year 2008. Surprisingly, the improvement after assimilation for 2000 is not as good as in [RD-43], although being initialized with same initial conditions and starting from the same value of total cost. For the first iteration during the optimization procedure, a minimal cost value should be defined to generate the first step of the cost reduction. Hence different minimal cost values result in different cost reduction trajectories. Different methods for gaining the gradient of the scalar cost function also contribute to a different final cost values. Besides, sea ice model is chaotic and this would lead to instability in the model simulation. A less accurate final state of the last iteration from 2000 will lead to larger cost at the 1st iteration for the next year in our study. Overall, larger costs are achieved in our study compared with [RD-43].

The average reduction for the years of 2000-2010 is about 10%. The strongest cost reduction for individual variables is obtained for the SST and SIC, with an overall average of about 19% and 25%, respectively. Similar with [RD-43], the least successful cost reduction is obtained for the mean

dynamic topography (MDT), with slightly increased model-data differences for this variable for most years. Compared to a cost reduction of 49% for the sea ice area reported by [RD-21], the sea ice cost reduction is 21% in our work, which may partly due to differences in the first-guess solution [RD-43].

A relatively larger cost function does not necessarily mean a less accurate sea ice reconstruction. In the following we compare the assimilated SIC with satellite data and results from [RD-43], and focus on results related to sea ice changes. For this we choose the years 2005 and 2007; that is a year with local sea ice maximum and the overall minimum sea ice, respectively, for the period considered.

5.3 Sea-ice concentration changes

To evaluate how the data assimilation improves the reconstruction of SIC, we show the spatial distribution for the monthly SIC fields from observations and model runs, as well as the model-data differences for the year 2005 (year of the local maximum) in Figure 5-2. The top row is for winter and the bottom for summer. Larger improvement is derived in summer than in winter. In winter, the differences between the model-data misfits before and after assimilation are basically along the ice edges, considering the fact that in winter the Arctic is largely covered by sea ice. However, the changes for these differences are small and hard to be identified. The most noticeable difference is a small shrink of a tongue for the SIC extending along the east coast of the Greenland. Compared to the results by [RD-43], during March of 2005, the model simulation already bears relatively large error (model simulations against observations) before the assimilation in the east of Greenland, which probably comes from a less accurate assimilation in the previous year of 2004. After assimilation, the errors are reduced for both cases. In summer time, there are improvements both in the position of the sea-ice edge and over the central Arctic for sea ice fields after assimilation. The large positive anomaly of SIC in the Amerasian basin is reduced after assimilation. The amount of sea ice in the central Arctic becomes closer to observations. Errors are largely reduced in the ice edge in the Amerasian basin and in Laptev Sea for summer of 2005 in our study.

Quite similar to 2005, changes of the difference between simulation and observation are hard to identify during March of 2007 (the year of the overall minimum sea-ice cover in the considered period) (Figure 5-2). Largest model-data differences are along the sea-ice edge, in particular along the east coast of Greenland, near Spitsbergen and Franz Joseph Land. There is hardly any change observed for the model results after assimilation. Such a situation was also reported in the results by [RD-43]. The author demonstrated that the dynamical SIC anomaly couldn’t be handled properly by the adjoint model, due to the simplified sea-ice dynamics scheme (free drift) employed. During September of 2007, the model results become closer to observations both in the central Arctic Ocean and for the position of sea-ice edge, in particular along the continental shelf of the Eurasian Basin. Nevertheless, the error of SIC still remains large along the sea-ice edge in the American basin. Compared with the results by [RD-43], larger improvements are found along the continental shelf of the Eurasian Basin in our study and for the sea-ice edge in the Laptev Sea.

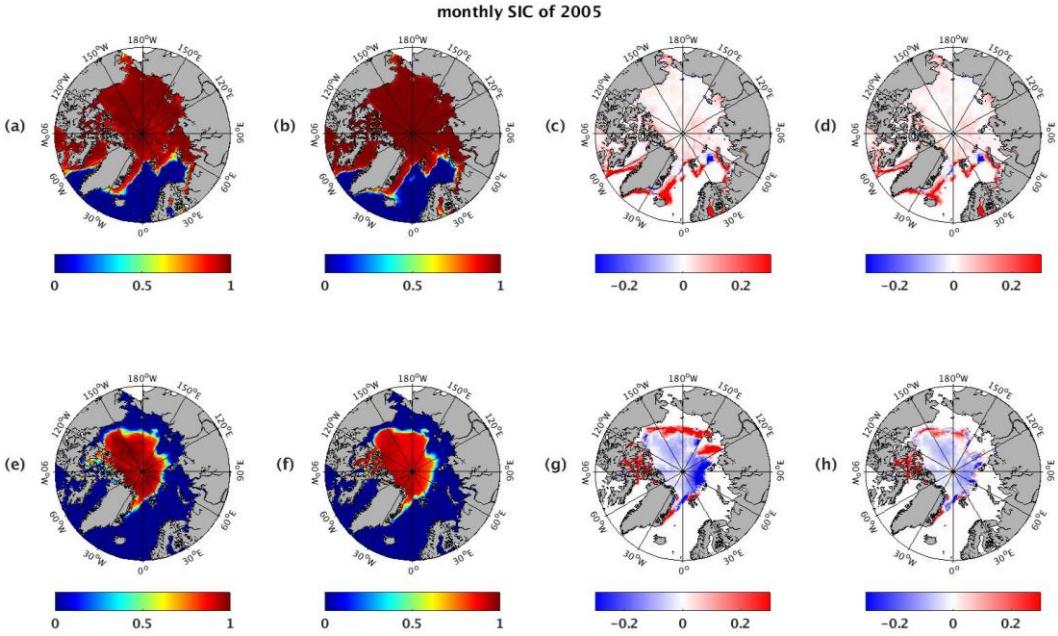

Figure 5-2: Spatial distribution of SIC during March (top) and September (bottom) of 2005, from satellite (a, e) and model runs (b, f). Differences between the satellite data and the model results without corrections (it0) are shown in the third column (c, g), while those with model results from the last assimilation iteration in the fourth column (d, h).

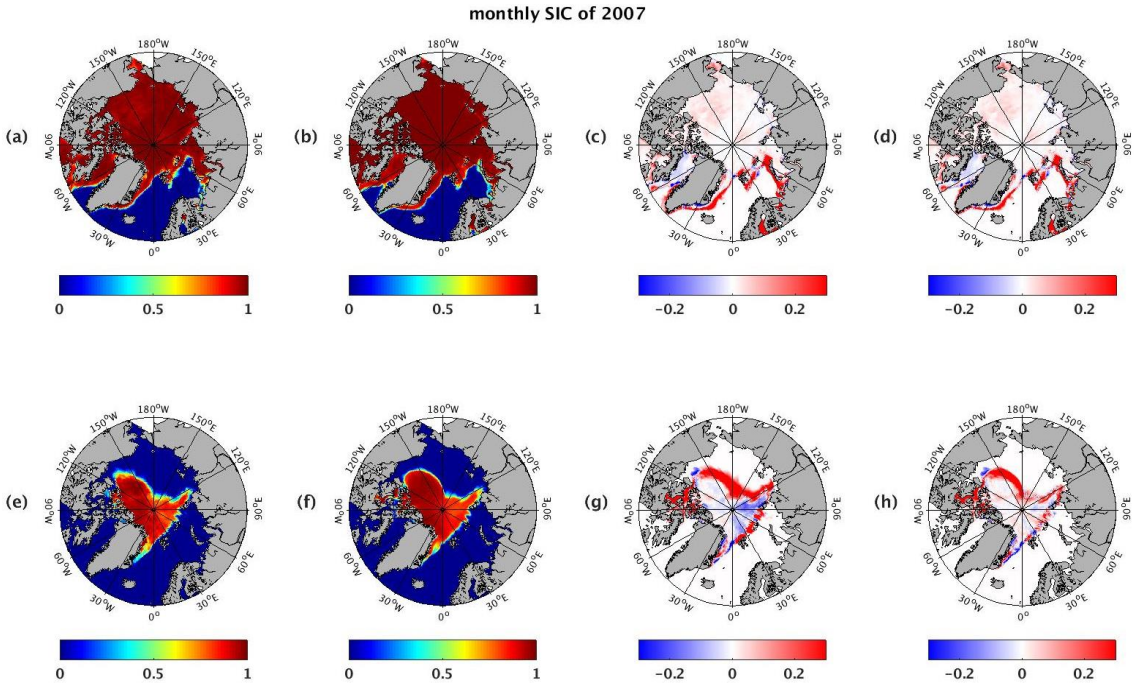

Figure 5-3: Same as Figure 5-2, but for the year 2007.

To summarize, SIC became closer to the observation after assimilation, particularly in summer. Considering the improvement in SIC due to assimilation with a different data set (OSI-SAF by Koldunov et al. versus ESA CCI), the cost reductions of SIC are not as good as in the study by [RD-43] on average. However, considering the monthly model simulations, our

study slightly outperforms the latter in summer, especially for the individual years 2005 and 2007.

5.4 Improvements in sea-ice thickness

The adjoint methodology provides dynamically consistent model solutions. Besides the variables that are directly assimilated, the simulation for other variables such as sea-ice thickness (SIT) may be considerably improved, too. For the analysis of SIT changes as a result of data assimilation, we compare spatial distributions of simulated SIT as a result of SIC assimilation with satellite data, which is shown in Figure 5-4. Here we use the satellite SIT data from ICESat campaigns [RD-58]. ICESat SIT estimates are distributed on a 25 km grid and are considerably larger than those in the simulations, especially in the Canadian sector of the Arctic Ocean. One should note that the uncertainty for this observational data is quite large (just better than 0.7 m; [RD-58], while the spatial distribution of the thickness is probably realistic [RD-65].

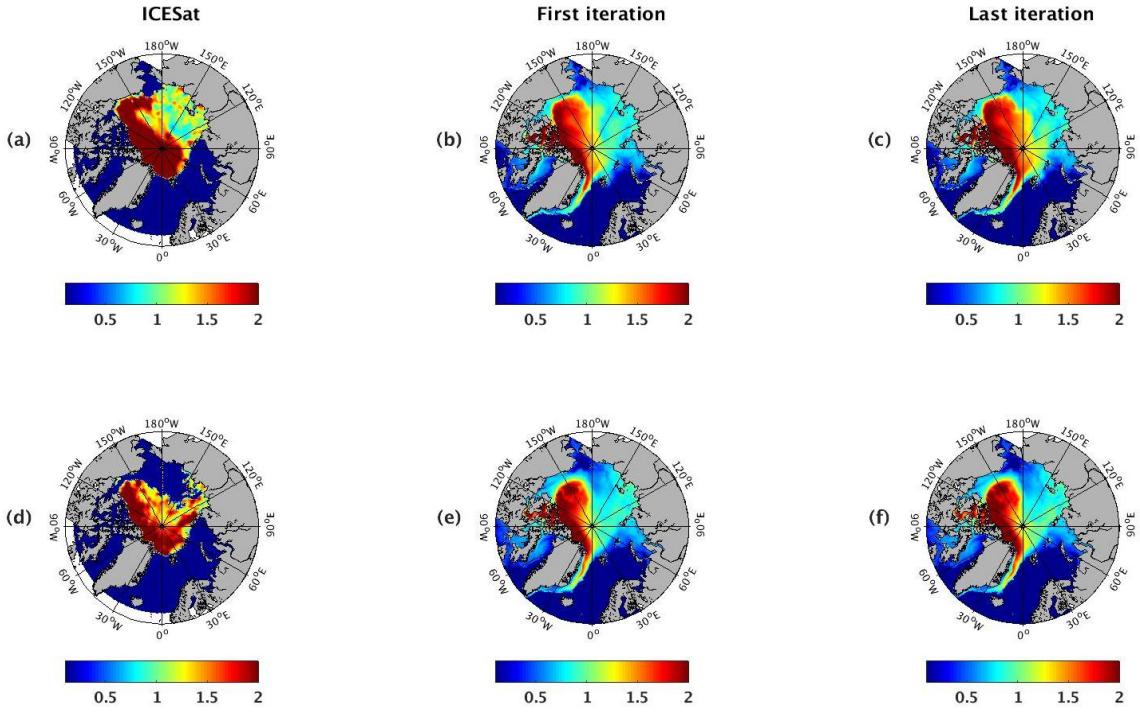

Figure 5-4: Spatial distribution of sea-ice thickness in winter for year 2005 (top row) and 2007 (bottom row). Satellite data (ICEsat, Kwok data; October-November) is shown in the first column (a, d); model simulations without corrections are presented in the second column (November; b, e); model results after assimilation is in the last column (November; c, f).

In general, there is an improvement of the SIT spatial distribution after assimilation. Sea ice became thicker after assimilation in the regions covered by thick ice, such as the central Arctic and the Canadian basin, while thickness tend to decrease in the regions covered with thin ice. Such

tendency was also shown by [RD-21] for the year 2004 and by [RD-43] for years 2005 and 2007. The SIT in October–November 2005 became closer to the observed SIT distribution in the Eurasian Basin of the Arctic Ocean after assimilation, with a considerable increase of around 0.2m. The similarity of the shape between the region with the strong thickness increase in the Eurasian Basin with the shape of the September SIC distribution (Figure 5-2) indicates that it is probably a result of the control variable's corrections that aim to thermodynamically increase SIC in this region [RD-43]. The strongest SIT increase along the sea-ice edge reaches 0.5 m. Results for the year 2007 are similar, with most noticeable improvement in SIT along the continental shelf of the Eurasian Basin. Compare to the year 2005, thickness increase is weaker in this region, reaching only about 0.1 m.

5.5 Summary

Based on a coupled Arctic Ocean–sea ice system, the adjoint methodology is used with the attempt to improve the reproduction of sea ice fields. Results show that the largest improvements happen for the SIC and SST compared with model simulations without data assimilation. The strongest improvements in the SIC are seen during summer months. After assimilation, the position of the sea ice edge becomes closer to observations and SIC in the central Arctic gets closer to observations too.

Compare to the previous work by [RD-43], the performance of total cost reduction after assimilation is different in our work, with relatively smaller cost reduction. However, in respect with the two years 2005 and 2007 that correspond to local sea ice maximum and overall sea ice minimum for the period considered, the improvements for spatial distribution of SIC after assimilation are pretty much similar. Larger improvements are seen in summer, both in the position of sea-ice edge and for SIC in the central Arctic. Our results show slightly better improvements in summer in the Laptev Sea and in the Amerasian/Eurasian basin.

The comparison to available but limited SIT observations shows that SIC assimilation reveals some improvements in SIT despite these observations not being directly assimilated. Improvements in the ocean state are also expected and will be analyzed later on, although the amount of assimilated ocean observations in the water column of the Arctic Ocean is relatively small compared to that of SIC data. The ocean state can be affected indirectly by SIC assimilation due for example to the freshwater fluxes related to the additional melting or freezing and by changes in the ocean exposure to the atmosphere caused by changes in SIC.

As an important climate parameter, SIT influences the heat and freshwater budgets in the ocean-sea ice system. The assimilation of SIT is supposed to improve the reconstruction of sea ice fields (e.g. [RD-41]) and the predictability of sea ice variability ([RD-66], [RD-67]). Based on the ESA CCI 2 SIT and SIC data set, we expect substantial improvements in the reconstruction of sea ice fields with the use of the adjoint assimilation technique. Right now the model is running. But more efforts are needed because the optimization is not working well.

6 SICCI-2 products in Earth-System Modelling (WP4400)

6.1 Introduction

The satellite retrieved sea-ice concentration (SIC) and sea-ice thickness (SIT) provided by the ESA Sea-ice CCI are used in a climate-modelling context primarily for two reasons: First, to evaluate simulations of the past evolution of the polar sea-ice cover, and second to initialize model simulations for seasonal or decadal prediction studies. For both purposes, it is essential that uncertainty information are provided with the satellite-retrieved product, as otherwise a meaningful initialisation or evaluation of an Earth-System-Model will not be possible (see [RD-68] for details). In the following, we will assess the compatibility of the ESA sea-ice CCI products with the sea-ice physics as described by one of the most-advanced, state-of-the-art Earth System Model, MPI-ESM. This model is developed by the Max-Planck-Institute for Meteorology in Hamburg, Germany, and has been shown to reasonably represent the past evolution of the atmosphere [RD-69], the ocean [RD-70] and the sea-ice cover alike [RD-71].

Our approach will be to assimilate SICCI data into MPI-ESM, and to then compare the sea-ice cover of the assimilation simulation with the initial SICCI data. This approach allows us to robustly identify regions where the SICCI data is not compatible with the physics of MPI-ESM. Such mismatch would then be indicative of either issues with the model physics or with the SICCI data.

We will begin with an assessment of sea-ice concentration, followed by an assessment of sea-ice thickness. In both cases, particular attention will be given to utilizing the uncertainty information provided with the final product. From a climate-modeller perspective, this uncertainty information is extremely helpful and one of the main advances in SICCI SIC and SIT over existing products.

6.2 Evaluation of SICCI sea-ice concentration

We carried out an assimilation run with the full Earth System Model MPI-ESM. In all cases, the ocean temperature and ocean salinity were nudged towards the ocean reanalysis ORA-S4, while atmospheric surface pressure, vorticity, divergence and temperature were nudged towards the reanalysis ERA-Interim. Various combinations of sea-ice concentration and sea-ice thickness from SICCI/OSISAF where used to nudge the sea ice towards the observational records.

For all figures shown in the following, we focus on the period January 2011 until December 2014. This represents the overlap period of the SIC and SIT data products we use in the following, and thus allows for a direct comparison between the respective results.

We start with a simulation where only SIC [RD-06] has been nudged towards the observational record (Figure 6-1). The simulated sea-ice thickness is updated proportionally to the updates in sea-ice concentration, as suggested by [RD-37].

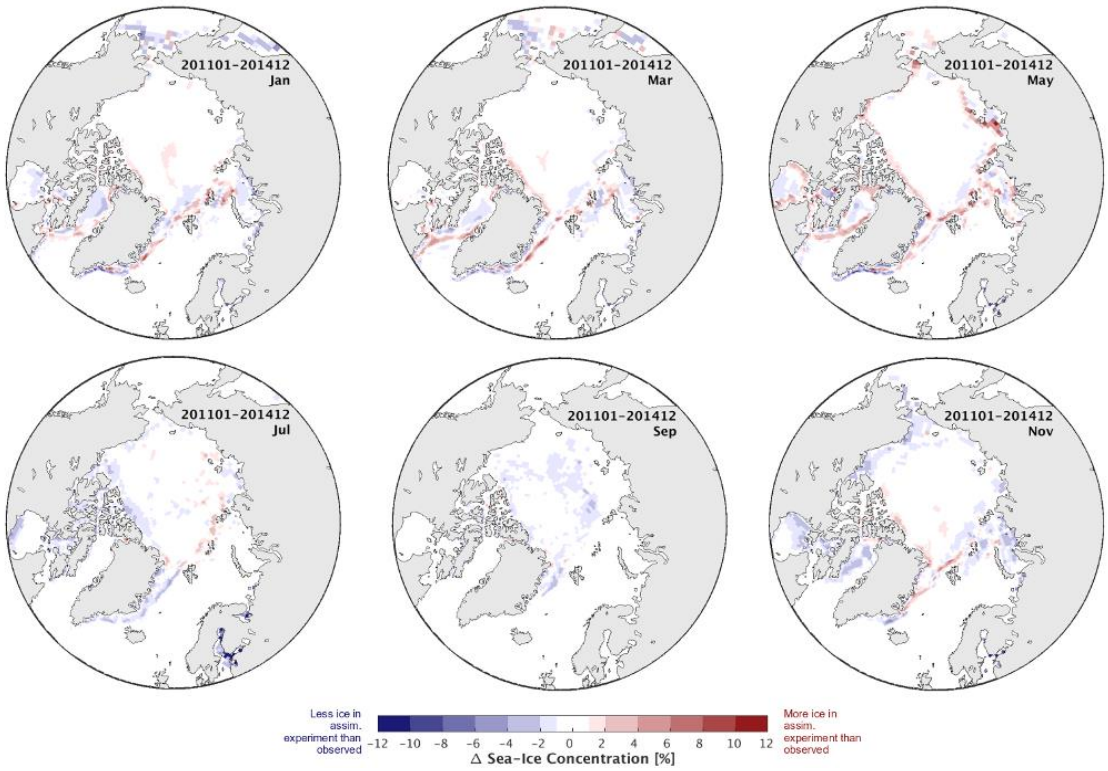

Figure 6-1: Difference between simulated sea-ice concentration (SIC) and OSISAF/SICCI SIC. The simulated sea-ice concentration is obtained from an assimilation run where only OSISAF/SICCI SIC has been assimilated. The modeled SIT was updated proportionally to the updates of SIC.

We find that throughout the year and across the entire Arctic, the modeled sea-ice concentration is very close to the underlying satellite-retrieved sea-ice concentration. In winter, the model tends to produce a slightly larger ice concentration along the ice edge in the European Arctic, where sea ice and open water meet. This is extended towards the Russian Arctic as sea ice begins to retreat from the shores in May. Throughout summer, the model tends to simulate slightly lower sea-ice concentration than retrieved by satellite.

To understand and to judge the relevance of these differences, it is very helpful and instructive to additionally consider the uncertainty of the satellite retrieved sea-ice concentration (Figure 6-2). The SICCI SIC processing chain for the first time allows modelers to examine the uncertainty of the final product, and to exploit this uncertainty to judge the relevance of possible differences between a model simulation and the underlying satellite product.

It turns out that the uncertainties of the sea-ice concentration product are largest in those areas where the differences between model and simulation are largest. For example, in winter, uncertainties of up to 40 % in sea-ice concentration are reported along the ice edge in the European Arctic, spreading to the Russian Arctic in May.

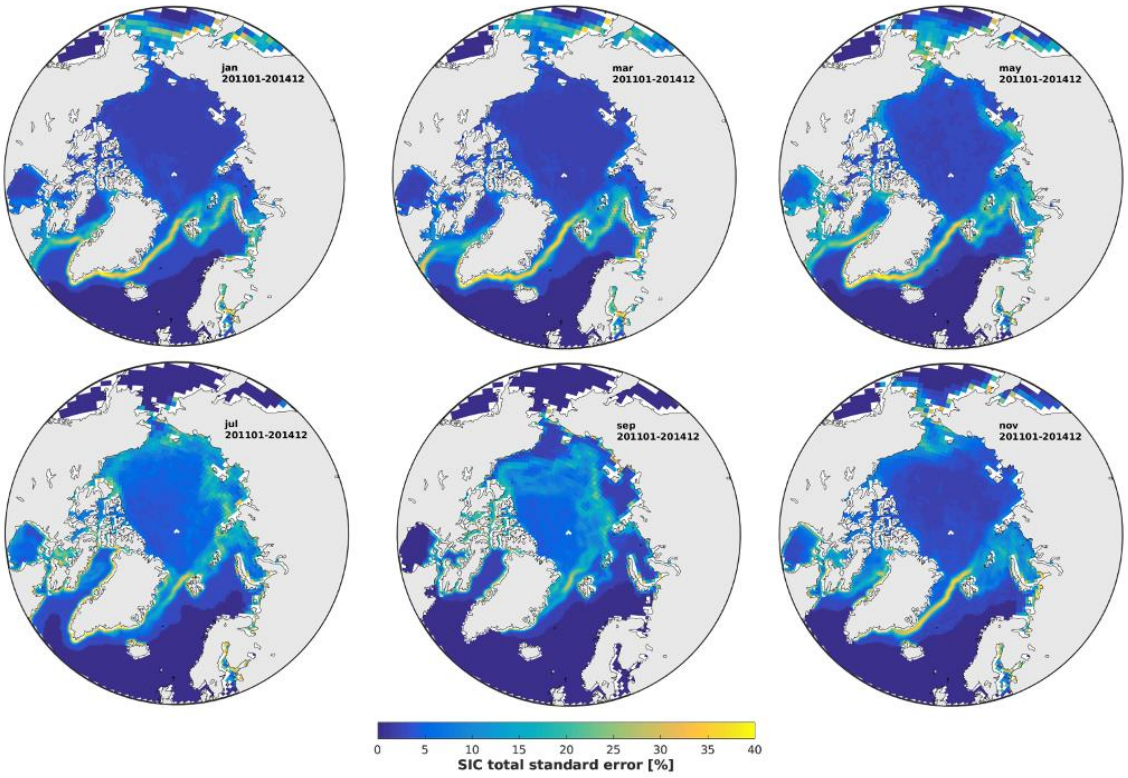

Figure 6-2: Uncertainty of the SICCI SIC product

We can now use the uncertainty information to filter out those regions where differences between the model simulation and the satellite product are smaller than the observational uncertainty (Figure 6-3). Doing so, we find that all identified differences are smaller than the observational uncertainty.

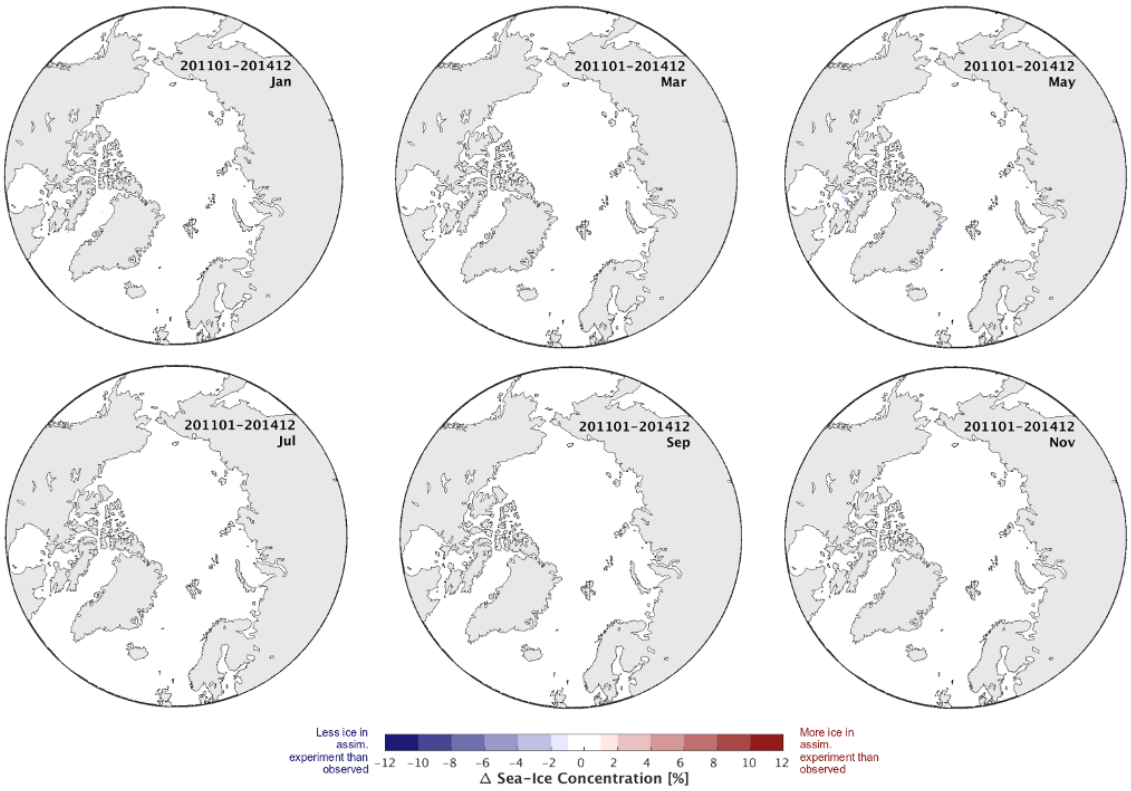

Figure 6-3: As in Figure 6.1, but all regions where the difference between the simulated SIC and SICCI SIC are smaller than the reported uncertainty of SICCI SIC are masked out. This shows that in this case, all differences are smaller than observational uncertainty.

From a modelers' perspective, this allows one to conclude that within observational uncertainty, the model simulation is fully compatible with the underlying satellite product. Without such uncertainty information, one could have been tempted as a modeler to spend unnecessary time and money on trying to improve the seeming disagreement along the ice edge, for example. This is hence one example where the uncertainty information is extremely valuable and of immediate practical use from a climate modelling perspective.

This finding also holds if in addition to OSISAF/SICCI SIC we assimilate SICCI sea-ice thickness (SIT) into our model (Figure 6-4). We note that the differences remain very similar to the simulation with assimilation of SIC only, which indicates that the combination of both products is clearly compatible with the sea-ice physics encoded in MPI-ESM. All differences in SIC remain smaller than the uncertainty of the SIC product.

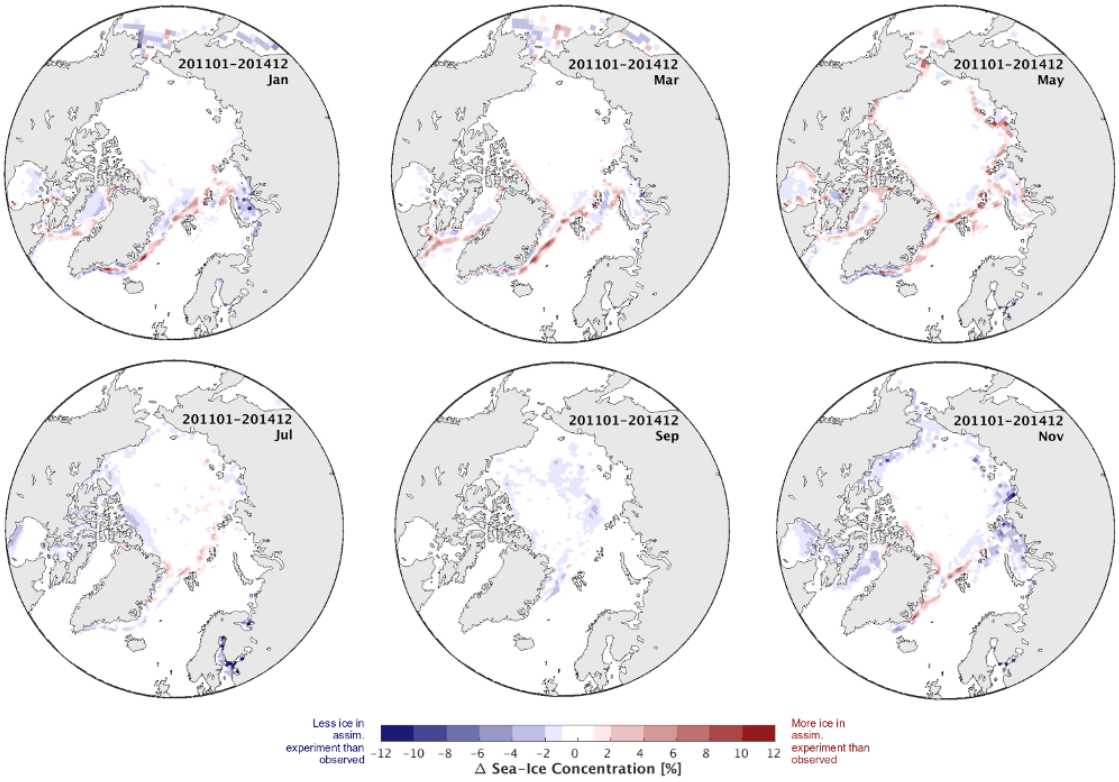

Figure 6-4: Difference between simulated sea-ice concentration (SIC) and OSISAF/SICCI SIC. The simulated sea-ice concentration is obtained from an assimilation run where both OSISAF/SICCI SIC and SICCI SIT have been assimilated. All differences shown here are smaller than the uncertainty of the OSISAF SIC product.

This is, however, not the case if we combine in our assimilation run the OSISAF/SICCI SIC with the sea-ice thickness product obtained from combining Cryosat-2 (CS-2) SIT in regions of thick ice with SMOS SIT in regions of thin ice (Figure 6-5). If we use the Cryosat-2/SMOS product [RD-72] to nudge the ice thickness in our assimilation run, we obtain a substantially increased mismatch between the modelled sea-ice concentration and the sea-ice concentration provided by the underlying SICCI/OSISAF satellite retrieval. For example, in winter the model now simulates far too little ice in many regions, and the errors are larger than the observational uncertainty at least in some parts of the domain (Figure 6-6). This indicates that the CS-2/SMOS sea-ice thickness product at least in some regions is incompatible with SICCI sea-ice concentration relative to our understanding of sea-ice physics as incorporated in MPI-ESM.

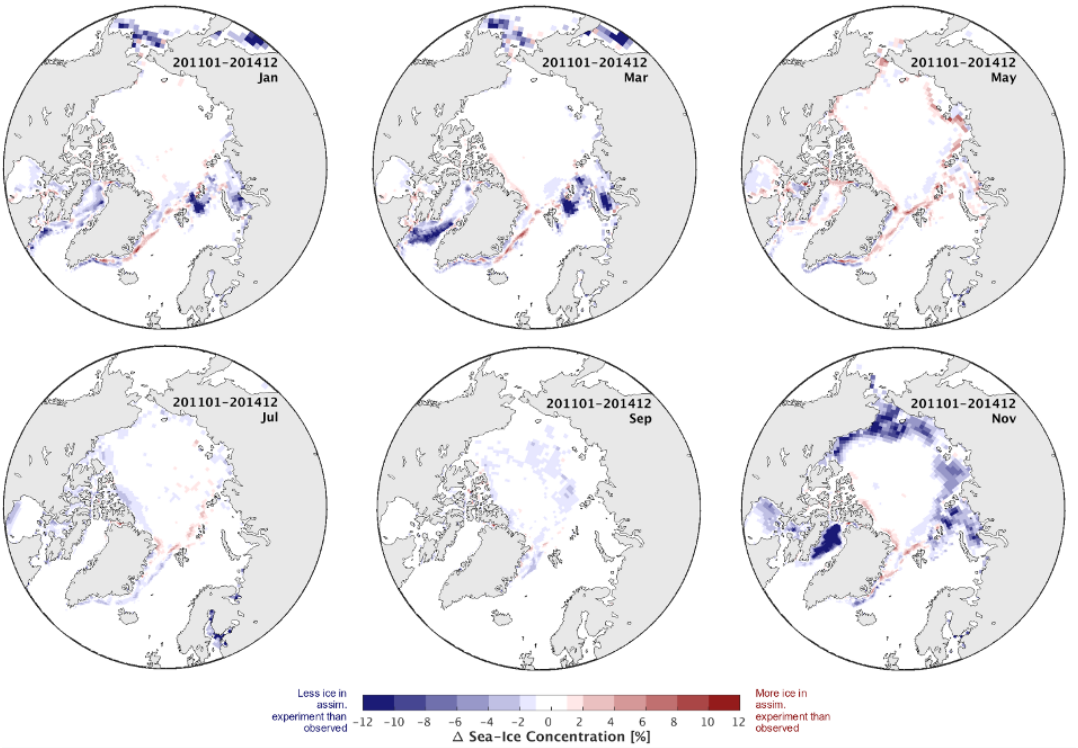

Figure 6-5: Difference between simulated sea-ice concentration (SIC) and SICCI/OSISAF SIC. The simulated sea-ice concentration is obtained from an assimilation run where both SICCI/OSISAF SIC and the CryoSat-2/SMOS SIT have been assimilated.

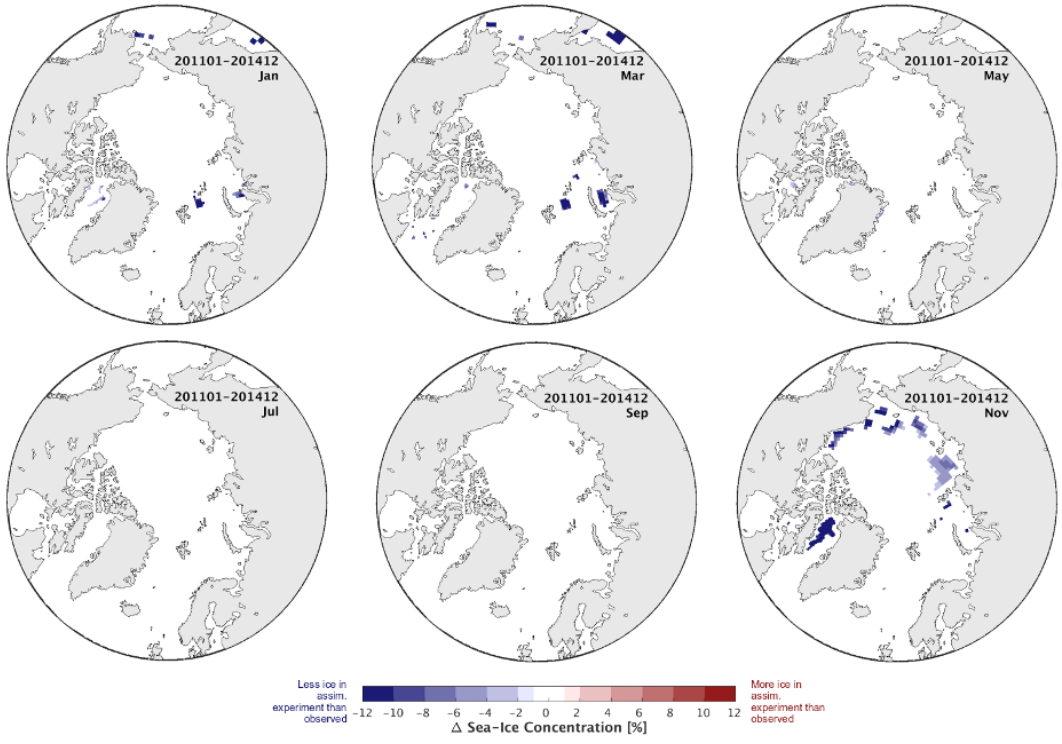

Figure 6-6: As Figure 6-5, but regions are masked where differences are smaller than uncertainties in SICCI/OSISAF-SIC.

6.3 Evaluation of SICCI sea-ice thickness

We now use the same simulations as just discussed, but now evaluate the modelled sea-ice thickness in comparison to the satellite-retrieved sea-ice thickness.

We find that in the simulation where only sea-ice concentration is nudged, while the modelled sea-ice thickness is simply updated proportionally to the updates in sea-ice concentration, the model simulates a large-scale distribution of ice thickness that is substantially different from the one displayed by the SICCI SIT product (Figure 6-7). In particular, the ice in the model simulation tends to be substantially thinner than the satellite-retrieved ice thickness North of Greenland, while the modelled ice is seemingly too thick in much of the remainder of the domain.

While this per se could denote a substantial model deficiency, the interpretation of this result is extremely difficult given the very large reported uncertainty of the SICCI SIT product (Figure 6-8). Across the entire domain, the reported uncertainty of sea-ice thickness is usually above 1 m, which renders the difference between the model simulation and the satellite product insignificant throughout much of the domain (Figure 6-9). From a large-scale model perspective, it is questionable if a product with such large uncertainties can meaningfully be used for climate-model evaluation. These uncertainties should urgently be evaluated, and it should be established that they are indeed realistic. We will return to this issue in the next section, where we outline possible strategies to deal with these large uncertainties from a modelling perspective.

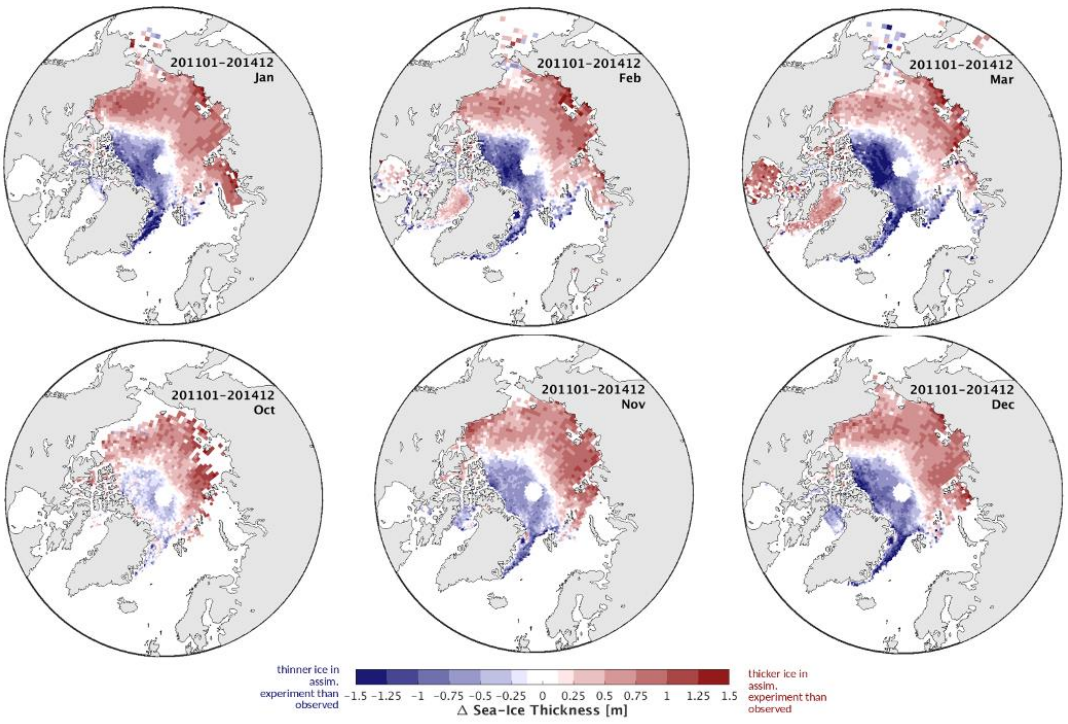

Figure 6-7: Difference between simulated sea-ice thickness (SIT) and SICCI SIT. The simulated sea-ice thickness is obtained from an assimilation run where only SICCI/OSISAF SIC has been assimilated. The modeled SIT was updated proportionally to the updates of SIC.

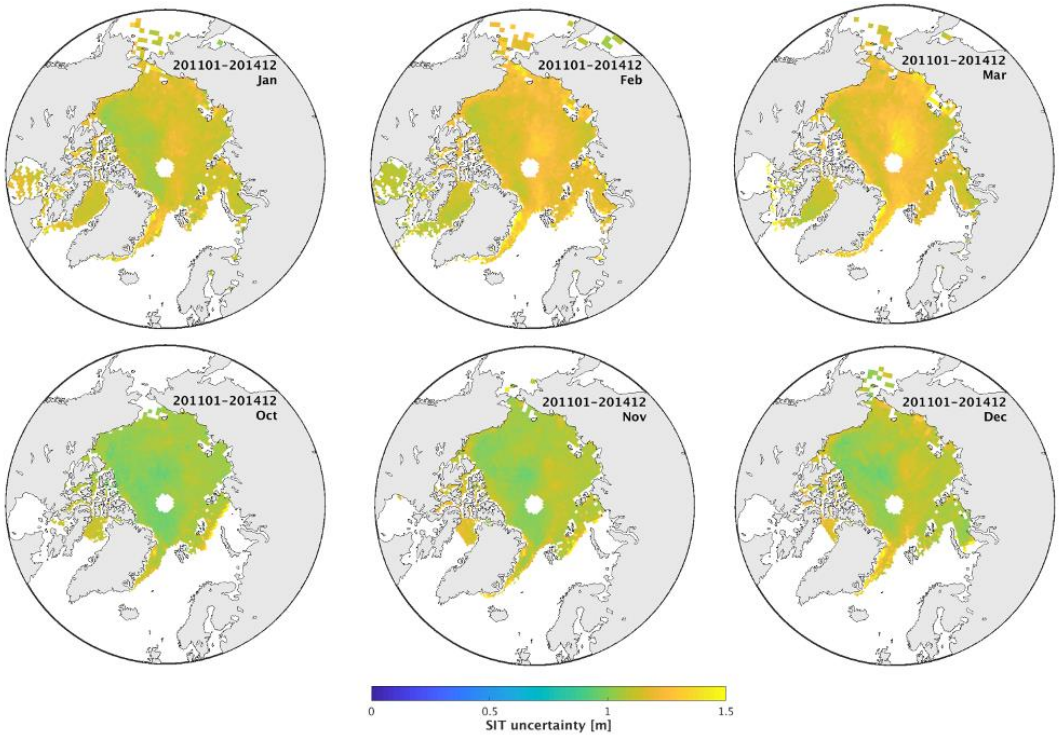

Figure 6-8: Uncertainty of the SICCI SIT product.

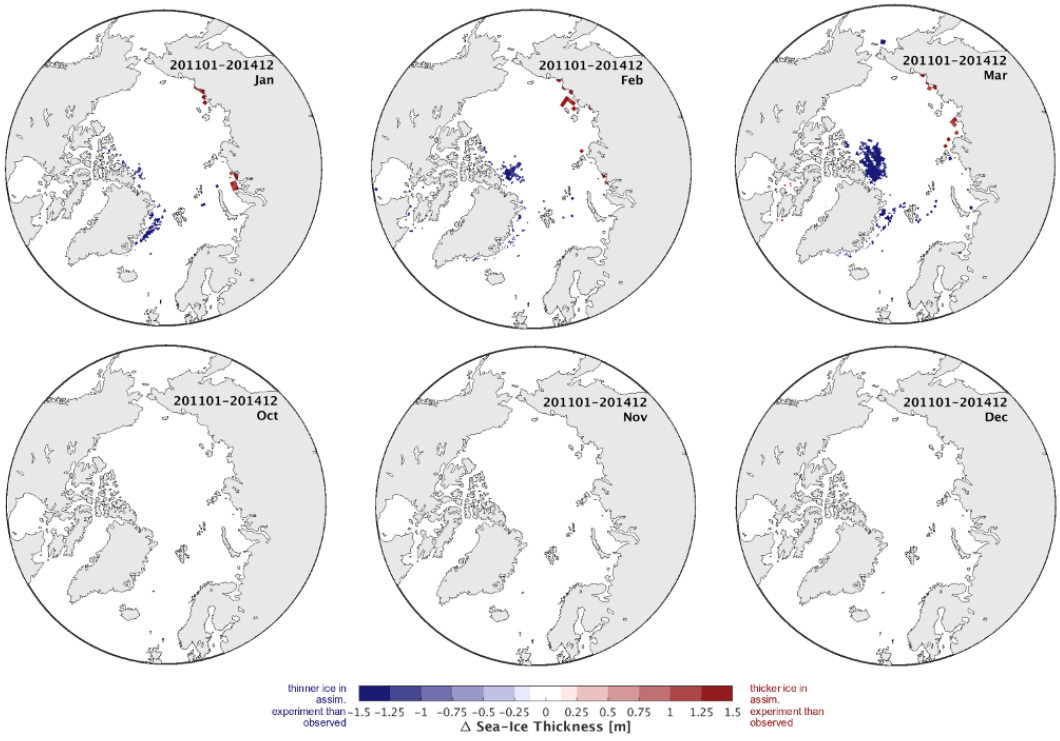

Figure 6-9: As in Figure 6-7, but all regions where the difference between the simulated SIT and SICCI SIT is smaller than the reported uncertainty of SICCI SIT are masked out. This shows that in this case, almost all differences are smaller than observational uncertainty.

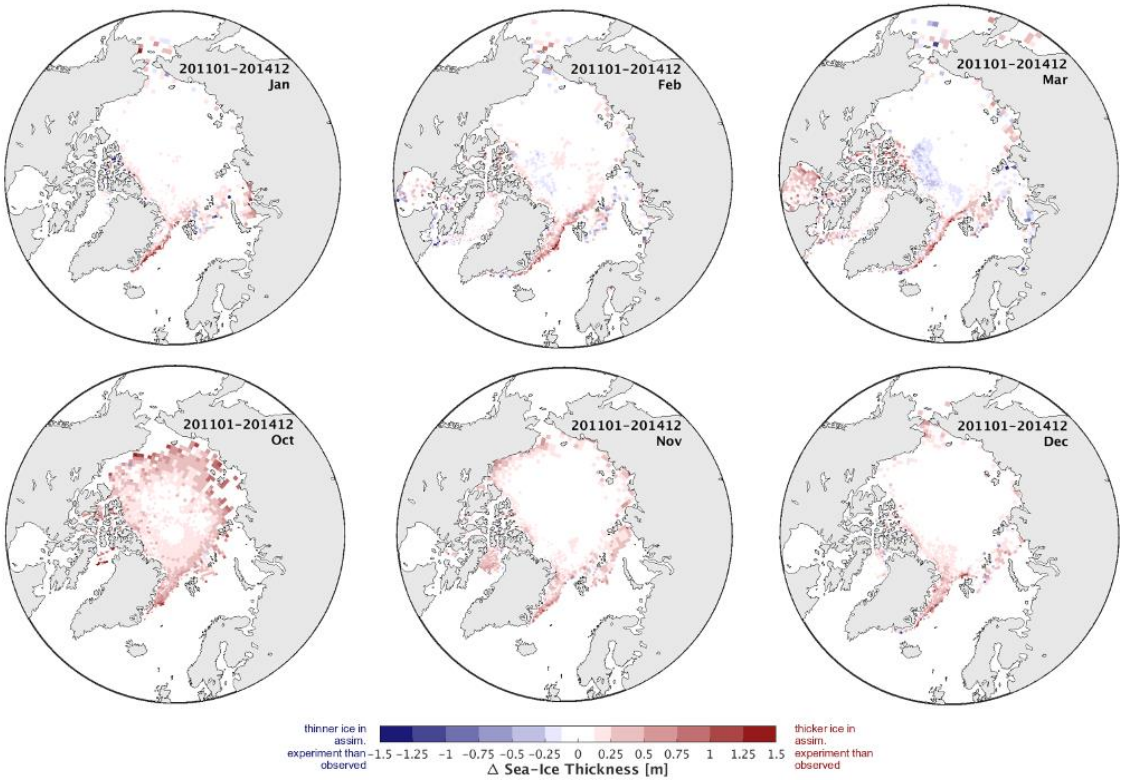

Figure 6-10: Difference between simulated sea-ice thickness (SIT) and SICCI SIT. The simulated sea-ice thickness is obtained from an assimilation run where both SICCI/OSISAF SIC and SICCI SIT have been assimilated. All differences shown here are substantially smaller than the uncertainty of the SICCI SIT product.

If we additionally assimilate either SICCI SIT (Figure 6-10) or CS-2/SMOS SIT (Figure 6-11) into MPI-ESM, the differences in modelled versus satellite-retrieved sea-ice thickness are limited to the ice-edge zone, where the model also showed a mismatch in sea-ice concentration. Only in October, wide-spread differences arise for both SIT products. This, however, can be expected as no SIT information are available throughout summer. Hence, at the end of summer, it can be expected that the model differs from the satellite observation, as it was basically free-running for a couple of months, which then gave rise to the identified biases in sea-ice thickness once satellite data become available again.

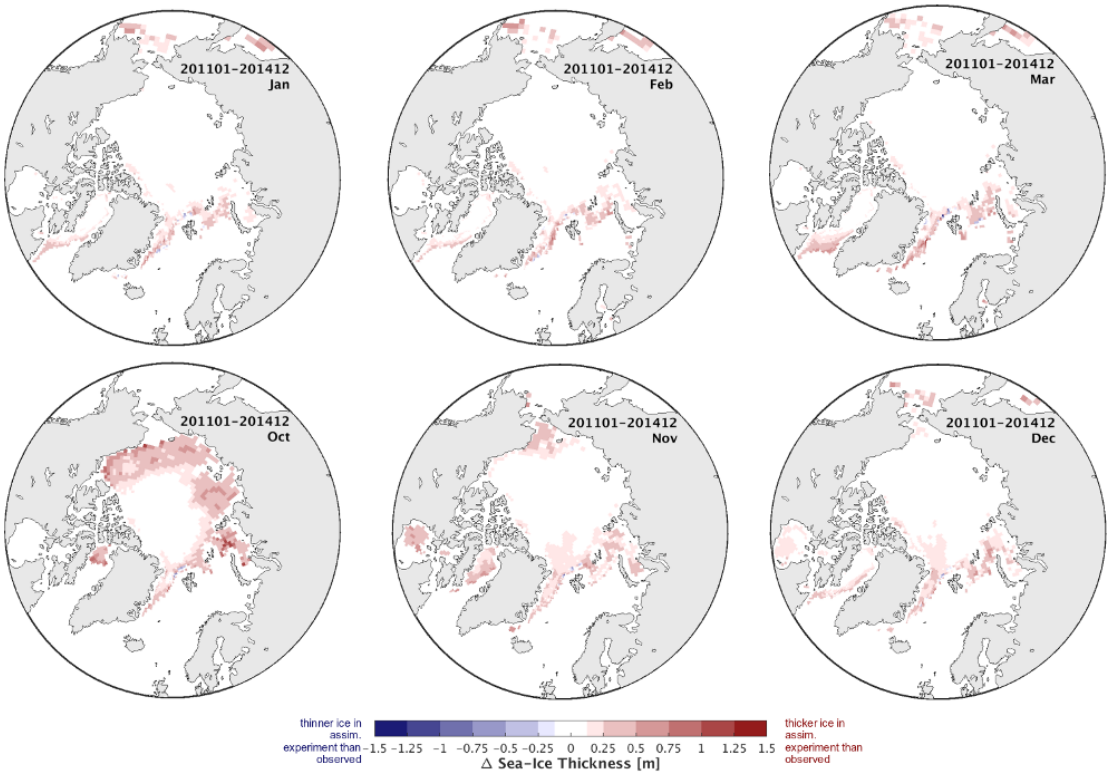

Figure 6-11: Difference between simulated sea-ice thickness (SIT) and CS2/SMOS SIT. The simulated sea-ice thickness is obtained from an assimilation run where both CS2/SMOS SIT and SICCI/OSISAF SIC have been assimilated.

6.4 Evaluating sea-ice freeboard

If we take the reported uncertainty of the SICCI SIT product at face value, this product does not allow for a meaningful initialisation or evaluation of the sea-ice thickness distribution in large scale Earth-System Model simulations. The uncertainty is often 100 % of the reported sea-ice thickness, and hence so large that almost all available output from Earth System Models fall within the reported uncertainty range.

We have hence been working on establishing routines to allow for a more robust evaluation or initialization of our models based on the available information of the SICCI SIT product. It turned out that the available information on sea-ice freeboard (Figure 6-12) and sea-ice radar freeboard are potentially more promising candidates for large-scale model purposes than the sea-ice thickness itself. This is because the reported sea-ice freeboard has a much smaller observational uncertainty than the derived sea-ice thickness (Figure 6-13 and Figure 6-16, also compare [RD-73]).

To examine the feasibility of using the sea-ice freeboard for model evaluation purposes, we calculate the freeboard from the assimilation runs that we also discussed in the previous sections. We find that the apparent biases in sea-ice freeboard obviously mirror the apparent biases in sea-ice thickness, as shown in Figure 6-14 for the assimilation run in which only SIC was assimilated. However, more importantly, in larger regions than before these differences are larger than the observational uncertainty, thus

indicating a robust shortcoming of the model simulation compared to the satellite retrieval (Figure 6-15).

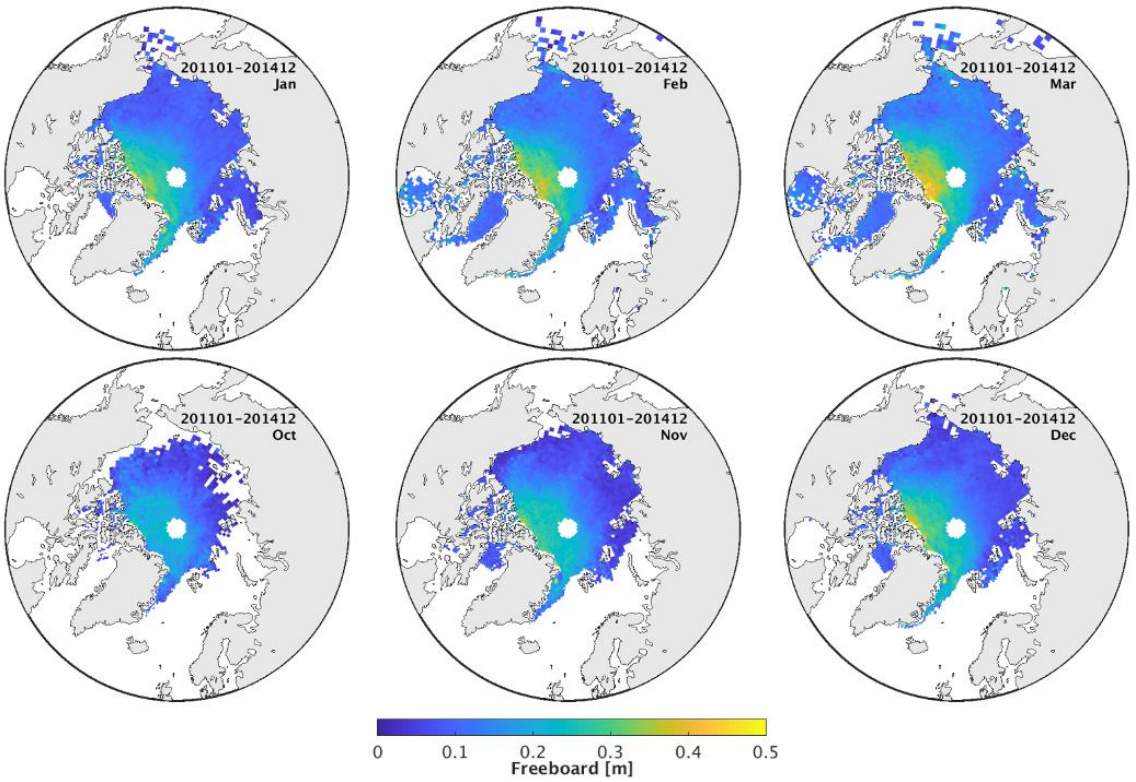

Figure 6-12: SICCI SIT product freeboard.

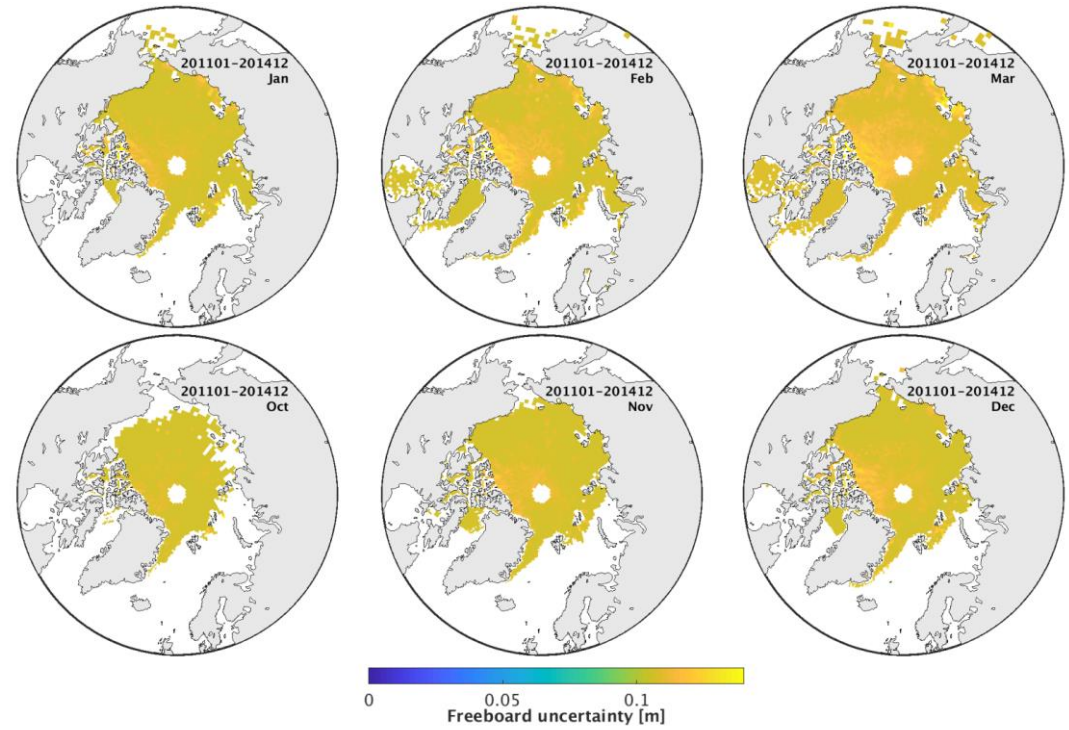

Figure 6-13: SICCI SIT-product freeboard uncertainty.

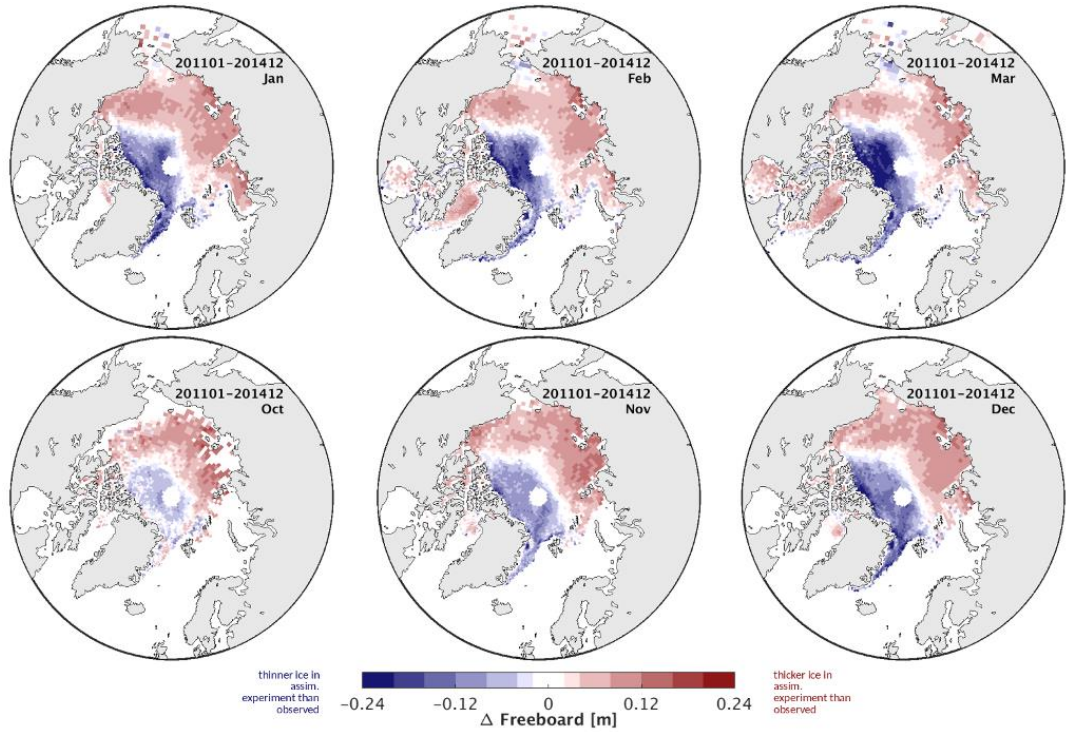

Figure 6-14: Difference between simulated sea-ice freeboard (SIF) and SICCI SIF. The simulated sea-ice freeboard is obtained from an assimilation run where only OSISAF/SICCI SIC has been assimilated. The modeled SIT was updated proportionally to the updates of SIC.

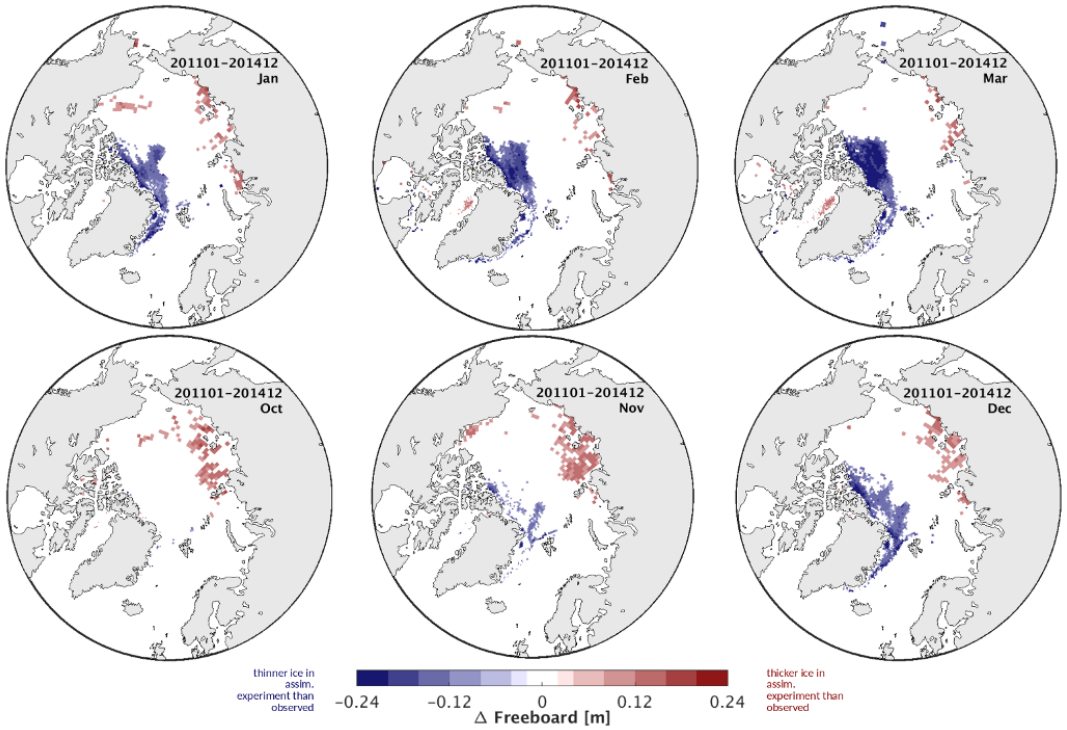

Figure 6-15: As Figure 6-14, but regions are masked where differences are smaller than uncertainties in SICCI-SIF.

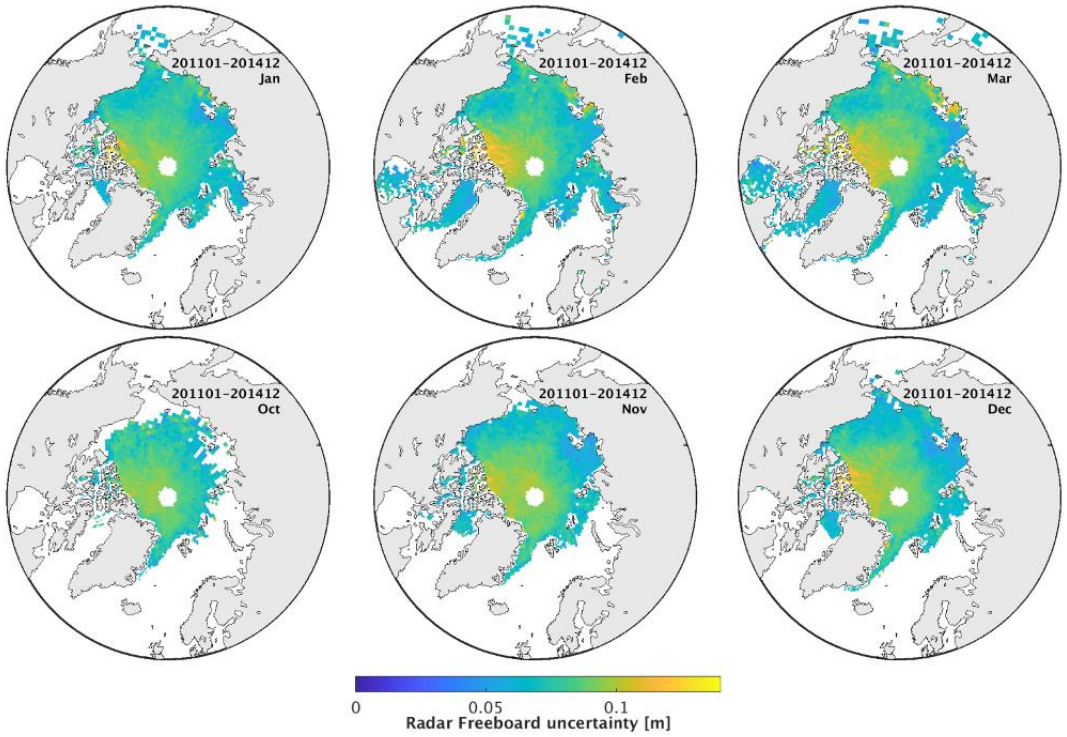

Figure 6-16: SICCI SIT-product radar freeboard uncertainty.

These findings are further amplified if instead of the sea-ice freeboard we use the radar freeboard as reported by the SICCI SIT product. The radar

freeboard is given as the initial freeboard obtained from the SIT algorithm, before the correction for the slower travel speed of the radar signal has been applied. This correction is necessary to obtain a proper sea-ice freeboard, but the snow thickness must be known to apply this correction. Hence, the substantial uncertainty related to snow thickness increases the uncertainty of the resulting sea-ice freeboard relative to the radar freeboard (compare Figure 6-13 and Figure 6-16).

Again, the actual differences look similar to the one obtained for the highest-level product, namely the sea-ice thickness product, as shown here for the simulation where only SICCI SIC has been assimilated (compare Figure 6-7 and Figure 6-17). In contrast to the high-level product, however, the observational uncertainty of radar freeboard are so small that we can now indeed for much of the domain identify a robust model bias, even if those regions are filtered where the differences are smaller than the observational uncertainty (compare Figure 6-9 and Figure 6-18). This also holds if we use for example the simulation where we additionally assimilate SICCI SIT: evaluating radar freeboard, we find significant differences between the simulation and the underlying satellite product that were completely missing when examining significant differences in the high-level product sea-ice thickness (Figure 6-19).

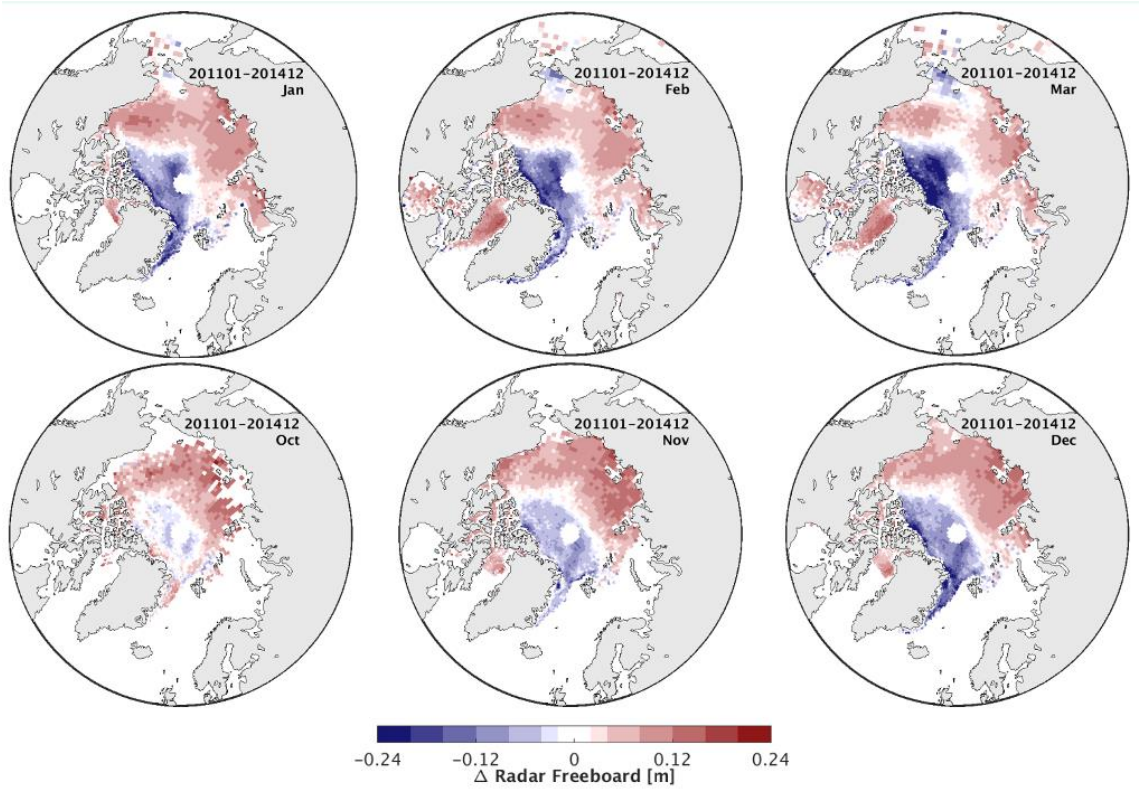

Figure 6-17: Difference between simulated radar sea-ice freeboard (RSIF) and SICCI RSIF. Blue colors denote a smaller freeboard in the simulation than in the original data. The simulated sea-ice freeboard is obtained from an assimilation run where only OSISAF/SICCI SIC has been assimilated. The modeled SIT was updated proportionally to the updates of SIC.

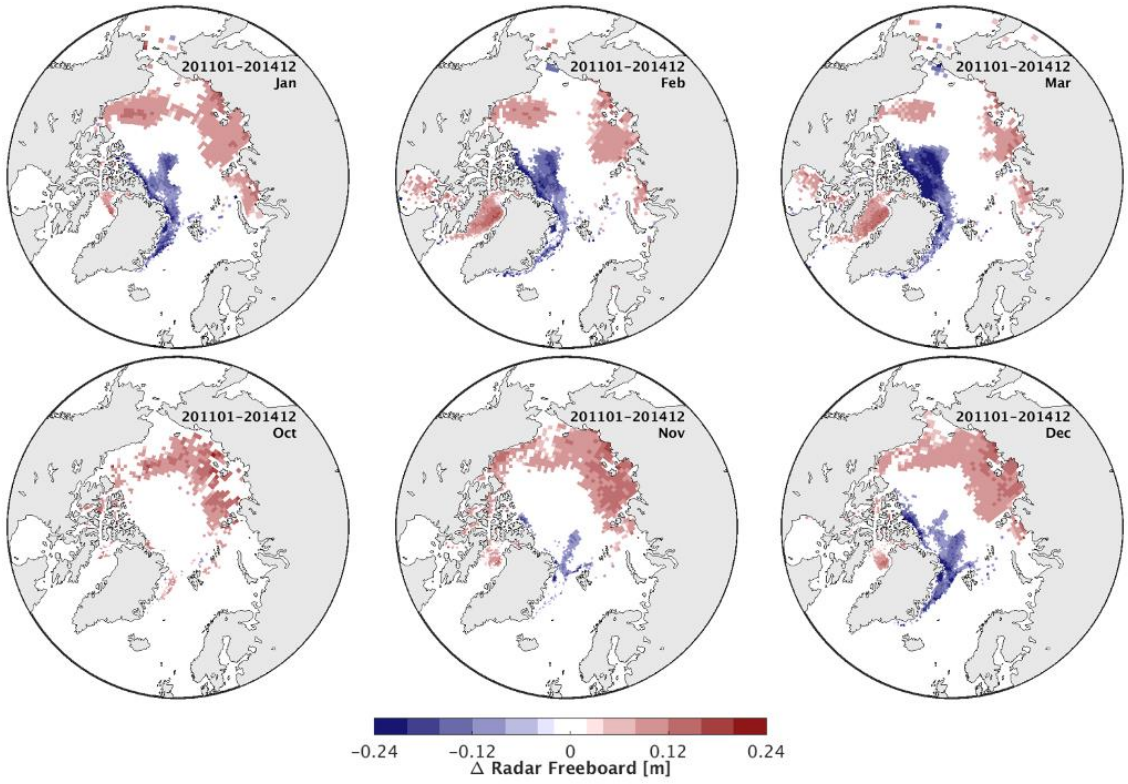

Figure 6-18: As Figure 6-17, but regions are masked where differences are smaller than uncertainties in SICCI-RSIF.

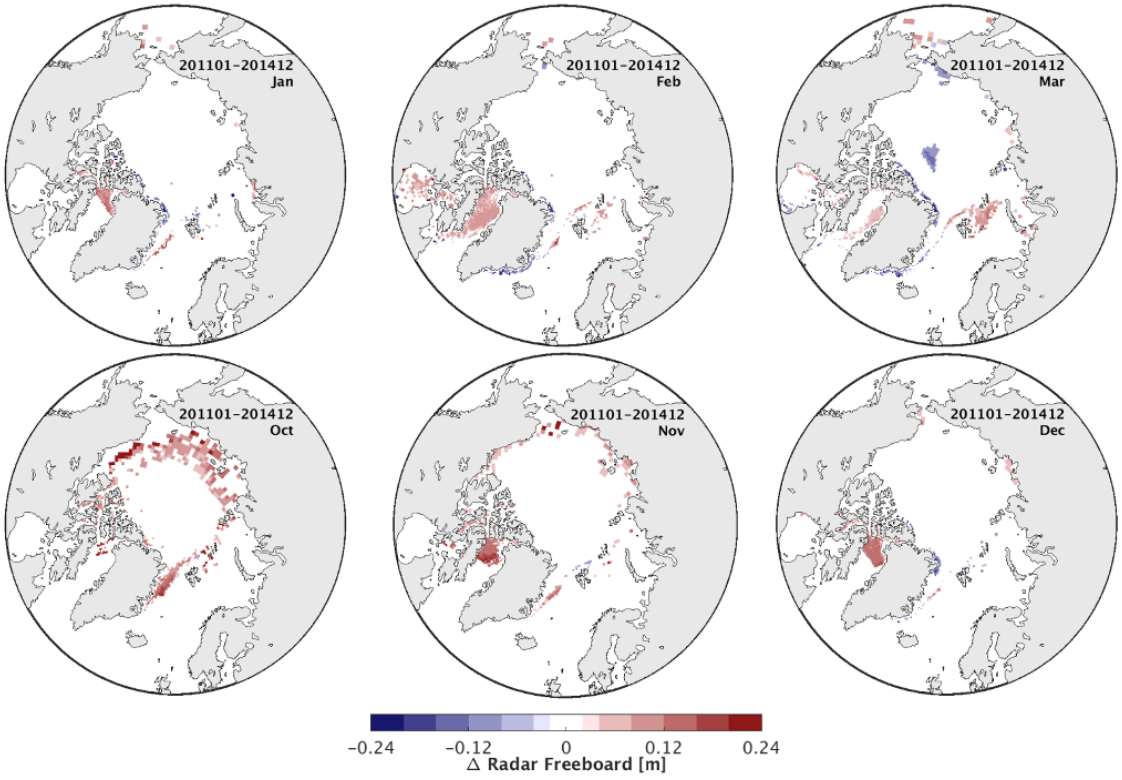

Figure 6-19: Difference between simulated radar sea-ice freeboard (RSIF) and SICCI RSIF. Blue colors denote a smaller freeboard in the simulation than in the original data. The simulated sea-ice freeboard is obtained from an assimilation run where both OSISAF/SICCI SIC and SICCI SIT have been assimilated. All differences are masked white that are smaller than the uncertainties of the SICCI RSIF.

6.5 Impact of the spatial resolution of the SICCI SIC product

From a climate-modelling perspective, a low uncertainty of a given observational product is often more important than a high spatial resolution. Hence, we very much welcome that SICCI SIC is the first product that explicitly addresses this need by providing its sea-ice concentration fields at three different spatial resolutions, namely 12.5x12.5 km^2, 25x25 km^2, and 50x50 km^2.

To test possible changes in the compatibility of these products with the physics described by MPI-ESM, we assimilated sea-ice concentration from all three products into our model and examined the deviation between the initial data and our assimilation run.

We find that all three products are compatible with our model physics to a roughly equal degree, both in winter (Figure 6-20, top row) and in summer (Figure 6-20, bottom row). All differences are smaller than the observational uncertainty reported by the SICCI SIC product.

In winter, the high-resolution product is slightly less compatible with our model physics, in that our model simulates a slightly higher ice concentration North of Greenland compared to the observational records. All other differences are located near the ice edge and similar across all three resolutions.

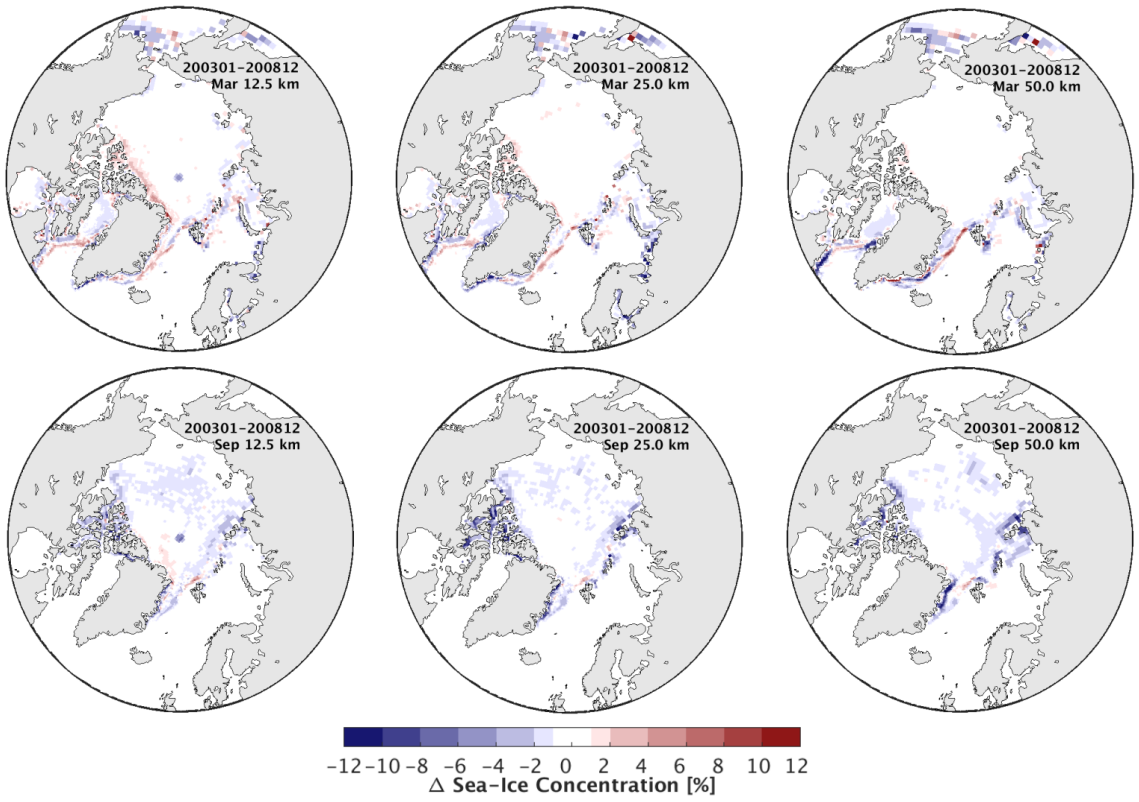

Figure 6-20: Difference between simulated sea-ice concentration (SIC) and SICCI SIC. Blue colors denote a smaller ice concentration in the simulation than in the original data. The simulated sea-ice concentration is obtained from an assimilation run where SICCI SIC at various resolutions has been assimilated. The ice thicknesses were updated proportionally to the updates of SIC. All differences shown here are smaller than the uncertainty of the SICCI SIC product in all grid points.

In summer, the model simulates a slightly smaller ice concentration than the observations over much of the Arctic Ocean for all resolutions. The differences are most pronounced in the Canadian Archipelago and near Severnaja Semlja.

In regards the individual uncertainties, we note that in the interior of the Arctic Ocean, the low resolution product indeed has the lowest uncertainty. Near the ice edge, however, we were surprised to find that there the low-resolution product has the highest uncertainty. We learned that this is because the smearing error as reported in all three products always considers a matrix of 3x3 grid cells, which then for the low-resolution product covers a larger area with larger sea-ice variability compared to the higher-resolution products. It would be helpful if the SICCI SIC team could re-consider this definition and to re-examine whether it is physically plausible that the low resolution product has such high uncertainty near the ice edge, despite its underlying oversampling.

6.6 Summary

In this chapter, we have examined the compatibility of the SICCI products with the sea-ice physics described in large scale earth-system models.

Particular focus has been put on examining the usefulness of the underlying uncertainty information for the purpose of model evaluation.

We have found that for sea-ice concentration, our earth-system model MPI-ESM is fully compatible with the SICCI/OSISAF SIC product, and that all differences between an assimilation simulation and the underlying satellite product are smaller than the observational uncertainty. The differences are largest along the ice edge, where also observational uncertainty is largest. This allows one to conclude that currently, we cannot conclude that the models need to be improved based on the mismatch between SICCI SIC and the assimilation run.

The same holds if we assimilate both SICCI/OSISAF SIC and SICCI SIT. The model can well handle the information from both products and comes up with a model solution that is compatible with the initial data. This is, however, not the case if we replace SICCI SIT with CS-2/SMOS sea-ice thicknesses. This indicated that the compatibility of the SIC and SIT products of SICCI is comparably high given the physics of our earth-system model.

As regards to the sea-ice thickness product, we find that the reported uncertainties are generally too high to allow for a meaningful evaluation of sea-ice model simulations. We urge the SICCI SIT team to carefully examine if (a) the reported uncertainties are realistic and (b) can be reduced.

We further found that from a large-scale modeling perspective, it is much more helpful to evaluate either the modeled sea-ice freeboard or, even more, the modeled radar freeboard. For both properties, the patterns of the mismatch between the model and the observations are comparable, but the uncertainty of the freeboard products is much smaller (also in a relative sense) than the uncertainty of the high-level product sea-ice thickness. Evaluating sea-ice freeboard thus allows for a much more robust identification than evaluating sea-ice thickness with the underlying substantial observational uncertainties.

As regards the three different resolutions, we welcome the inclusion of lower-resolution products as long as they indeed provide lower uncertainties. However, we find that the lowest resolution product only has low uncertainty away from the ice edge, while near the ice edge the error are largest in this product compared to the higher-resolution product. It would be helpful if the SICCI SIC team could examine whether this result is physically plausible, or whether the underlying algorithm for the calculation of uncertainties gives misleading results in this case.

All in all, we are very pleased with the provision of the SICCI SIC and SIT products, and in particular welcome the provision of underlying uncertainties. We would, however, ask both the SIT and the SIC teams to examine whether the reported uncertainties are indeed realistic, and whether they can possibly be diminished, which would in particular be necessary to increase the usefulness of the SIT product.

7 Satellite simulator for Earth-System Models

7.1 Introduction

The most common approach for climate model evaluation is to compare the model output to observations. Models in which the evolution of the variable of interest is closer to the observed evolution tend to be labeled as "better" than those who represent a different evolution. This comparison approach holds if the observations represent the "true" state. However, in the case of sea ice, the observational uncertainty is not negligible. Indeed, different algorithms can be applied to the microwave brightness temperatures measured by satellites to retrieve the observed sea-ice concentration. These different algorithms lead to a spread of up to 10% in the total winter Arctic sea-ice area and up to 25% in the total summer Arctic sea-ice area (Fig. 3 in [RD-74]). We therefore investigate an alternative comparison approach to circumvent observational uncertainty. We propose to compare observed brightness temperatures to simulated brightness temperatures, as would be observed by a satellite flying over the model.

Brightness temperatures depend on the internal structure of the ice and of the snow covering it. This information is not available in a very detailed way in climate models. We therefore explore the feasibility of such a sea-ice satellite simulator on the basis of the limited information contained in the climate model output. To this purpose, we investigate the sensitivity of the surface microwave brightness temperatures simulated by a 1D-microwave emission model (MEMLS) to different sea-ice profile properties, mainly temperature and salinity. We can then determine what complexity the input sea-ice profile needs to provide for realistic brightness temperatures to be simulated. This approach also allows us to compute how much uncertainty is introduced by the reduced complexity of the input profiles. Additionally, we examine relationships between brightness temperatures and liquid water fraction to explore ways to reduce the computational time needed to simulate sea-ice brightness temperatures.

7.2 Method

As a first step, we investigate the sensitivity of simulated microwave brightness temperatures to the sea-ice temperature and salinity profile. To that purpose, we focus on snow-free sea ice and on the microwave brightness temperature simulated directly at the ice’s surface. This allows us to neglect the effect of snow and the atmosphere on the microwave emission. Additionally, we concentrate on the frequency of 6.9 GHz, where the effect of dry snow and the atmosphere are very small, so that we can assume that our results will not fundamentally change even when considering snow and the atmosphere. The spatial resolution at this frequency (75 km x 43 km) is coarse compared to other frequencies but is still comparable to the resolution of a global climate model (around 40 to 100 km). Also, the contrast in emission between open water and sea ice is high at this frequency.

As this is the first such study, we initially aim at minimizing the impact of observational uncertainty and GCM uncertainty for the purpose of our feasibility study. We hence explore a perfect-model setup, where we use a complex one-dimensional sea-ice model to simulate both detailed profiles of sea-ice properties that represent the "real" world and simplified profiles of sea-ice properties that represent the "GCM" world. Our "real" world are

profiles computed by the complex thermodynamical 1D sea-ice model SAMSIM ([RD-75], [RD-76]) using forcing from ERA-Interim. Our "GCM" world are simplified versions of the "real" world profiles. Specifically, we emulate a profile that could be inferred from model output of the Max Planck Institute Earth System Model (MPI-ESM). In these simplified profiles, we take the temperature profile as linear between the surface temperature and the water temperature (-1.8 °C). For the salinity profiles, we investigate two simplification possibilities: salinity as a function of depth as defined in [RD-76] and constant salinity over depth (5 g/kg for first-year ice and 1 g/kg for multiyear ice). The "real world" and "GCM" profiles are then used as input for the microwave emission model MEMLS ([RD-77], [RD-78]). MEMLS computes different sets of brightness temperatures based on the different input profiles: the "real" brightness temperatures and the "GCM emulated" brightness temperatures (Figure 7-1). These can then be compared to get insight into the sensitivity of brightness temperatures to different input profile parameters.

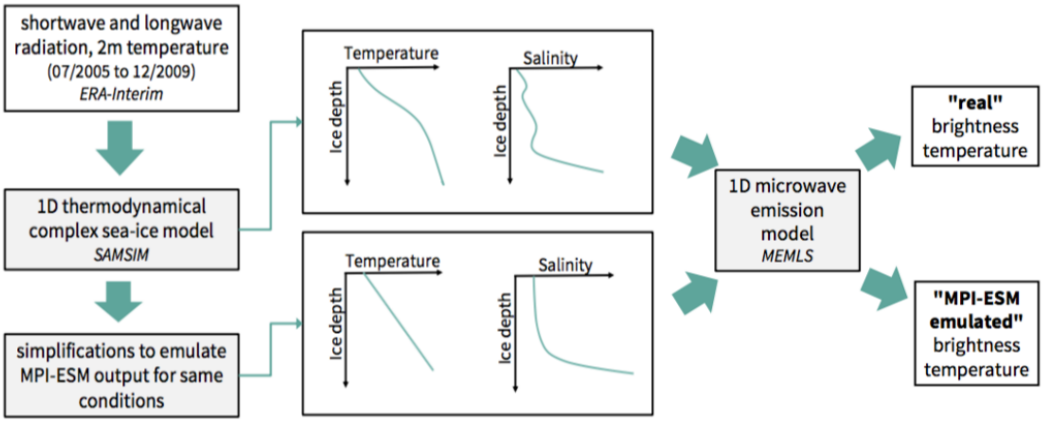

Figure 7-1: Schematic of the steps of our simulation and comparison method.

7.3 Results and discussion

7.3.1 Sensitivity studies

As a first step, we run a brightness temperature simulation with complex temperature and salinity profiles (our "real" world) as input and a brightness temperature simulation with simple temperature and salinity profiles (our "GCM"). We find that the results for first-year ice can be divided into two seasons (Figure 7-3): winter (from October to March) and summer (from April to September). In winter, the resulting brightness temperatures agree well, with a difference between the two resulting brightness temperatures of (2.9±3.8) K when the simple salinity is a function of depth (Figure 7-3 a) and of (3.1±3.9) K when the simple salinity is constant throughout depth (Figure 7-3 c). As a result, we conclude that the temperature and salinity simplifications do not affect the simulated brightness temperature to a very high degree.

In summer, the difference is larger, respectively (45.7±45.1) K (Figure 7-3 c) and (46.5±44.8) K (Figure 7-3 d). These large differences are mostly the result of differences in the surface liquid water fraction (see Figure 7-2,

Table 7-1). While often the surface liquid water fraction is high in the in the simple profiles, it remains low in complex profiles. These differences in liquid water fraction are induced by temperatures near 0°C and different salinities at the surface. At temperatures near 0°C, even slight differences in temperature and salinity lead to very large differences in liquid water fraction. In the simple profiles the surface salinity is slightly higher than in the complex profiles, therefore leading to surface liquid water fractions as high as one. A liquid water fraction of one at the surface means that the surface emits brightness temperatures similar to water (near 160 K) rather than similar to pure ice (around 260 K). This phenomenon can be explained by the strong relationship we find between surface liquid water fraction and brightness temperature (Figure 7-2). For surface liquid water fractions above 0.2, the brightness temperature directly depends on it and can be inferred from the surface liquid water fraction directly. This relationship holds a little less strong for H-polarization as well (Table 7-1).

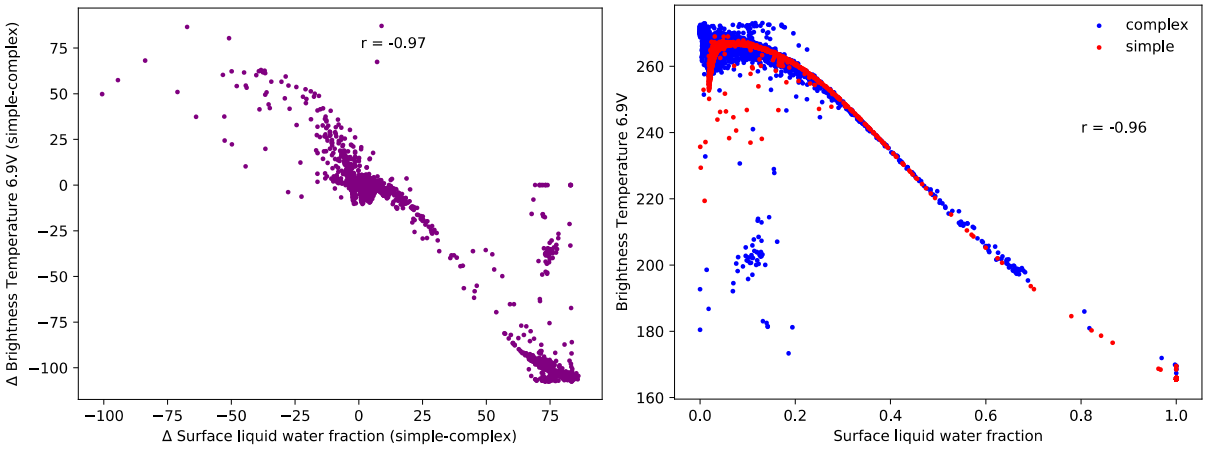

(a) ΔTBV vs Δsurface lwf (b) TB vs lwf

Figure 7-2: Difference in (a) and absolute (b) brightness temperatures at 6.9 GHz (V-polarization), as a function of the difference in (a) and the absolute (b) surface liquid water fraction (lwf).

Table 7-1: Correlation coefficient between the two variables given in the column and line description. Δ means the difference between the surface layer of the simple and complex profile. FYI = first-year ice, MYI multiyear ice, TB = brightness temperature. The surface temperature is not shown as it is the same in both profiles by definition of the method.

	ΔTB V-polarization			ΔTB H-polarization		
surface parameters	all year	summer	winter	all year	summer	winter
FYI Δ salinity	-0.47	-0.57	-0.42	-0.52	-0.61	-0.32
FYI Δ density	-0.95	-0.94	-0.53	-0.89	-0.92	-0.31
FYI Δ liquid water fraction	-0.97	-0.96	-0.75	-0.91	-0.94	-0.41
MYI Δ salinity	0.05	0.10	-0.002	0.04	0.08	-0.06
MYI Δ density	0.27	0.34	0.03	0.20	0.26	0.04
MYI Δ liquid water fraction	0.89	0.89	-0.04	0.64	0.62	-0.04

We therefore conclude in a first step that, to simulate realistic brightness temperatures, having a complex profile is much more important in summer than in winter. However, in summer, most of the information driving the brightness temperature is contained in the very upper layers. It is therefore

more important to yield a realistic simplified temperature and salinity profile in the upper layers than over the whole depth of the ice. Having a good representation of ice surface properties allows to infer the brightness temperature directly from surface liquid water fraction if the latter is higher than 0.2. Also, we find that a salinity profile as a function of depth yields slightly more realistic brightness temperatures than a constant salinity profile.

For multiyear ice, the difference in brightness temperature is induced by differences in surface liquid water fraction in summer as well (Table 7-1). In winter, however, the emission appears to come from deeper layers. A similar relationship with properties in deeper layer might be uncovered after further analysis.

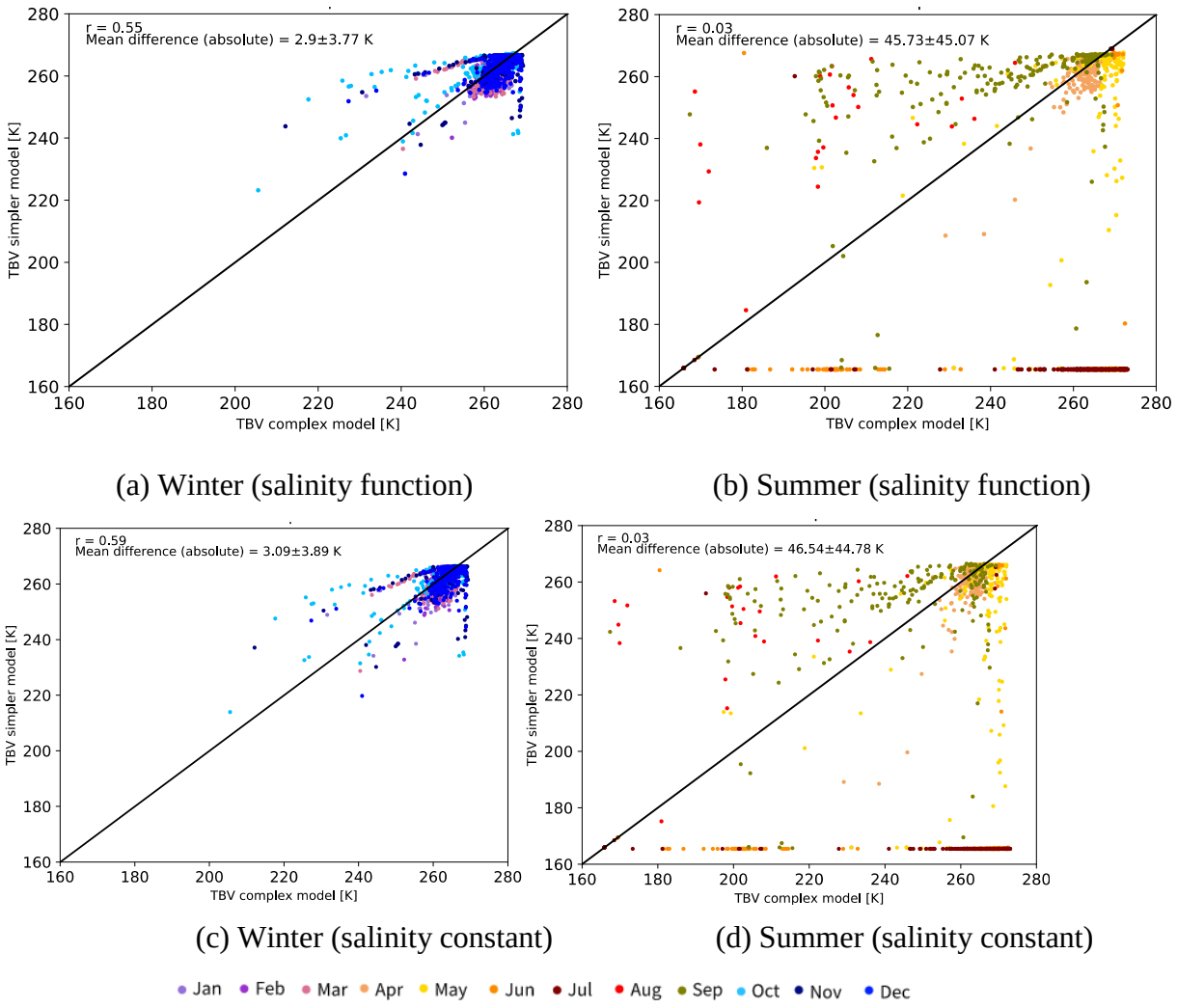

(a) Winter (salinity function) (b) Summer (salinity function)

(c) Winter (salinity constant) (d) Summer (salinity constant)

Figure 7-3: Brightness temperatures at 6.9 GHz, vertical polarization, x-axis: resulting from complex profile, y-axis: resulting from simplified profile, first-year ice. Colors represent the different months (summer: April to September, winter: October to March).

In a second step, we investigate which of the two simplifications (temperature or salinity) introduces most of the difference in brightness temperatures. To this end, we run three additional brightness temperature simulations. In the first, called "simpletemp" in the following, we use the

linear temperature profile but keep the complex salinity profile. In the second, called "simplesalfunc" in the following, we use the salinity profile as a function of depth but keep the complex temperature profile. In the third, called "simplesalconst" in the following, we use the salinity profile as a constant over depth but keep the complex temperature profile. This way, we can discriminate the effect of the different simplifications on the simulated brightness temperature. We find that, while the temperature simplification only introduces a difference of (3.9±11.2) K to the brightness temperature simulated based on complex profiles (Figure 7-4), the simplification of the salinity profile introduces a difference (19.9±36.2) K (simplesalfunc, Figure 7-4 b) and (20.3±36.2) K (simplesalconst, Figure 7-4 c) respectively.

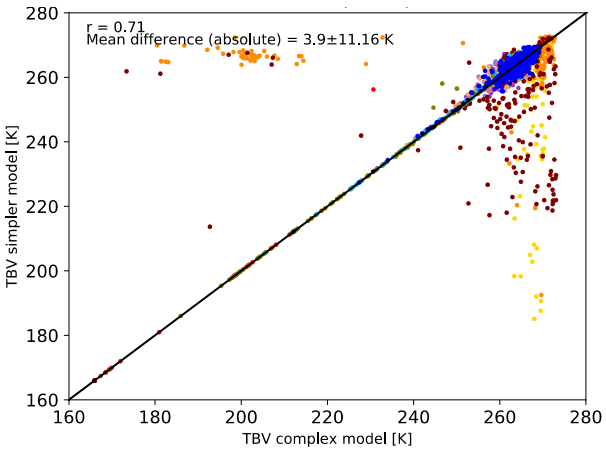

(a) Only simple temperature profile

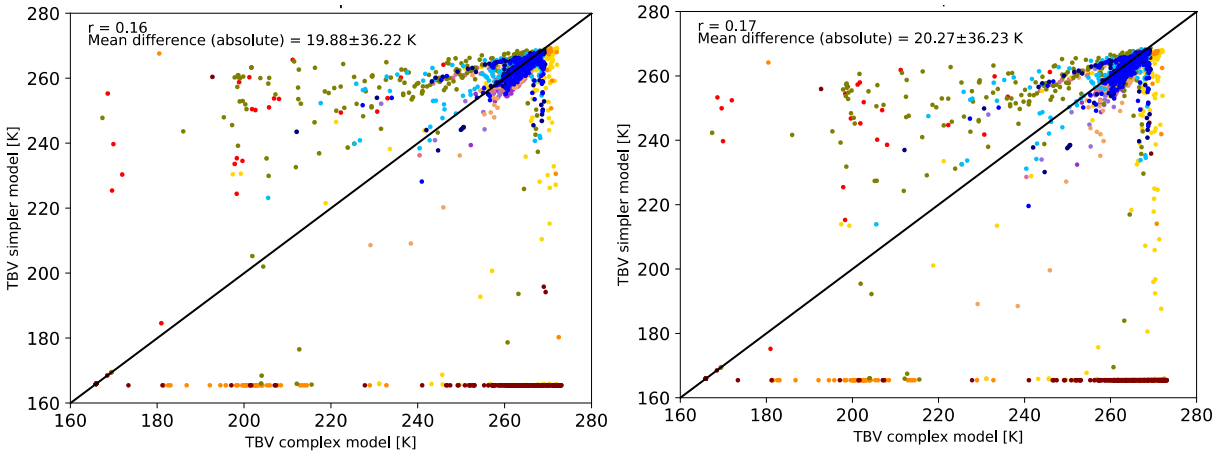

(b) Only simple salinity profile (function) (c) Only simple salinity profile (constant)

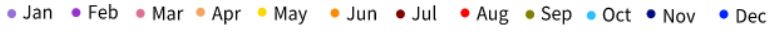

Figure 7-4: Brightness temperatures at 6.9 GHz, vertical polarization, x-axis: resulting from complex profile, y-axis: resulting from (semi-)simplified profile, first-year ice. Colors represent the different months (summer: April to September, winter: October to March).

These results are slightly higher for multiyear ice, so we will not discuss the multiyear ice more in detail (Table 7-2). For the horizontal polarization, the difference is also slightly higher in the mean but shows a much higher

standard deviation. More investigation is needed to understand which parameter is driving this large spread (Table 7-2).

Table 7-2: Mean difference, standard deviation of difference and correlation coefficient between simple and complex brightness temperatures. FYI = first-year ice, MYI multiyear ice, TB = brightness temperature.

		First-year ice			Multiyear ice		
		all year	winter	summer	all year	winter	summer
TB V-polarization							
simpletemp	Δ	3.9±11.2	1.3±1.2	7.6±16.7	3.7±7.2	3.1±2.7	4.2±10.6
	r	0.71	0.95	0.67	0.93	0.86	0.93
simplesalfunc	Δ	19.9±36.2	2.0±3.7	45.5±45.4	8.7±20.5	4.4±5.5	12.9±27.9
	r	0.16	0.64	0.03	0.66	0.60	0.66
simpleallfunc	Δ	20.5±35.9	2.9±3.8	45.7±45.1	16.8±29.0	6.0±6.0	26.6±37.1
	r	0.16	0.55	0.03	0.46	0.39	0.48
simplesalconst	Δ	20.3±36.2	2.2±3.8	46.1±45.2	22.9±39.5	4.5±5.4	41.4±49.3
	r	0.17	0.66	0.03	0.27	0.57	0.28
simpleallconst	Δ	20.9±35.9	1.3±3.9	46.5±44.8	24.4±38.8	6.8±5.9	42.1±48.6
	r	0.17	0.59	0.03	0.26	0.32	0.28
TB H-polarization							
simpletemp	Δ	5.8±16.0	1.5±4.1	2.0±23.2	7.4±17.4	3.8±4.7	10.7±22.5
	r	0.88	0.99	0.81	0.91	0.95	0.90
simplesalfunc	Δ	33.9±47.6	12.0±20.2	65.4±57.1	9.6±17.9	3.8±4.7	15.4±23.5
	r	0.26	0.58	0.06	0.91	0.98	0.88
simpleallfunc	Δ	34.0±47.6	12.1±20.1	65.4±57.1	12.8±20.6	6.3±8.7	18.8±25.9
	r	0.25	0.58	0.06	0.90	0.92	0.89
simplesalconst	Δ	35.1±47.8	13.3±21.2	66.4±57.0	36.3±54.7	8.7±6.8	64.0±66.5
	r	0.26	0.55	0.07	0.63	0.96	0.55
simpleallconst	Δ	35.5±47.7	13.6±21.5	66.8±56.8	40.0±54.0	15.5±17.3	64.6±65.8
	r	0.25	0.53	0.06	0.61	0.77	0.55

7.3.2 Quantifying uncertainties

The aim of using a sea-ice satellite simulator is to reduce the uncertainty introduced by retrieval algorithms in the comparison between models and observations. As several simplifications are used in our tentative simulator, we need to assess if the simulated brightness temperatures are realistic enough to indeed reduce the uncertainty in the comparison. This uncertainty also depends on the sea-ice concentration itself, as realistic ice brightness temperatures are more important for regions with high concentrations than for regions with low concentrations. We therefore investigate the uncertainty introduced by our simplification for weighted brightness temperatures and sea-ice retrievals.

The total sea-ice concentration dependent brightness temperature TB_{tot} is computed as follows:

$$TB_{tot} = (1\text{-}SIC) \cdot TB_w + SIC \cdot TB_i \quad (1)$$

where SIC is the sea-ice concentration between 0 and 1, TB_w is the water brightness temperature and TB_i is the sea-ice brightness temperature. We use Eq. 1 to assess the importance of using as realistic ice brightness temperatures as possible. TB_w is defined as 161.35 K, as given in [RD-79]. Figure 7-5 and Figure 7-3 show the difference between TB_{tot} computed with TB_i on the basis of a complex profile and TB_{tot} computed with TB_i on the

basis of a simple profile, for different sea-ice concentrations. As expected through the linearity of Eq. 1, the difference between both sets of TB_{tot} decreases from (2.9±3.8) K at 100% concentration to (0.4±0.6) K at 5% in winter. In summer, the uncertainty is much higher, from (45.7±45.0) K at 100% to (6.9±6.8) K at 5%.

Table 7-3: Influence of the simplification of the profiles on the total brightness temperature (mean absolute difference between simple and complex) [in Kelvin] and sea-ice concentration retrieval [in %] for FYI as a function of sea-ice concentration.

Ingoing SIC	0.15	0.30	0.50	0.75	0.90	1.00
V-polarization						
ΔTB_{tot}						
all year	3.1±5.4	6.1±10.8	10.2±17.9	15.4±26.9	18.4±32.3	20.5±35.9
winter	0.4±0.6	0.9±1.1	1.4±1.9	2.2±2.8	2.6±3.4	2.9±3.8
summer	6.9±6.8	13.7±13.5	22.9±22.5	24.3±33.8	41.2±40.1	45.7±45.0
Retrieved SIC						
all year	0.74±1.33	1.48±2.66	2.47±4.43	3.70±6.65	4.44±7.98	4.93±8.87
winter	0.15±0.008	0.30±0.2	0.50±0.03	0.75±0.04	0.90±0.05	1.01±0.05
summer	1.58±1.76	3.17±3.52	5.28±5.86	7.92±8.80	9.50±10.56	10.56±11.73
H-polarization						
ΔTB_{tot}						
all year	5.1±7.1	10.2±14.3	17.0±23.8	25.5±35.7	30.6±42.8	34.0±47.6
winter	1.8±3.0	3.6±6.0	6.1±10.0	9.1±15.1	10.9±18.1	12.1±20.1
summer	9.8±8.6	19.6±17.1	32.7±28.5	49.1±42.8	58.9±51.3	65.4±57.0
Retrieved SIC						
all year	0.11±1.13	0.21±2.25	0.35±3.75	0.53±5.63	0.64±6.75	0.71±7.5
winter	0.15±0.49	0.31±0.97	0.51±1.64	0.77±2.47	0.92±2.96	1.03±3.29
summer	0.04±1.65	0.08±3.3	0.13±5.5	0.19±8.25	0.23±9.90	0.25±11.00

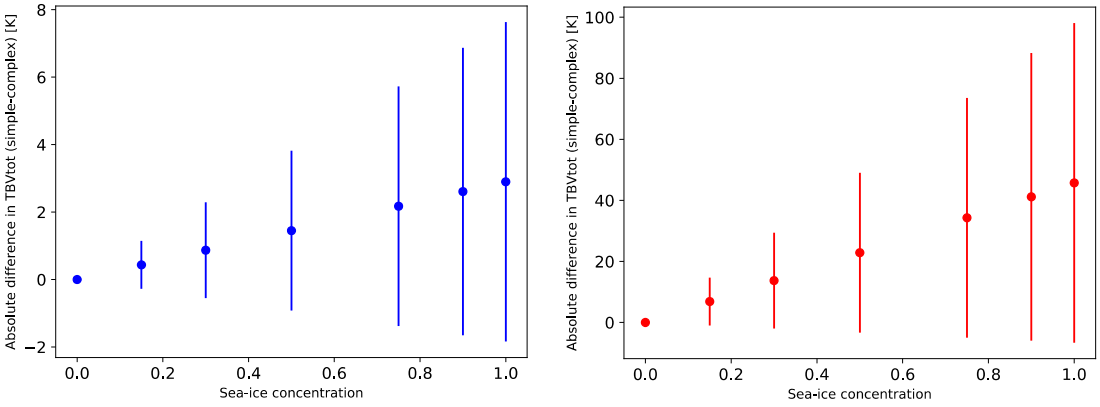

(a) Winter (b) Summer

Figure 7-5: Absolute difference in total brightness temperatures at 6.9 GHz (vertical polarization) between simple and complex profiles as a function of sea-ice concentration, first-year ice. Error bars represent one standard deviation.

The observational uncertainty of retrieval algorithms is given in % of sea-ice concentration. It is therefore not straightforward to compare their uncertainty to the uncertainty we produce by simplifications of the sea-ice temperature and salinity profiles introduced in the computation of the total

brightness temperature and which is given in K. In a next step, we therefore transform Eq. 1 to retrieve the sea-ice concentration:

$$SIC = (TB_{tot,complex} - TB_w) / (TB_{i,simple} - TB_w) \quad (2)$$

With Eq. 2, we can assess how much the simplified ice brightness temperatures influences the retrieval of a sea-ice concentration from a measured "real" brightness temperature. In winter, the error in retrieved sea-ice concentration ranges from (101±5) % at 100% "real" concentration to (15.0±0.8) % at 15% "real" concentration (Figure 7-6). The uncertainty is therefore lower to current retrievals (up to 10%). As already expected from the high spread of brightness temperatures, the error in retrieved summer sea-ice concentration is much higher and yields unrealistic concentrations above 100%, even at very low "real" concentrations. The retrieved sea-ice concentration reaches (1056%±1173) % at 100% "real" concentration. This uncertainty comes from the spread in surface liquid water fraction between complex and simple profiles. Simple profiles tend to have high surface liquid water fractions more often in summer. $TB_{i,simple}$ is therefore much lower than $TB_{tot,complex}$ in these cases and Eq. 2 yields a result that is much higher than 100%.

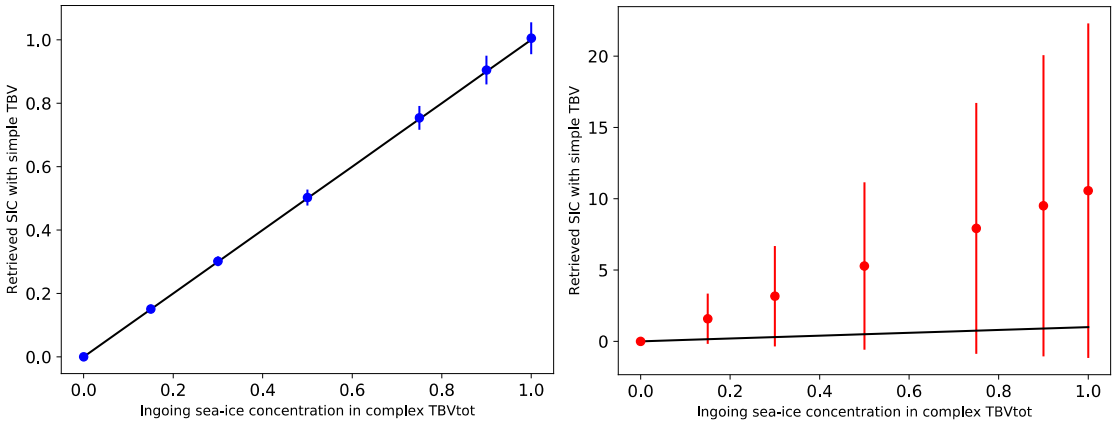

(a) Winter (b) Summer

Figure 7-6: Sea-ice concentration as retrieved with $TB_{i,simple}$ as a function of the sea-ice concentration used to compute TB_{tot} for 6.9 GHz (vertical polarization), first-year ice.

Winter results for H-polarization also show a reasonable mean retrieved sea-ice concentration (Table 7-3). The standard deviation is however much larger. In summer, the mean retrieved concentration is very low but the standard deviation very large as well. More investigation is needed to understand this behavior.

7.4 Conclusion

Using a theoretical approach involving a complex 1D thermodynamical sea-ice model and sea-ice emission model, we explore to what extent realistic brightness temperatures can be simulated from simple climate model sea-ice information. We find that a simplified salinity profile introduces most of the uncertainty in the brightness temperature simulation compared to a simplified temperature profile. Using a salinity as function of depth yields slightly better results than using a salinity constant over depth. In winter, the difference between "real" and "GCM" brightness temperatures (V-

polarization) reaches up to (2.9±3.8) K at 100% sea-ice concentration for first-year ice, which means that we can simulate realistic brightness temperatures from GCM output. In summer, however, the brightness temperature's sensitivity to surface liquid water fraction leads to a very high difference between "real" and "GCM" brightness temperatures. We therefore argue that, to use a sea-ice satellite simulator in the summer, the surface properties must be known in a much more detailed way. However, only very small changes in the surface temperature (on the order of 0.1 or even 0.01 K) can already yield a high range of liquid water fractions, when near 0 °C. Therefore, this task might well be impossible to reach.

Further insights can be gained from further analysis of multiyear ice and H-polarization. Also, including snow-covered ice can help assess brightness temperatures resulting from situations nearer to the real ice conditions. Finally, including several frequencies can even unlock more mysteries about sea-ice brightness temperatures.

8 Summary

We computed sea-ice area and extent and compared the SICCI-2 products with themselves (AMSR-E versus AMSR2), the SICCI-2 product with the OSI-450 product, and the combined OSI-450 / SICCI-2 product with the sea-ice index. We can state that the new data set provides a consistent time-series of sea-ice area and extent.

We computed the Arctic and Antarctic sea-ice volume time series based on a combined, inter-sensor (Envisat to CryoSat-2) bias corrected sea-ice thickness data set and the SICCI-2 sea-ice concentration data set gap-filled with the OSI-450 data set. For the Arctic this is done only for the central Arctic Ocean to comply with the limited validity of the snow-depth data set used for the freeboard-to-thickness conversion.

We computed sea-ice volume fluxes for several zonal and meridional flux gates in the Arctic and Antarctic by combining SICCI-2 / OSI-450 data with the monthly NSIDC sea-ice motion product. We provide and discuss time-series of the sea-ice volume flux for all (some selected) flux gates in the Arctic (Antarctic).

Based on the adjoint methodology, satellite sea ice data of concentration (SIC) and thickness (SIT) are assimilated into a regional Arctic coupled ocean-sea ice model for the period of 2000-2015 (SIT: 2003-2008, external data set), as well as other climate variables. The spatial distributions of sea ice become closer to the observations after assimilation, in particular for the position of ice edge. There is large improvement for the representation of SIC in the central Arctic in summer.

We have examined the compatibility of the SICCI products with the sea-ice physics described in large scale earth-system models. Particular focus has been put on examining the usefulness of the underlying uncertainty information for the purpose of model evaluation. We are very pleased with the provision of the SICCI SIC and SIT products, and in particular welcome the provision of underlying uncertainties. We would, however, ask both the SIT and the SIC teams to examine whether the reported uncertainties are indeed realistic, and whether they can possibly be diminished, which would in particular be necessary to increase the usefulness of the SIT product.

Using a theoretical approach involving a complex 1D thermodynamical sea-ice model and sea-ice emission model, we explore to what extent realistic brightness temperatures can be simulated from simple climate model sea-ice information. We find that a simplified salinity profile introduces most of the uncertainty in the brightness temperature simulation compared to a simplified temperature profile. Further insights can be gained from further analysis of multiyear ice and horizontally-polarized brightness temperatures. Also, including snow-covered ice can help assess brightness temperatures resulting from situations nearer to the real ice conditions. Finally, including several frequencies can even unlock more mysteries about sea-ice brightness temperatures.

< End of Document >